

# UC Santa Cruz

## UC Santa Cruz Electronic Theses and Dissertations

### Title

Fiber sensors for molecular detection using Raman and surface enhanced Raman scattering

### Permalink

<https://escholarship.org/uc/item/7z67236c>

### Author

Yang, Xuan

### Publication Date

2013

Peer reviewed|Thesis/dissertation

UNIVERSITY OF CALIFORNIA  
SANTA CRUZ

**FIBER SENSORS FOR MOLECULAR  
DETECTION USING RAMAN AND SURFACE  
ENHANCED RAMAN SCATTERING**

A dissertation submitted in partial satisfaction  
of the requirements for the degree of

DOCTOR OF PHILOSOPHY  
in  
ELECTRICAL ENGINEERING

by  
**Xuan Yang**

March 2013

The Dissertation of Xuan Yang  
is approved:

---

Professor Claire Gu, Chair

---

Professor Jin Z. Zhang

---

Professor Holger Schmidt

---

Dr. Tiziana C. Bond

---

Tyrus Miller  
Vice Provost and Dean of Graduate Studies

Copyright © by

Xuan Yang

2013

# Table of Contents

<b>List of Figures</b> .....	v
<b>List of Tables</b> .....	xiii
<b>Abstract</b> .....	xiv
<b>Acknowledgements</b> .....	xvii
<b>Chapter 1. Introduction</b> .....	1
1.1 Background: Raman and surface enhanced Raman scattering .....	1
1.2 Multimode fiber SERS sensor .....	4
1.3 Hollow core photonic crystal fiber .....	9
1.4 Motivation and contribution .....	14
<b>Chapter 2. Multimode fiber SERS sensors</b> .....	17
2.1 Tip coated multimode fiber (TCMMF) SERS sensor .....	17
2.1.1 Synthesis of silver nanoparticles (SNPs) .....	17
2.1.2 Preparation of SERS substrate and optical fiber probes .....	18
2.1.3 SERS characterization and the aqueous protein detection .....	20
2.2 Fiber SERS sensor fabricated by interference lithography .....	26
2.2.1 Fabrication of IL-defined nanopillar array on the fiber facet .....	27
2.2.2 Optical and SERS characterization of the fiber SERS probe .....	30
2.2.3 Vapor SERS detection .....	35
2.2.4 Simulation analysis .....	38

<b>Chapter 3. Photonic crystal fiber sensors</b> .....	46
3.1 Gas Raman detection .....	46
3.1.1 Experimental set-up of HCPCF gas Raman detection .....	46
3.1.2 Ambient gas sensing .....	49
3.1.3 Organic vapor sensing .....	51
3.2 Glucose Raman detection .....	57
3.2.1 Background knowledge of glucose detection .....	57
3.2.2 Liquid-filled PCF preparation and Raman measurement .....	59
3.2.3 Glucose Raman detection at physiological concentrations .....	60
3.3 HCPCF SERS detection and characterization .....	66
3.3.1 Experimental demonstrations of HCPCF SERS detections .....	67
3.3.2 Theoretical analysis and discussion .....	77
3.4 Bacteria SERS detection using LCPCF .....	83
3.4.1 Bacterial strain and culture conditions .....	83
3.4.2 Bacteria SERS detection .....	84
<b>Chapter 4. Portable fiber SERS sensing systems</b> .....	88
4.1 Experimental demonstrations of portable fiber SERS systems .....	89
4.2 Results and discussion .....	94
<b>Chapter 5. Summary</b> .....	98
<b>Bibliography</b> .....	101

## List of Figures

Fig. 1.1: Energy level diagram showing different light scattering processes: elastic Rayleigh scattering; inelastic stokes and anti-stokes Raman scattering. ...	1
Fig. 1.2: Schematic of plasmon oscillation for a nanosphere. ....	3
Fig. 1.3: Schematic of a D-shaped fiber SERS probe. ....	6
Fig. 1.4: Schematic of a TCMMF SERS probe with a double substrate “sandwich” structure. ....	7
Fig. 1.5: SEM micrograph showing a Section of a gold nanorod array transferred to the optical fiber facet. ....	8
Fig. 1.6: SERS spectra of RhB. Curve A: obtained from the measuring tip of the HCPCF probe (power: ~4.7 mW, integration time: 20 s, and accumulation: 5); Curve B: after fiber background subtraction; Curve C: obtained using a SERS substrate coated on a Si wafer (power: ~0.47 mW, integration time: 20s, and accumulation: 1). Inset: micrograph of the cross section of HCPCF. ....	11
Fig. 1.7: Schematic of the LCPCF SERS sensor and its cross-Sectional view. ...	12
Fig. 1.8: SERS spectra of R6G molecules at the concentration of $10^{-6}$ M using different detection methods: LCPCF sealed end detection, LCPCF unsealed detection, and bulk detection. ....	14
Fig. 2.1: (a) UV-vis of citrated-reduced SNPs with the SPR at 424 nm; (b) UV-vis of the CTAB-capped SNPs with the SPR at 391 nm. ....	18

Fig. 2.2: TEM image of the citrate-reduced SNPs. ....	19
Fig. 2.3: SEM image of the CTAB-capped SNPs coated on the fiber end. ....	20
Fig. 2.4: Schematic of the TCMMF SERS probe in aqueous protein detection. ...	21
Fig. 2.5: SERS spectra of R6G solution ( $10^{-5}$ M) by bulk detection and TCMMF SERS probe. ....	22
Fig. 2.6: SERS spectra of lysozyme detected by bulk solution and TCMMF probe at different concentrations: (a) $2 \mu\text{g/mL}$ ; (b) $0.2 \mu\text{g/mL}$ . ....	24
Fig. 2.7: SERS spectra of cytochrome c detected by bulk solution and TCMMF probe at different concentrations: (a) $2 \mu\text{g/mL}$ ; (b) $0.2 \mu\text{g/mL}$ . ....	25
Fig. 2.8: (a) Schematic of the spin coating process for the optical fiber sample; (b) photograph of the fiber ferrule; (c) SEM images of the fiber ferrule facet. ....	28
Fig. 2.9: Schematic of the two-beam interference lithography set-up. ....	29
Fig. 2.10: SEM images of the silver-coated nanopillar array patterned on the fiber core (tilted view: $45^\circ$ ). ....	32
Fig. 2.11: Reflectance spectra of the fiber SERS probe in both the front end configuration (A) and remote end configuration (B). ....	33
Fig. 2.12: a) SERS spectra of BPE monolayer using the fiber SERS probe in both the front end configuration and remote end configuration (laser power: $0.2 \text{ mW}$ , integration time: 10 s); (b) Raman spectrum of $0.1 \text{ M}$ BPE obtained with the same spectroscopy system (laser power: $2 \text{ mW}$ , integration time: 10 s). ....	34

Fig. 2.13: Curve A: the SERS spectrum of the fiber probe for the remote detection of toluene vapor (laser power: 2 mW, integration time: 10 s); Curve B: the spectrum obtained by the unpatterned optical fiber in the toluene vapor with the same system configuration. ....	37
Fig. 2.14: Curve A: the SERS spectrum of the fiber probe for the remote detection of DNT vapor (laser power: 2 mW, integration time: 10 s); Curve B: the spectrum obtained by the same optical fiber without any DNT vapor exposure with the same system configuration. ....	38
Fig. 2.15: Geometry of the unit cell in the simulation model: (a) the purple region corresponds to the fused silica on the fiber facet; (b) the blue region corresponds to the silver coating on the fused silica pillar; the rest of the unit cell is the air region. ....	40
Fig. 2.16: Geometry of the unit cell in the simulation model with different directions of the metal coating: (a) $\beta = -45^\circ$ ; (b) $\beta = -90^\circ$ .....	41
Fig. 2.17: Simulated reflectance spectrum for the front end configuration. ....	42
Fig. 2.18: Simulated reflectance spectrum for the remote end configuration. ....	43
Fig. 2.19: Simulated EM distribution in the front end configuration ( $\beta = 0^\circ$ , $\lambda = 550$ nm): (a) $z = 0$ plane; (b) $x = 0$ plane; (c) $y = 0$ plane. ....	44
Fig. 2.20: Simulated EM distribution in the remote end configuration ( $\beta = 0^\circ$ , $\lambda = 550$ nm): (a) $z = 0$ plane; (b) $x = 0$ plane; (c) $y = 0$ plane. ....	45

Fig. 3.1: Schematic of a HCPCF probe for gas/vapor Raman detection. Top right: Cross Sectional view of the HCPCF probe; Bottom right: the air channels of the HCPCF filled with gas/vapor molecules. ....	47
Fig. 3.2: Typical attenuation and dispersion of the HCPCF (Model: HC-800B) used in gas Raman detection. ....	48
Fig. 3.3: (a) Comparison of the ambient N <sub>2</sub> /O <sub>2</sub> Raman signals collected by the 30 cm-long HCPCF probe (10 s) and the conventional bulk detection (60 s); (b) Ambient N <sub>2</sub> /O <sub>2</sub> Raman signals obtained by the HCPCF probe at various fiber lengths in the range of 5-30 cm; (c) Length-dependence of the N <sub>2</sub> Raman signal detected by the HCPCF probe; (d) Ambient N <sub>2</sub> /O <sub>2</sub> Raman signals obtained by the 10 meter-long HCPCF probe. ....	50
Fig. 3.4: Ambient CO <sub>2</sub> Raman detection by the HCPCF probe. (Integration time: 3 min). ....	51
Fig. 3.5: (a) Raman spectra of toluene vapor collected by the HCPCF probe at various concentrations (Integration time: 10 s): 0.57%, 0.19%, 0.04%; inset shows linear relationship between Raman signal for the strongest peak and concentration. (b) Intensity of the strongest peak of toluene vapor with respect to the filling time at the concentration of 0.57%. ....	53
Fig. 3.6: Raman spectra of acetone vapor collected by the HCPCF probe at various concentrations (Integration time: 10 s): 0.55%, 0.05%, 0.01%; inset shows linear relationship between Raman signal for the strongest peak and concentration. ....	54

Fig. 3.7: Raman spectrum of 1,1,1-trichloroethane vapor collected by the HCPCF probe at the concentration of 1.2%. (Integration time: 60 s). .....	54
Fig. 3.8: Raman spectrum of the toluene/acetone/1,1,1-trichloroethane vapor mixture (0.57%, 0.55%, 1.2%) collected by the HCPCF probe. (Integration time: 10 s); inset shows the close overlap but clear separation of the two fundamental peaks of acetone and 1,1,1-trichloroethane, respectively. ....	56
Fig. 3.9: Schematic of a liquid-filled PCF probe for glucose detection. Top right: Cross Sectional view of the PCF probe (provided by Crystal Fiber A/S); Bottom right: the air channels of the PCF filled with glucose solution. ..	60
Fig. 3.10: Raman spectra of glucose solutions collected by (a) conventional bulk Raman spectroscopy at the glucose concentration of 1 M; and (b) a liquid-filled PCF probe at the glucose concentration of 50 mM. ....	62
Fig. 3.11: Raman spectra of glucose solutions collected by the liquid-filled PCF probe at various concentrations: (a) 1 mM; (b) 5 mM; (c) 10 mM; (d) 15 mM; (e) 25 mM. ....	63
Fig. 3.12: Concentration-dependent Raman intensities of glucose ( $1127\text{ cm}^{-1}$ ) measured by the liquid-filled PCF probe. Each datum indicates 5 measurements for each sample, and each error bar indicates the standard deviation. ....	64

Fig. 3.13: Raman spectra of (a) glucose (10 mM), (b) fructose (10 mM), and (c) a mixture of glucose (5 mM) and fructose (5 mM) measured by the liquid-filled PCF probe. ....	66
Fig. 3.14: Comparison of SERS spectra of R6G at the concentration of $10^{-6}$ M between the bulk detection and using a 2 mm liquid-filled PCF. ....	69
Fig. 3.15: Comparison of the SERS signals at lowest excitation powers between bulk detection and using liquid-filled PCF when the concentration of R6G is $10^{-6}$ M. ....	72
Fig. 3.16: SERS signals detected from (a) bulk detection and (b) liquid-filled PCF when the concentration of R6G is $10^{-8}$ M. While bulk detection can detect R6G signal, liquid-filled PCF failed due to an enhanced SNPs background. ....	73
Fig. 3.17: When the solution of SNPs is diluted by a factor of 10, the SERS signals are detected from (a) bulk detection and (b) liquid-filled PCF at the concentration of $10^{-7}$ M. The positions of typical R6G peaks are marked by red arrows. In this case, liquid-filled PCF can detect a lower concentration ( $10^{-7}$ M) than bulk detection. ....	74
Fig. 3.18: Background comparison between a liquid-filled PCF and a LCPCF with only the silver colloid. ....	76
Fig. 3.19: SERS signal from the detection of 0.1 nM R6G using a LCPCF. Peaks (a) and (c) are from the citrate introduced during the synthesis of SNPs. Peaks (b), (d), (e), (f), (g), (h), (i), (j), (k) and (l) are typical R6G peaks.	

Specifically, (d) and (e) are split from the  $1204\text{ cm}^{-1}$  peak while (g) and (h) are split from the  $1312\text{ cm}^{-1}$  peak compared to the high concentration SERS spectrum. .... 77

Fig. 3.20: Light propagation when focusing a Gaussian beam at (a) the surface of a bulk liquid medium (water), (b) the entrance of a HCPCF with open air channels, (c) the entrance of a HCPCF with all channels filled with liquid, (d) the entrance of a LCPCF with only the core channels filled with liquid, (e) the entrance of a LCPCF with a  $200\text{ }\mu\text{m}$  air gap between the entrance and the liquid surface. In each set of images, the top one corresponds to the field distribution near the entrance of either bulk medium or HCPCF, while the bottom one corresponds to the field distribution after a propagation distance of  $400\text{ }\mu\text{m}$  from the entrance. .... 79

Fig. 3.21: Light power inside the fiber cross-section with respect to the propagation distance in various cases: (a) bulk water; (b) HCPCF with open air channels; (c) water-filled PCF; (d) LCPCF with a  $200\text{ }\mu\text{m}$  air gap between the fiber entrance and the surface of water. .... 81

Fig. 3.22: Plot of intensity distribution with respect to the radial position of (a) liquid-filled PCF; (b) LCPCF. Gray regions indicate silica walls in the HCPCF. .... 82

Fig. 3.23: SERS spectra of MR-1 cells detected by (a) bulk detection ( $10^{10}$ , $10^9$ , and $10^8$ cells/mL), and (b) using the LCPCF probe ( $10^{10}$ , $10^8$ , and $10^6$ cells/mL). .....	85
Fig. 3.24: Control experiment with lactate medium and SNPs but without MR-1 cells in both (a) bulk detection and (b) using the LCPCF SERS probe. ....	86
Fig. 4.1: Experimental set-up: (a) TCMMF-portable SERS system; (b) LCPCF-portable SERS system (spectrometer and laptop computer not included). .....	90
Fig. 4.2: Schematics of (a) TCMMF-portable SERS system and (b) LCPCF-portable SERS system (not to scale). .....	91
Fig. 4.3: SERS signals obtained using the portable-TCMMF system and that obtained using direct sampling, when the R6G concentration is $10^{-5}$ M. ....	95
Fig. 4.4: SERS signals obtained using the portable-TCMMF system after washing procedures. ....	95
Fig. 4.5: SERS signals obtained using (a) direct sampling, and (b) the portable-LCPCF system, when the R6G concentration is $10^{-6}$ M. ....	97

## List of Tables

Table 2.1: Band assignments for lysozyme and cytochrome c. ....	26
Table 3.1: Using the nitrogen Raman line as the calibration, the relative Raman intensities of the vapors collected separately and in mixture by using the HCPCF probe. ....	56
Table 3.2: Using the $1509\text{ cm}^{-1}$ peak as a reference, the intensity of the conventional Raman signal and the SERS signal in both the bulk detection and the liquid-filled PCF. ....	70
Table 3.3: Band assignments for bacteria of <i>Shewanella oneidensis</i> MR-1. ....	87

## **Abstract**

### Fiber sensors for molecular detections using Raman and surface enhanced Raman scattering

Xuan Yang

In this dissertation, highly sensitive optical fiber sensors based on Raman spectroscopy (RS) and surface-enhanced Raman scattering (SERS) are studied with focus on applications in various chemical and biological detections. In particular, two main categories of optical fibers have been used as the sensing platforms: one is the conventional multimode optical fiber and the other is the hollow core photonic crystal fiber (HCPCF). For the conventional multimode optical fiber, we've developed two types of probes using SERS techniques: the first is based on a double substrate "sandwich" structure with colloidal metal nanoparticles, and the second is based on interference lithography-defined nanopillar array structure on the fiber facet with the metal film deposition. For the HCPCF, the photonic bandgap guiding mechanism provides an ideal sensing platform because the confinement of both light and sample inside the fiber enables direct interaction between the propagating wave and the analyte. We demonstrate that by filling up the air channel(s) of the fiber with gas or liquid samples, it can significantly increase the sensitivity of the sensors in either regular Raman or SERS applications. For RS applications, these fiber sensors were tested with ambient gases, organic vapors, and biomedically important glucose molecule. For SERS application, these fiber sensors were evaluated with Rhodamine

6G, trans-1,2-bis(4-pyridyl)-ethylene, toluene vapor, 2,4-dinitrotoluene vapor, proteins and bacteria. We also demonstrate that these fiber sensors can be integrated with the portable Raman spectrometer in order to make it practical for out-of-laboratory applications. The techniques developed in this study are expected to have significant impact in chemical, biological, environmental, national security, and other applications.

I would like to dedicate this thesis to my grandparents, Xinghai Yang and Laqing Shu. Without their love and support, I would never be able to get to this point.

## **Acknowledgments**

First, I am heartily thankful to my supervisor, Prof. Claire Gu from Department of Electrical Engineering at UC Santa Cruz, whose guidance, support, and encouragement helped me a lot during all the time of my research. With her in-depth knowledge and great enthusiasm, she brought me to the field of optics and nanotechnology and taught me a lot of knowledge in this field. Also, she provided a lot of great opportunities to me, which are very precious and helpful for the career development in my life. Without her support and encouragement, I would have been lost these years. It is so lucky to have her as my supervisor and I owe my deepest gratitude to her for always being there for me.

Second, I should thank my supervisor, Dr. Tiziana C. Bond at Lawrence Livermore National Laboratory. She helped me win the prestigious Lawrence Scholar Fellowship at LLNL and offered a fantastic opportunity to work in her group to finish my thesis. During those hard times, it is her that always gave me the strongest support and encouragement. Her knowledge, experience, and spirit in research have benefited me tremendously.

I am grateful to Prof. Jin Z. Zhang from Department of Chemistry and Biochemistry at UC Santa Cruz, for his help and advice on my thesis work. He is very nice and gave me a lot of support in the experiments done in his lab. I should thank him for agreeing to be a member of my Ph.D. Thesis Reading Committee.

I should also thank Prof. Holger Schmidt from Department of Electrical Engineering at UC Santa Cruz for agreeing to be a member of my Ph.D. Thesis Reading Committee.

I also want to thank Dr. Shaowei Chen, Dr. Yat Li, Dr. Rebecca Newhouse, Dr. Fang Qian, Damon A. Wheeler, Dr. Lei Tian, Dr. Qiao Xu, Dancheng Wang from Department of Chemistry and Biochemistry at UC Santa Cruz, Dr. Chao Shi, Zuki Tanaka, Dr. Liangcai Cao, Zhigang Zhao, Pingyao Lin, Dr. Bin Chen from Department of Electrical Engineering at UC Santa Cruz, Dr. Allan S. P. Chang, Dr. Mihail Bora, Ali Altun, Dr. Keiko Munechika, Dr. Nazar Ileri, Dr. Cindy C. Larson, Dr. Thomas C. Carlson, Dr. Jerald A. Britten, Dr. Elaine Behymer at LLNL for their support, help, and discussion in my experiments.

I should give my thanks, gratitude, and love to my wife Xueqin Yin. Without her encouragement and deep understanding, I would not be able to finish the work. Her love would support me forever.

Most importantly, I would thank my family members, grandparents Xinghai Yang and Laqing Shu, parents Jinhua Chen and Zhengzhong Yang, and sister Juan Yang for their great and unselfish love. I miss them so much and love them forever.

# Chapter 1. Introduction

## 1.1 Background: Raman and surface enhanced Raman scattering

Raman spectroscopy (RS) is a well-known and useful spectroscopic technique employed to study vibrational, rotational, and other low-frequency modes in the molecules [1, 2]. As shown in Figure 1.1, Raman scattering is an inelastic scattering process in which the laser light interacts with the molecule, resulting in the energy of the laser photons being shifted up or down. The energy difference between the incident photon and the scattered photon gives information about the vibrational modes in the molecules. Since each molecule has its own set of vibrational modes, this technique has the advantage of molecular specificity over most of other spectroscopic techniques such as fluorescence spectroscopy [3].

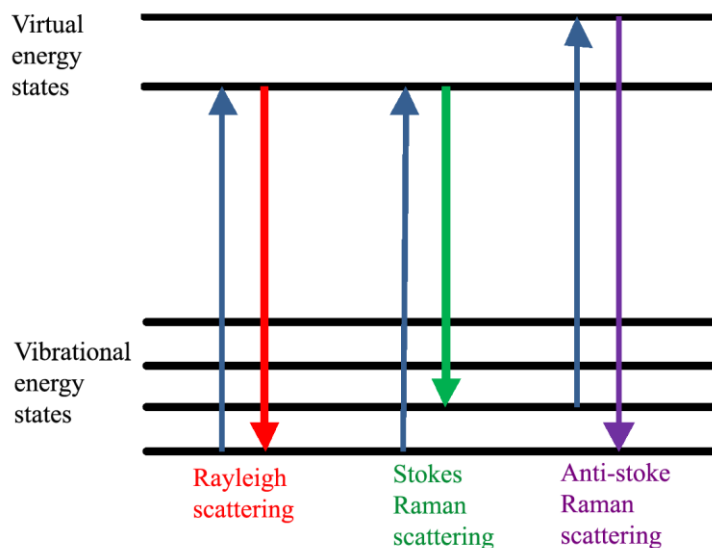


Figure 1.1: Energy level diagram showing different light scattering processes: elastic Rayleigh scattering; inelastic Stokes and anti-Stokes Raman scattering.

However, there is one main drawback of RS: the small scattering cross section ( $\sim 10^{-30} - 10^{-25} \text{ cm}^2/\text{molecules}$ ). The Raman signal is usually very weak and it is difficult to detect the analyte at low concentrations. In order to improve the sensitivity, several techniques have been developed to enhance the Raman signal, including both resonance enhancement and surface enhancement. In resonance RS, the energy of the incoming laser light is tuned such that it or the scattered light coincide with an electronic transition of the molecule, which can result in an enhancement factor of about  $10^2 - 10^3$  [4]. The main disadvantage of this technique is the increased fluorescence background and the photodegradation of the sample due to the increased energy of the incoming laser light.

The second technique is so-called surface enhanced Raman scattering (SERS), in which the molecule is adsorbed or close to a metallic nanostructure surface [5-7]. Historically, SERS was first observed in 1974 by Martin Fleischman and his coworkers; in this study SERS from pyridine adsorbed on electrochemically roughened silver was produced [8]. Although the exact mechanism of the enhancement effect of SERS is still under debate in the literature, there are generally two main reasons for the amplified Raman signal: one is the strong enhancement of the electromagnetic field by the surface plasmon resonance (SPR) of metallic nanostructures [9-11], which is considered as the main contributor of the SERS enhancement factor, and the other is the surface chemical enhancement [12].

Figure 1.2 shows the schematic of the localized SPR with the example of metal nanoparticles: in this case, light interacts with nanoparticles much smaller than the incident wavelength and this leads to an enlarged electromagnetic field due to a plasmon that oscillates locally around the nanoparticles with a frequency known as the localized SPR [11]. The enhancement factor is an overall enhancement of electrical field at both the excitation frequency and the scattered Raman frequency, which is approximately  $E^4$ . Larger enhancement can be achieved when metal surface roughing or aggregation is taken into consideration [13-15]. Typically, for roughened metal films, the enhancement is around  $10^3 - 10^5$ ; for isolated metal nanoparticles, the enhancement is on the order of  $10^6$ ; and for nanoparticles aggregates, they have even stronger enhancement of  $10^7 - 10^9$  [16]. The increase in enhancement for aggregates is believed to be due to the stronger electromagnetic field at the junctions of nanoparticles (e.g., a nanoparticle dimer system) in the aggregates, as shown by the simulation work done by Xu et al. [17].

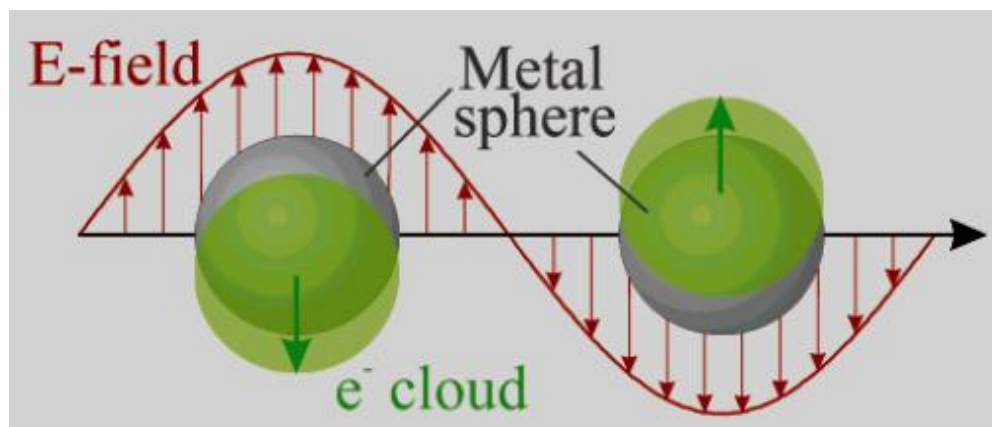


Figure 1.2: Schematic of plasmon oscillation for a nanosphere. Adapted with permission from ref. 11. Copyright 2003 American Chemical Society.

For the surface chemical enhancement, different mechanisms are proposed as the origin of a “chemical” or “electronic” SERS effect. One possible mechanism is the electronic coupling between molecule and metal and formation of an adsorbate-surface complex, which results in an increased Raman cross Section of the adsorbed molecule in the complex [12]. Another explanation involves a resonance Raman effect, which becomes operative with the shifted and broadened electronic levels in the adsorbed molecule compared to the free one. The chemical enhancement usually provides an enhancement factor of 10 to 100 [12].

## **1.2 Multimode fiber SERS sensor**

Traditionally, optical fibers have been successfully used in various systems to transmit optical power as well as information from one point to another. For example, optical fibers form the backbone of the long-distance communication networks, mainly due to their large bandwidth [18]. Most of the applications rely on the fantastic properties of optical fibers that can confine optical waves/energies inside the small core, guide the light through the fiber for a relatively long distance with manageable loss or dispersion, and when added with protective layers become flexible and easy to interface with other passive and active devices.

And in integrated sensors systems, optical fibers have been frequently utilized to connect the source and the detector, due to their flexibility, compactness, and low loss. However, optical fibers can offer more functions than a simple transmission; in particular, they can be used as a platform for molecular sensors based on RS and

SERS [19-30]. The fibers can serve to significantly enhance the sensitivity of RS/SERS and to facilitate the integration of a compact sensor system [28-30].

The single multimode fiber SERS probe was first demonstrated by Ken I. Mullen et al. in 1991 [19]. In the following years, different shapes of fiber sensing tips were studied, such as flat and angled fibers [22, 24]. Alternatively, wet chemical etching was utilized to fabricate tapered fiber probes for localized SERS detections [25, 26]. Also, metal nanoparticles have been used for the dip coating of the fiber facet as SERS-active substrates [31, 32].

In our previous research, Zhang et al. reported a D-shaped fiber SERS probe with coated metal nanoparticles as shown in Figure 1.3 [27]. In this study, the cross-sectional D-shape was formed by side-polishing the fiber for the purpose of increasing the SERS-active surface area to enhance the signal. Light can be coupled out of the polished fiber into silver or gold nanoparticles coated on the polished surface. In this configuration, as much as 70% of light that coupled into the fiber may be adsorbed into the SERS-active region across much of an  $80,000 \mu\text{m}^2$  surface comparing to  $\sim 50 \mu\text{m}^2$  of an end-polished fiber of the same kind. This can lead to as much as three orders of magnitude increase in the Raman scattered photons as compared to end-tip fiber probe. However, this configuration can only work well in a configuration that the SERS signal was directly collected by the Raman spectrometer instead of the same optical fiber, mainly due to the poor collection efficiency in the backscattering geometry.

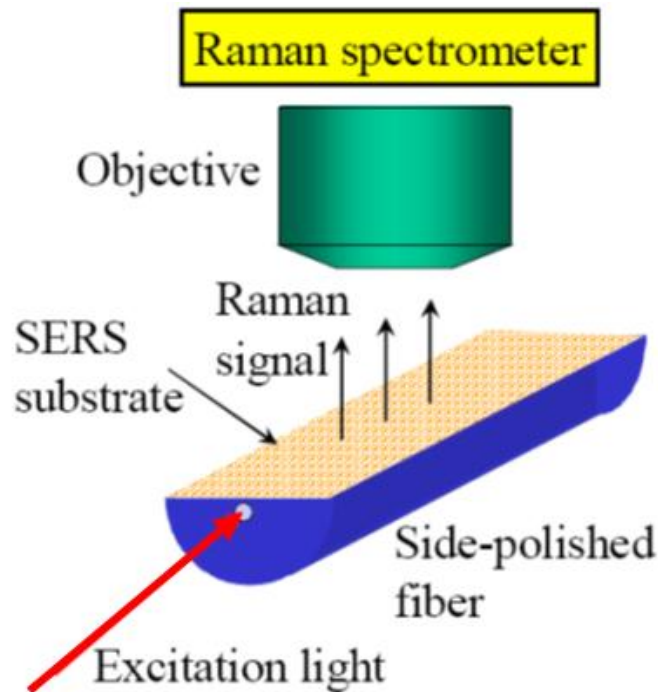


Figure 1.3: Schematic of a D-shaped fiber SERS probe. Adapted with permission from ref. 27. Copyright 2005 American Institute of Physics.

Besides increasing the surface area of the SERS-active region, another straightforward strategy for enhancing the SERS sensitivity is to increase the electromagnetic field. Therefore, previously Shi et al. developed a configuration based on a tip coated multimode fiber (TCMMF) with a double-substrate “sandwich” structure using two substrates simultaneously [28]. As shown in Figure 1.4, one type of silver nanoparticles (SNPs) was coated on the tip of a multimode fiber while the other type of SNPs was mixed with the target analyte molecules inside the solution. After dipping the coated fiber probe into the solution, these two types of SNPs would sandwich the analyte molecules where the electromagnetic field was stronger and therefore lead to an increased SERS signal. In this original design, 5 nm-sized

hexanethiolate-protected SNPs were used to coat the fiber tip and 25 nm-sized citrate-reduced SNPs were inside the solution and the results showed that the original TCMMF SERS probe can provides  $2-3\times$  sensitivity than the bulk detection, in which the laser light was directly focused onto the solution without using any optical fibers [28].

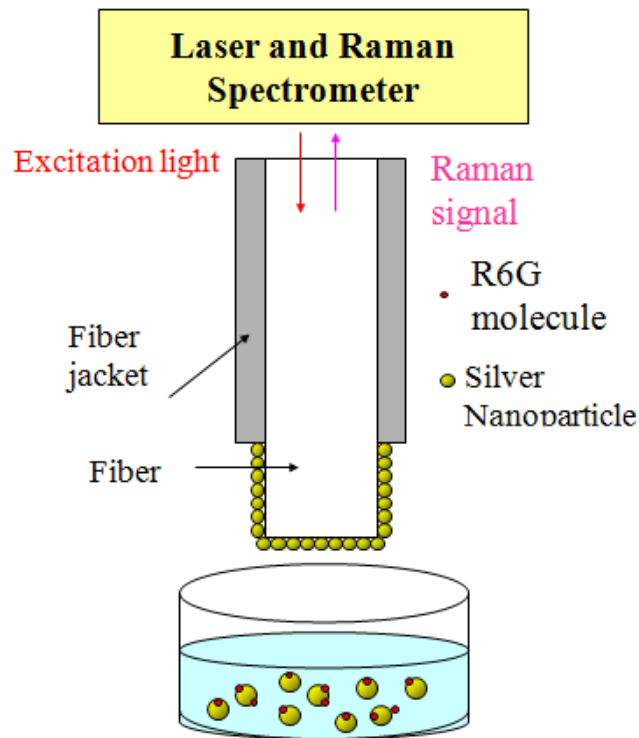


Figure 1.4: Schematic of a TCMMF SERS probe with a double substrate “sandwich” structure. Adapted with permission from ref. 28. Copyright 2008 American Institute of Physics.

On the other hand, for the purpose of the uniformity, reproducibility, and potential mass production, efforts have also been made to apply lithography techniques for nanopatterning and nanofabrication on the fiber facet. Focused ion-beam lithography (FIB) has been employed to define gold nanostructures on the fiber tip but inadvertent

doping with gallium ions changed the optical response of the SERS substrate [33]. For electron-beam lithography (EBL), it is challenging to be directly applied to the optical fiber; therefore, elegant transfer techniques have been proposed by Capasso et al. to transfer the EBL-defined metal nanostructures (e.g., gold nanorod array) onto the fiber facet for SERS application, as shown in Figure 1.5 [34, 35]. However, this technique is not appropriate for high-throughput fabrication. Nanoimprint lithography (NIL) might be a potential candidate technology for the high-yield mass production and Kostovski et al. have demonstrated a nanoscale biotemplating approach to fabricate fiber SERS sensors using NIL; but the nanoimprint resist in the fabrication process inevitably introduces additional coupling loss and Raman background, which would degrade the SERS performance, especially the sensitivity of the fiber probe [36, 37].

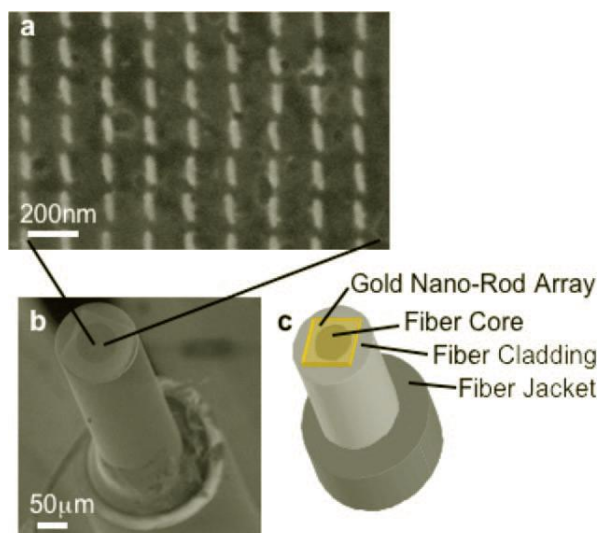


Figure 1.5: SEM micrograph showing a Section of a gold nanorod array transferred to the optical fiber facet. Adapted with permission from ref. 34. Copyright 2009 American Chemical Society.

With all the drawbacks of existing technologies mentioned above, there still exists a strong demand for developing new optical fiber SERS probes with high sensitivity, uniformity, reproducibility, and mass production capability.

### **1.3 Hollow core photonic crystal fiber**

While one way to improve the performance of the sensors relies on incorporating new SERS techniques into conventional multimode optical fiber facet, another strategy is to utilize advanced optical fiber technologies, such as hollow core photonic crystal fibers (HCPCF). Since its discovery in the 1990s, HCPCF has emerged as a powerful platform for a wide variety of fascinating applications [38-41]. The unique microstructure of axially aligned periodic air channels in HCPCF acts as reflectors to confine light in an empty core. With this so-called photonic bandgap effect, the optical power located in the glass region is greatly reduced and the interaction between light and glass can be very small as compared to conventional index-guiding fibers. Therefore, HCPCF has been employed in applications that require extremely low non-linearity, high breakdown threshold, and zero dispersion.

However, the combinations of optical sensing techniques and HCPCF for chemical and biological detections have only been extensively explored recently [29, 42-53]. By filling the air channel(s) with the target analyte, HCPCF can provide an ideal platform for the strong interaction between the light and the analyte while minimizing the interference from the glass background, and therefore it is very promising to

improve the performance of existing optical sensing techniques. In the past decade, attempts have been made to utilize HCPCF for various optical sensing applications, such as absorption [42], fluorescence [43], Raman [44-48] and SERS [29, 49-53].

In particular, as for the Raman applications, Konorov et al. first used the HCPCF for the Raman detection of 95% methane and observed a decreased fiber background compared to solid-core silica fiber probes [44]. Later, Buric et al. applied this technique in gas Raman detection with a focus on the detection of hydrocarbon gases [45, 46]. However, a systematic and quantitative study of this technique has not been given; more importantly, its multiplexing capability has not been quantitatively demonstrated.

And the first attempt to combine HCPCF and SERS was carried out in 2006 by Yan et al. in our previous work [50]. In this study, Yan et al. demonstrated a HCPCF SERS probe coated with a layer of gold nanoparticles on the inner wall of the air holes. The analyte solution entered the air holes due to the capillary force and was then dried during a heating procedure. The laser light was coupled into one end of the HCPCF, propagated along the fiber, and interacted with the SERS substrate and the molecules at the other end. Finally, the SERS signal was transmitted back to the measuring tip and coupled into the Raman spectrometer. Figure 1.6 shows the cross-section of a single HCPCF probe and the first proof-of principle demonstration with the SERS spectrum of Rhodamine B (RhB) detected by the HCPCF probe [50].

The original HCPCF probe can only operate well when the sample solution is dried in the fiber with the assistance of a heating procedure, which highly limits the

application for in vivo sensing. Also, the scheme of coating nanoparticles on the inner walls only utilized the light energy near the silica walls and has not fully taken advantage of the power inside the fiber for SERS detection. Moreover, the quality of HCPCF needs improvement for fewer defects, lower coupling loss, and better modal confinement.

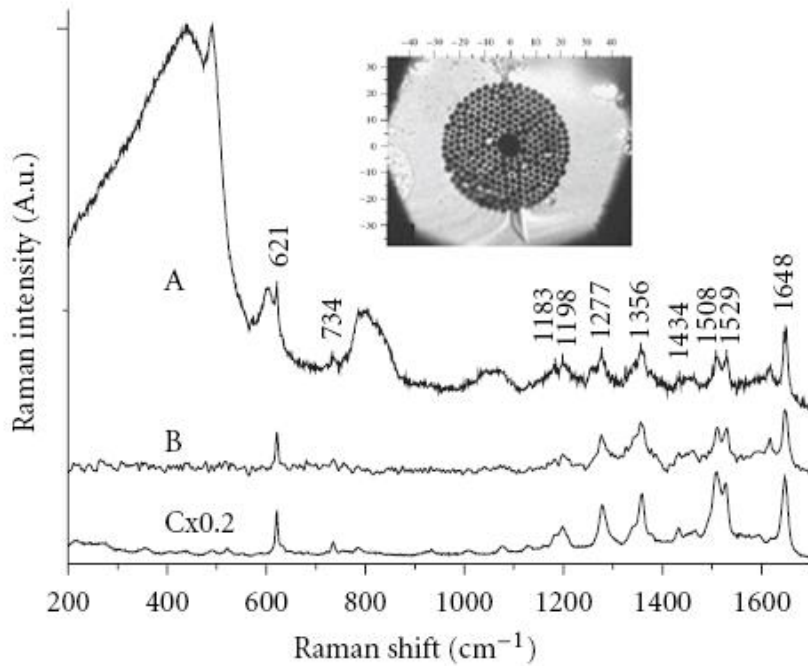


Figure 1.6: SERS spectra of RhB. Curve A: obtained from the measuring tip of the HCPCF probe (power:  $\sim 4.7$  mW, integration time: 20 s, and accumulation: 5); Curve B: after fiber background subtraction; Curve C: obtained using a SERS substrate coated on a Si wafer (power:  $\sim 0.47$  mW, integration time: 20s, and accumulation: 1). Inset: micrograph of the cross Section of HCPCF. Adapted with permission from ref. 50. Copyright 2006 American Institute of Physics.

To address the problems mentioned above, a liquid core PCF (LCPCF) probe was proposed and demonstrated by Zhang et al. [51]. The LCPCF probe was fabricated by

sealing the cladding channels of the HCPCF while leaving the central hollow core open. The SERS substrate, in this case SNPs, was mixed with the analyte inside the solution instead of being coated on the walls. After dipping the sealed end of the HCPCF into the SNPs/analyte mixture, only the central hollow core was filled due to the capillary effect. In this experiment, a 10 cm-long segment of HCPCF was prepared with both ends carefully cleaved by the fiber cleaver, and the cladding channels were sealed by inserting 2-3 mm of one tip of the HCPCF into a high-temperature flare ( $\sim 1000\text{ }^{\circ}\text{C}$ ) for 3-5 seconds. Figure 1.7 shows the schematic of LCPCF probe and the micrograph of the cross-section of the HCPCF after the sealing procedure [51].

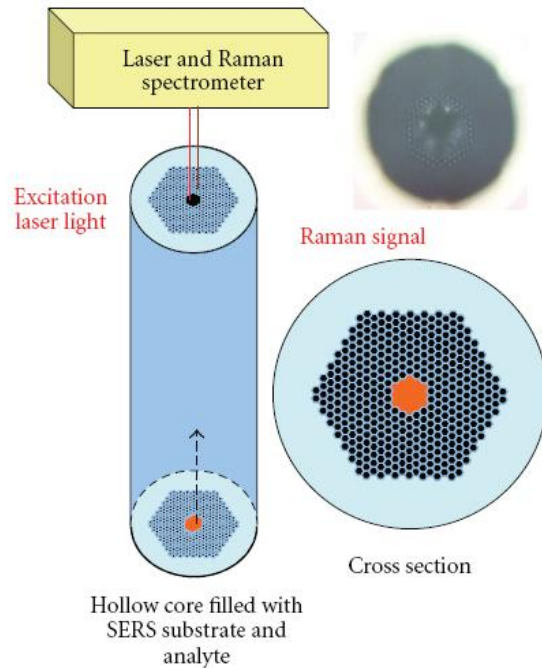


Figure 1.7: Schematic of the LCPCF SERS sensor and its cross-Sectional view. Adapted with permission from ref. 51. Copyright 2007 American Institute of Physics.

Various sample solutions such as Rhodamine 6G (R6G), human insulin, and tryptophan were tested for the evaluation of the LCPCF probe in this study. And Zhang et al. demonstrated that the LCPCF sensor is more sensitive than the original HCPCF probe, which is mainly attributed to the better confinement of both light and sample in the central core of the LCPCF and thereby increased interaction volume [51].

For further improvement of the sensitivity, a better control process was developed by Shi et al. in the following study [29]. A fusion splicer was used to seal the cladding channels instead of the high-temperature flare. By controlling the arc power, arc duration, and positions of the fibers, the fusion splicer can generate heat more uniformly and seal the cladding hole more accurately than the flame method. Shi et al. used two detection schemes: one was the sealed end detection in which the sealed end (i.e., dipped end) was placed under the microscope for coupling and the other was the unsealed end detection in which the unsealed end (i.e., undipped end) was placed under the microscope instead. And Shi et al. observed a sensitivity enhancement of  $100\times$  for the former configuration and a sensitivity enhancement of  $10\times$  for the latter compared to the bulk detection, as shown by Figure 1.8 [29]. However, the underlying mechanism for the difference of the sensitivity performance of two configurations was not clear. More importantly, the strong sensitivity enhancement of this probe has not been utilized for pushing the detection limit of the analyte. In addition, the SERS performance of this technique was mainly evaluated using mainly

small dye molecules; fewer efforts have been devoted to studying its applications in the detection of interesting biological macromolecules or systems.

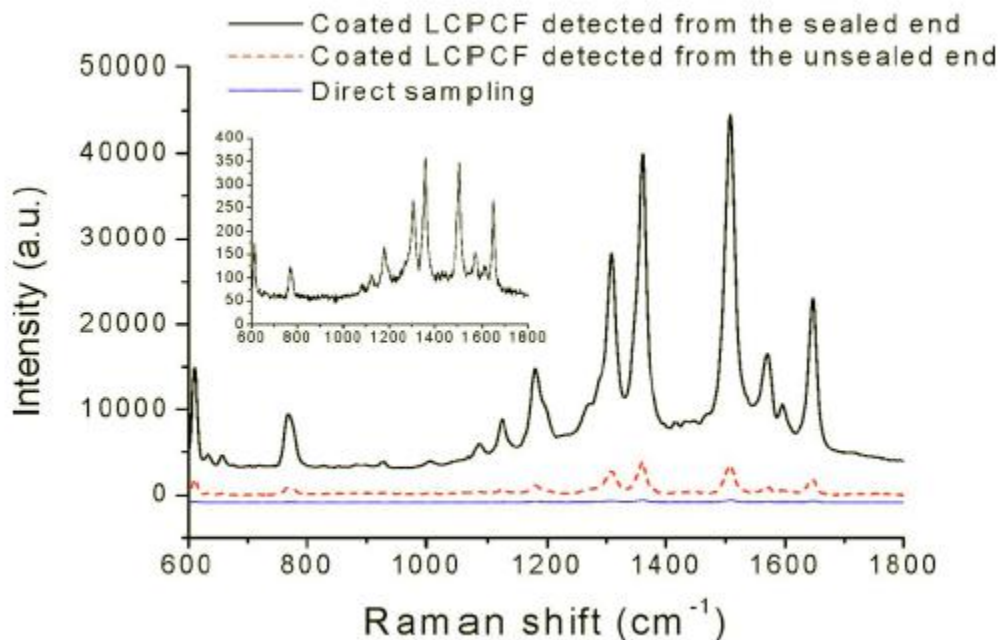


Figure 1.8: SERS spectra of R6G molecules at the concentration of 10<sup>-6</sup> M using different detection methods: LCPCF sealed end detection, LCPCF unsealed detection, and bulk detection. Adapted with permission from ref. 29. Copyright 2008 American Institute of Physics.

## 1.4 Motivation and contribution

In this thesis, we will focus mainly on the recent work from our research labs and aim to illustrate the molecular fiber Raman or SERS sensors as reliable devices with the advantages of molecular specificity, high sensitivity, flexibility, compactness, low cost, reproducibility, and in-situ remote sensing capability. We demonstrate the implementation of these techniques in various interesting chemical biological

detections. Moreover, we integrated these probes in a portable fiber SERS sensing system, which is crucial for out-of-laboratory applications.

Chapter 2 will discuss the multimode fiber SERS sensors with two different techniques: one is based a modified double substrate “sandwich” structure using colloidal metal nanoparticles. We demonstrate the improved performance of the TCMMF fiber SERS probe and apply this technique for the highly-sensitive detection of aqueous protein samples (cytochrome c and lysozyme). The other is based on interference lithography-defined nanopillar array structure on the fiber facet with the metal deposition and this technique has been employed for detections of the toluene and 2,4-dinitrotoluene vapors, which is the first time, to the best of our knowledge, that a single conventional optical fiber SERS sensor can be used for the remote detection of the vapor/gas samples at room temperature.

Chapter 3 will show the work of using HCPCF as a promising platform for Raman and SERS sensors. We demonstrate HCPCF can be used for the Raman detection of low-concentration ambient greenhouse gas (carbon dioxide) and organic vapors. Both the detection limits and the multiplexed sensing capability are discussed. In addition, this technique is utilized for the glucose Raman detection at physiological concentrations for the purpose of reducing laser exposure as compared to conventional RS. Moreover, we theoretically analyzed the HCPCF SERS probes and pushed the detection limit to 0.1 nM for R6G molecules, which is the lowest value obtained using similar techniques. With the improved sensitivity, we also apply this technique for the SERS detection of low-concentration bacterial cells.

Chapter 4 will demonstrate the integration of both TCMMF SERS probe and LCPCF SERS probe with a portable Raman spectrometer. With the appropriate coupling designs, we can achieve similar performance of the sensitivity enhancement of these sensors in the portable Raman system as compared to that in the bulky Renishaw Raman system. These fiber SERS probes integrated with a portable Raman spectrometer provide a promising scheme for the development of a compact and flexible molecular sensing system with high sensitivity and portability.

Chapter 5 concludes the dissertation and references are listed after chapter 5.

## **Chapter 2. Multimode fiber SERS sensors**

### **2.1 Tip-coated multimode fiber (TCMMF) SERS sensor**

#### **2.1.1 Synthesis of silver nanoparticles (SNPs)**

The SNPs used in the sample solution were prepared using the Lee and Meisel protocol, which basically used silver nitrate as the metal precursor and sodium citrate as the reducing agent [54]. The ones coated on the fiber facet were cetyltrimethylammonium bromide (CTAB)-capped SNPs, which were synthesized by a one-step reaction in an ethanol/water system [31, 55]. Briefly, CTAB ethanol solution (2 mL, 1 mM) was mixed with aqueous silver nitrate solution (30 mL, 5 mM) under vigorous stirring. After 10 min, freshly prepared aqueous sodium borohydride solution (1%) was added into the solution as the reducing agent until the color of the mixed solution changed to yellow-green and the color did not change when more sodium borohydride was added. 1 mL of the prepared CTAB-capped SNPs was purified by centrifugation (14,000 rpm, 25 min), and the solid SNPs were redispersed into 1 mL of Milli-Q water and ready for the coating process. Formations of both the citrate reduced negatively charged SNPs and the CTAB-capped positively charged SNPs were monitored by UV-vis spectroscopy using a HP 8452A spectrometer with 2 nm resolution and the corresponding surface plasmon resonances for these two types of SNPs were 424 nm (citrate-reduced SNPs) and 391 nm (CTAB-capped SNPs) respectively, as shown in Figure 2.1 [31]. The size of the

citrate-reduced SNPs was measured by a transmission electron microscope (TEM, model JEOL JEM 1200 EX) and the average SNP size was 30 nm, as shown in Figure 2.2 [31].

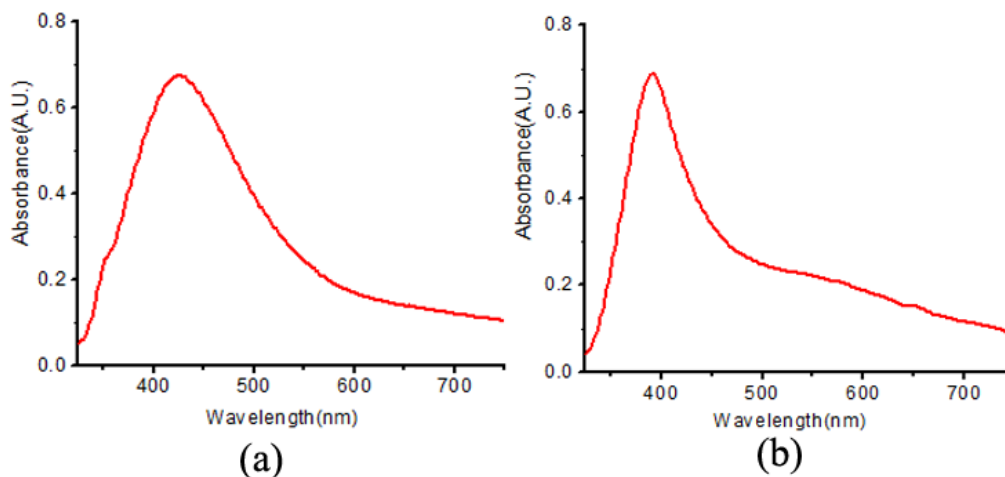


Figure 2.1: (a) UV-vis of citrate-reduced SNPs with the SPR at 424 nm; (b) UV-vis of the CTAB-capped SNPs with the SPR at 391 nm. Adapted with permission from ref. 31. Copyright 2011 American Chemical Society.

### 2.1.2 Preparation of SERS substrates and optical fiber probes

In this study, R6G solution at the concentration of  $10^{-5}$  M was chosen first as the test sample solution, which was prepared by mixing 30  $\mu$ L aqueous R6G solution ( $10^{-4}$  M) and 270  $\mu$ L of the citrate-reduced SNPs solution. For the biological application in aqueous protein SERS detection, the bulk sample preparation was the same as that reported by Ozaki et al. [56]. Briefly, the protein sample solutions were diluted 1/10 with the aggregation agent (0.1 M  $\text{Na}_2\text{SO}_4$ , pH = 3) and then mixed with the citrate-reduced SNPs (1:5, v/v).

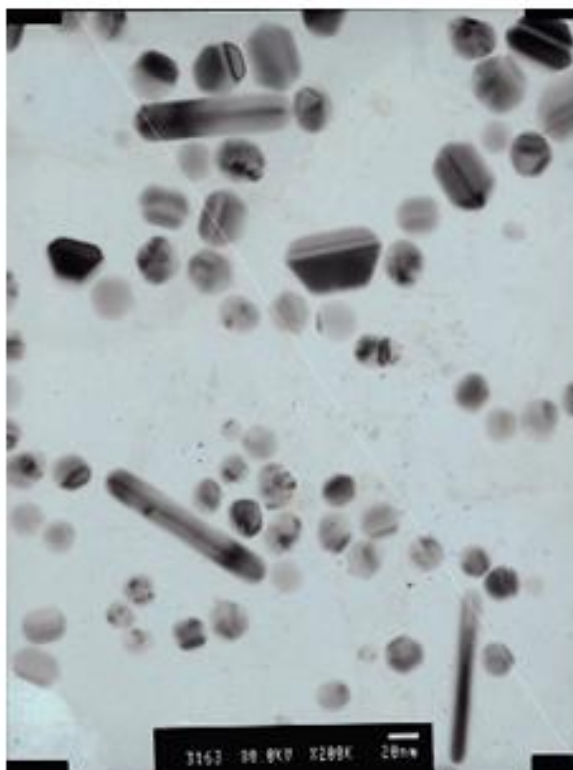


Figure 2.2: TEM image of the citrate-reduced SNPs. Adapted with permission from ref. 31. Copyright 2011 American Chemical Society.

The fiber used for the TCMMF SERS probe was purchased from Newport (model F-MLD-500). The coating process of this fiber probe was simply performed by dipping one cleaved end into CTAB-capped SNP solution for 3 hours. Scanning electron microscope (SEM, model FEI Quanta 3D FEG dual beam SEM) was used to observe the size and distribution of the SNPs coated on the fiber facet. Figure 2.3 shows that the average size of the CTAB-capped SNPs was 25 nm and the coating density on the fiber facet was 400 particles/ $\mu\text{m}^2$  [31].

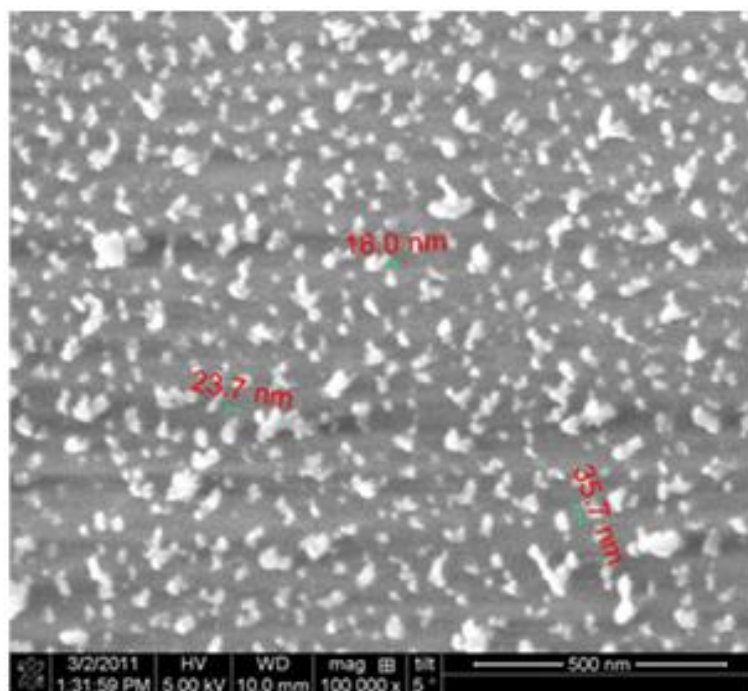


Figure 2.3: SEM image of the CTAB-capped SNPs coated on the fiber end. Adapted with permission from ref. 31. Copyright 2011 American Chemical Society.

### 2.1.3 SERS characterization and the aqueous protein detection

The SERS signals were obtained by a Renishaw Raman system (Renishaw Inc., model RM2000) with a 632.8 nm He-Ne excitation laser light. The laser power was around 2 mW, and the integration time for each SERS measurement was 10 s. In the bulk detection, the laser excitation light was directly focused onto the sample solution without using any optical fiber. During the detection with a TCMMF SERS probe, the coated tip of the TCMMF was dipped into the mixed sample solution, and the other end was placed under the microscope for coupling between the optical fiber and the laser light and collecting the SERS signal as well. Figure 2.4 shows the schematic of

the TCMMF SERS probe with an oppositely charged double-substrate “sandwich” structure operating in aqueous protein detection [31]. For the SERS measurement of R6G solution, the configuration is the same while replacing the sample solution itself.

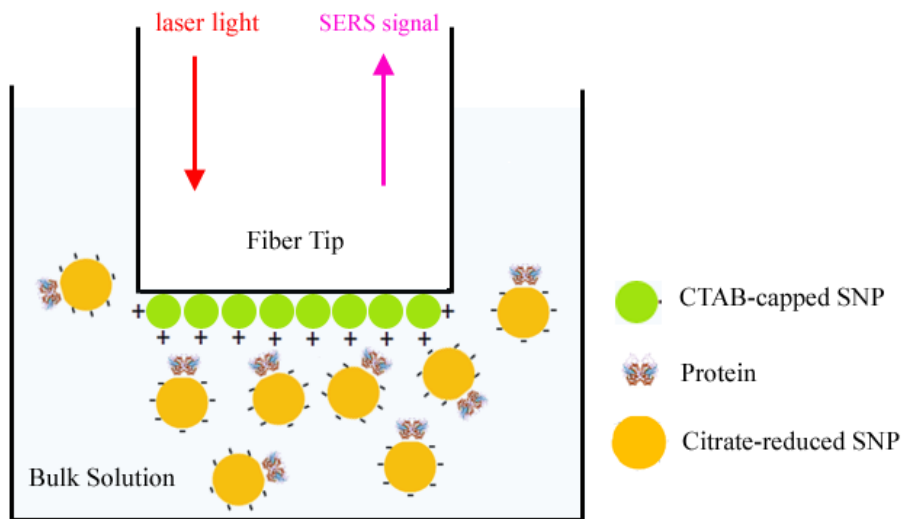


Figure 2.4: Schematic of the TCMMF SERS probe in aqueous protein detection. Adapted with permission from ref. 31. Copyright 2011 American Chemical Society.

In this work, we developed a new coating strategy by using the CTAB-capped positively charged SNPs to coat the optical fiber facet. Comparing with the previous method by Shi et al. [28], CTAB-capped SNPs have a relatively larger size (25 nm vs. 5 nm) and an opposite charge on the surface with respect to the SNPs in the bulk solution. The electrostatic force from the oppositely charged surface can decrease the gap distance between these two types of SNPs and therefore facilitate the formation of the “sandwich” structure. Since the EM field between the SNPs increases when the gap distance decreases, the shorter gap distance can result in a stronger EM field and an increased SERS signal. Moreover, both the synthesis and coating processes of

CTAB-capped SNPs are much easier and highly reproducible. The synthesis is a one-step reaction at room temperature without complex procedures. The coating can be easily done by the dip-coating for a relatively short time period due to the electrostatic force between the negatively charged silica surface of the fiber and the positively charged surface of the SNPs.

To characterize the SERS performance, Figure 2.5 shows the SERS detection of the R6G dye molecule ( $10^{-5}$  M) using both the TCMMF SERS probe and the bulk detection. It can be seen that the TCMMF probe can provide a sensitivity enhancement of 8~9 times compared to the bulk detection, which is much higher than the value of 2~3 times in our original design of the TCMMF SERS probe.

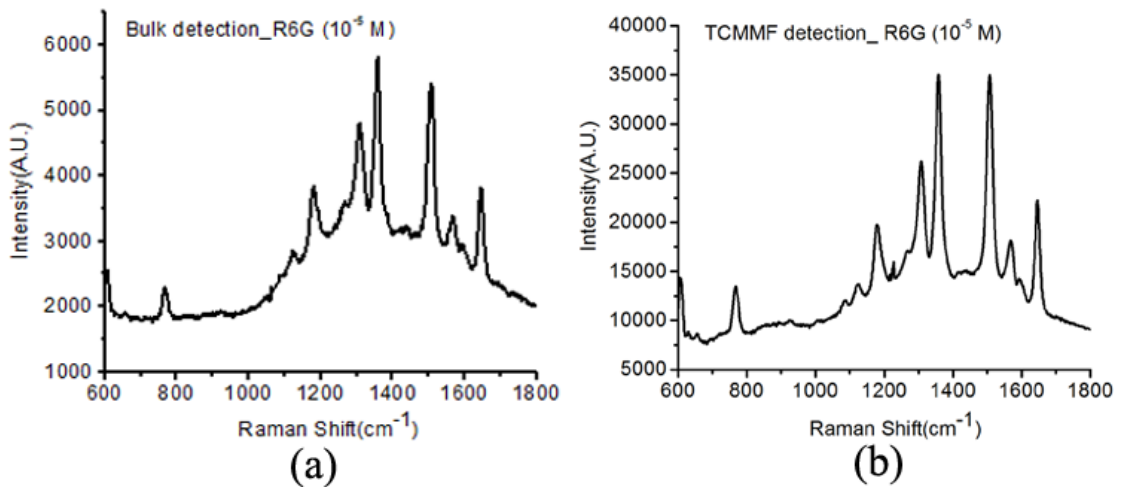


Figure 2.5: SERS spectra of R6G solution ( $10^{-5}$  M) by bulk detection and TCMMF SERS probe.

With this enhanced SERS signal, we employ this technique in the detections of the low concentration aqueous protein solutions. The complex structures of proteins

usually make it challenging to carry out direct, label-free SERS detection and the SERS signal in direct aqueous solution detection is often weak because of the small polarizability compared with dye probe molecules. As shown in Figure 2.6 and Figure 2.7 respectively [31], while the detection limit of lysozyme (one type of protein with no chromophore, purchased from Sigma-Aldrich) and cytochrome c (one type of hemoproteins, purchased from Sigma-Aldrich) by bulk detection is  $2 \mu\text{g/mL}$ , which is similar to the value of  $5 \mu\text{g/mL}$  reported previously in aqueous solution detection [56], the TCMMF SERS probe can obtain a detection limit of  $0.2 \mu\text{g/mL}$ , which is 1 order of magnitude lower than the bulk detection. This detection limit is also comparable and even a little bit lower than that using the dried protein-silver film protocol developed by Culha et al. [57]. Compared with the dried film strategy [57], the TCMMF probe developed here can offer several unique advantages: higher reproducibility, flexibility, and also in-situ remote sensing capability.

For both bulk solution and TCMMF detections, the SERS spectra of lysozyme and cytochrome c are in good agreement with that previously reported in the literature [56-58]. Table 2.1 lists the band assignments for these two proteins. For the spectra of lysozyme as shown in Figure 2.6, several major Raman peaks are observed at  $765$  (Trp),  $1359$  (Trp),  $1442$  ( $\text{CH}_2$  scissoring),  $1508$  (Phe, His, Trp), and  $1646 \text{ cm}^{-1}$  (amide I). In the TCMMF detection, an additional strong peak at  $1304 \text{ cm}^{-1}$  was observed and can be assigned to  $\text{CH}_2$  wagging mode. It is also noticed that some of the peaks have different signal sensitivity enhancements when using the TCMMF. On average, the signal sensitivity enhancement is  $\sim 10$  times for lysozyme. However, the signal

sensitivity enhancement for the  $1508\text{ cm}^{-1}$  peak is  $\sim 18$  times while that for the  $1442\text{ cm}^{-1}$  peak is  $\sim 5$  times. Both the new emerging peak and different signal sensitivity enhancements for different peaks in TCMMF are mainly attributed to the redistribution of EM field by the double-substrate “sandwich” structure. For example, the strongest EM field associated with a single nanoparticle is near the surface, while the strongest EM field associated with a dimer system of nanoparticles is inside the gap. Some segments of the protein that are not the closest to the surface of the citrate-reduced SNPs can lie in the gap which results in a much stronger enhancement. Therefore, the SERS signal enhancements can be different depending on their positions in the new SERS substrate. And with this additional information, it can help us have a better understanding of the adsorption of the protein on the metal surface.

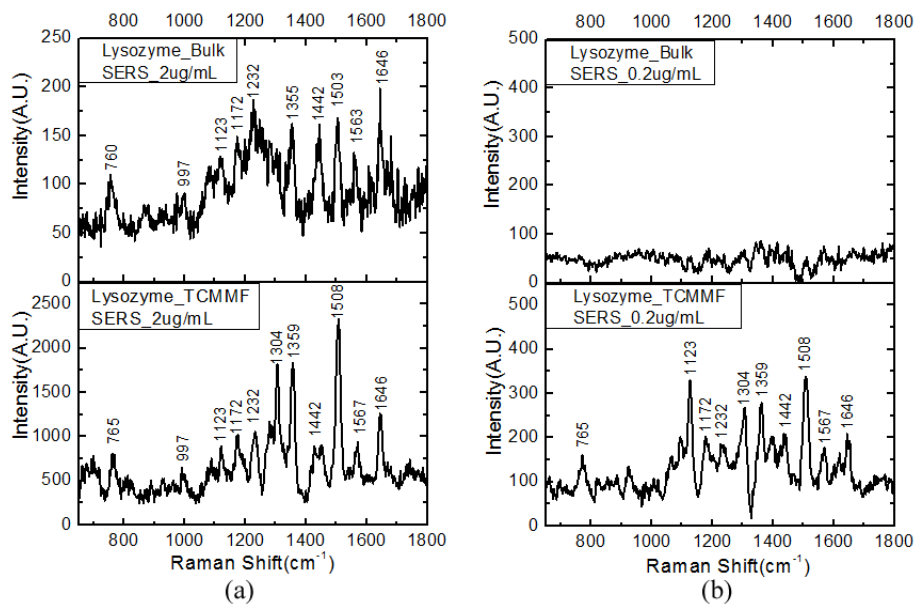


Figure 2.6: SERS spectra of lysozyme detected by bulk solution and TCMMF probe at different concentrations: (a)  $2\text{ }\mu\text{g/mL}$ ; (b)  $0.2\text{ }\mu\text{g/mL}$ . Adapted with permission from ref. 31. Copyright 2011 American Chemical Society.

For the SERS spectra of cytochrome c as shown in Figure 2.7, major Raman peaks are observed at  $1121\text{ cm}^{-1}$  ( $\text{NH}_3^+$  deformation),  $1230\text{ cm}^{-1}$  (Amide III),  $1313\text{ cm}^{-1}$  ( $\text{CH}_2$  wag),  $1363\text{ cm}^{-1}$  (Trp),  $1392\text{ cm}^{-1}$  ( $\text{COO}^-$  symmetric stretching),  $1554\text{ cm}^{-1}$  (Trp), and  $1622\text{ cm}^{-1}$  (Amide I). Similar to what occurred in lysozyme detection, some additional peaks are observed at  $821\text{ cm}^{-1}$ ,  $1197\text{ cm}^{-1}$ , and  $1330\text{ cm}^{-1}$  and can be assigned to Try, Try and Phe, and Trp respectively. And the sensitivity enhancement varies for different peaks with an average enhancement factor of 7.

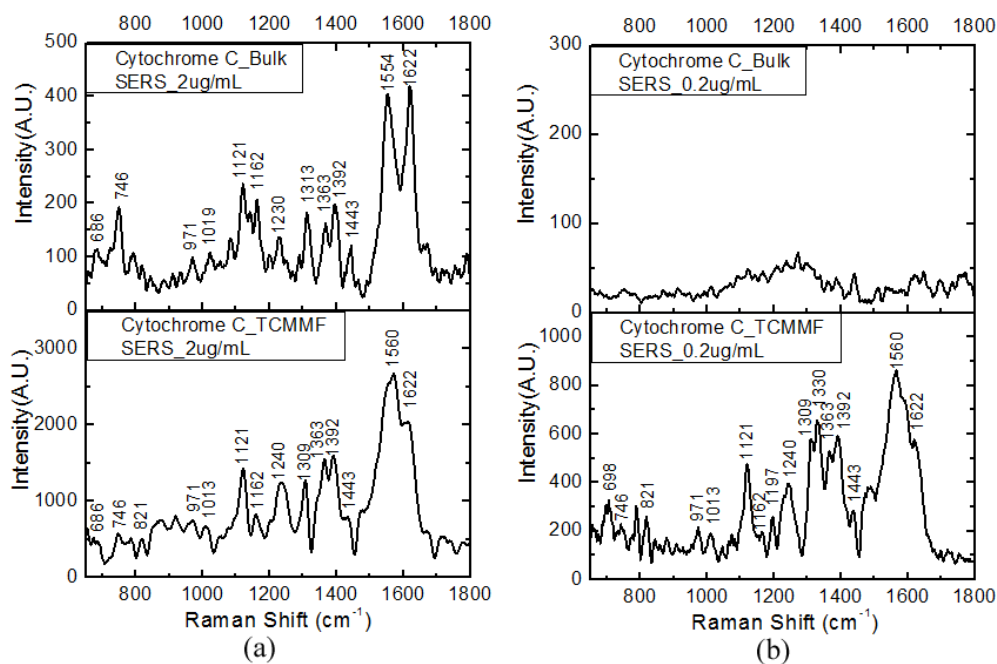


Figure 2.7: SERS spectra of cytochrome c detected by bulk solution and TCMMF probe at different concentrations: (a)  $2\text{ }\mu\text{g/mL}$ ; (b)  $0.2\text{ }\mu\text{g/mL}$ . Adapted with permission from ref. 31. Copyright 2011 American Chemical Society.

In conclusion, we have demonstrated a TCMMF SERS probe with a new double substrate “sandwich” structure by using the oppositely charged SNPs. We implement

this technique in the detections of the proteins lysozyme and cytochrome c in aqueous solutions and achieve a detection limit of 0.2  $\mu\text{g/mL}$ , which is one order of magnitude lower than that reported previously. High sensitivity, flexibility, and also in-situ remote sensing capability make this fiber probe promising in practical applications of label-free SERS detections of biomolecules.

Table 2.1. Band assignments for lysozyme and cytochrome c. Adapted with permission from ref. 31. Copyright 2011 American Chemical Society.

Lysozyme	Cytochrome c	Band Assignments
-----	686, 698	Same as reported <sup>17,19</sup>
760, 765	746	Trp
-----	821	Try
-----	971	C-C stretching
997	1019, 1013	Phe
1123	1121	$\text{NH}_3^+$ deformation
1172	1162	Try
-----	1197	Try+Phe
1232	1230, 1240	Amide III
1304	1313, 1309	$\text{CH}_2$ wagging
-----	1330	Trp
1355, 1359	1363	Trp
-----	1392	$\text{COO}^-$ symmetric stretching
1442	1443	$\text{CH}_2$ scissoring
1503, 1508	-----	Phe, his, trp
1563, 1567	1554, 1560	Trp
1646	1622	Amide I

## 2.2 Fiber SERS sensor fabricated by interference lithography

As mentioned in Section 1.2, to achieve high uniformity, high reproducibility, and potential mass production, it is desirable to implement lithography techniques in the

fabrication of fiber SERS probes. However, there are different technical drawbacks for the existing lithography techniques that have been applied to the nanofabrication of fiber SERS probes. Moreover, the sensitivities of these fiber probes reported in the literature are relatively low [35-37]. On the other hand, interference lithography (IL) has been used to fabricate waveguide grating structures on the facet of an optical fiber for refractive-index sensing, but no SERS-active substrate fabricated on the fiber facet with similar approach has ever been reported [59]. In this Section, we will present a highly sensitive fiber SERS sensor with the nanopillar array structure on the fiber facet, which is fabricated by IL technique [60].

### **2.2.1 Fabrication of IL-defined nanopillar array on the fiber facet**

In order to implement the IL fabrication technique on the fiber facet, the main challenge is how to control the position and orientation of the optical fiber tip in the processes of spin coating, lithography, etching, and vapor deposition, as the fiber has a small diameter and a large aspect ratio. In this work, we successfully fabricated the nanopillar array on the facet of a regular multimode optical fiber by mounting the fiber with the help of a fiber ferrule and employing IL to pattern the nanopillar array onto the fiber facet [60].

The fiber SERS probe was fabricated using a standard silica multimode optical fiber (OFS Fitel, LLC., model: BF06864, NA = 0.22), with a 50  $\mu\text{m}$  core diameter and a 125  $\mu\text{m}$  cladding diameter. The typical fiber length used in the study was around 10 cm. As shown in Figure 2.8, a custom-designed ceramic fiber ferrule was

attached at one fiber end for the spin coating processes. The fiber ferrule had an outer diameter of 3 mm and was 12 mm long. The epoxy gap between the optical fiber and the fiber ferrule was less than 2  $\mu\text{m}$  and the whole area of the ferrule including the fiber was polished with 0.02  $\mu\text{m}$  polishing film. This procedure of attaching a fiber ferrule at the fiber end is a standard process in fiber-optic industry and therefore the fiber sample can be easily fabricated at low-cost and high throughput. Figure 2.8 (b) and (c) show the photograph and SEM images of the fiber ferrule respectively.

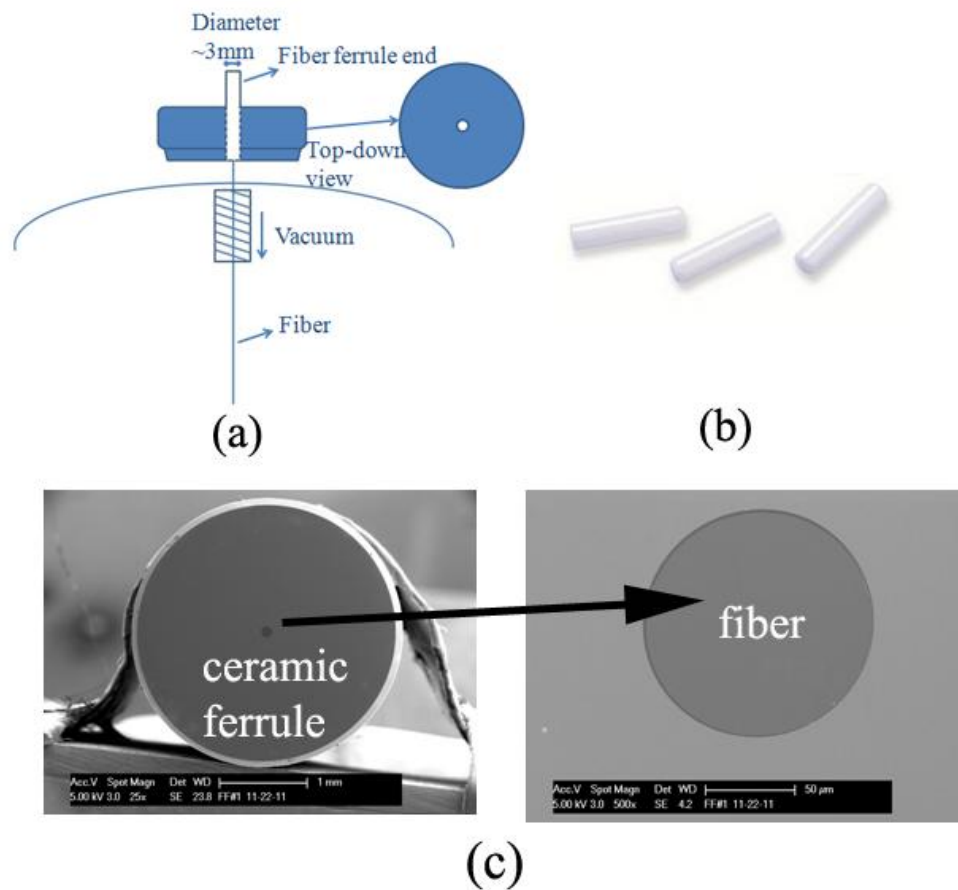


Figure 2.8: (a) Schematic of the spin coating process for the optical fiber sample; (b) photograph of the fiber ferrule; (c) SEM images of the fiber ferrule facet. Adapted with permission from ref. 60. Copyright 2012 Optical Society of America.

To prepare for the laser exposure of IL, the fiber facet with the fiber ferrule was first spin coated with a 260 nm thick antireflection layer and then coated with a 700 nm thick photoresist. The nanopillar array was then fabricated onto the fiber facet by IL, using the same method as that in the fabrication of similar array on 4-inch fused silica wafers in our previous studies [61-64]. Figure 2.9 shows the schematic of two-beam IL setup. The laser wavelength for IL was 413 nm and the dose was about 80 mJ/cm<sup>2</sup>. The fabricated photoresist pattern was a two-dimensional periodic nanopillar array with a 317 nm pitch and a 160 nm pillar diameter.

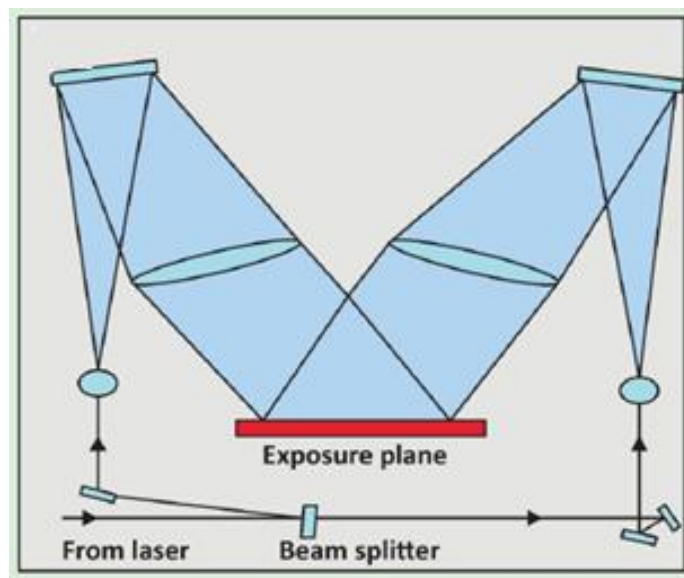


Figure 2.9: Schematic of the two-beam interference lithography set-up.

An ion milling deep reactive ion etching step was applied to remove the antireflection layer between the photoresist nanopillars (mask), after which the unprotected fused silica area was etched down to 600 nm and then the residual

photoresist mask on the top of the nanopillars was washed away. Finally a 60 nm layer of silver was e-beam evaporated at a deposition rate of 0.1 nm/s onto the fiber facet at an angle of 60 °to make it as a SERS-active substrate.

Figure 2.10 shows the SEM images of the silver-coated nanopillar array fabricated on the fiber core area. It can be seen that the patterned nanopillar array has a high uniformity which allows for the robustness and reproducibility of the measurement. Due to the 60 °angle deposition, the nanopillars are mainly coated by the silver on one side and the strong “shadowing” effect causes much less silver on the substrate surface (at the bottom of the nanopillars), which is crucial in reducing the detrimental metal absorption for the remote end SERS detection.

### **2.2.2 Optical and SERS characterization of the fiber SERS probe**

Trans-1,2-bis(4-pyridyl)-ethylene (BPE) powder (purity > 99.9%) was obtained commercially through Sigma-Aldrich. For the preparation of BPE SERS measurement, it followed a procedure described previously in the literature [65]: the patterned fiber facet was submerged in 5 mM BPE solution in methanol for 24 hours, then gently rinsed in methanol, and dried under a stream of nitrogen.

For the SERS measurements to characterize the fiber SERS probe, two configurations were used in this study [60]. One was the front end detection, in which the laser light was focused directly by the objective lens (20×, NA = 0.40) onto the patterned fiber facet and the SERS signal was collected in a backscattering geometry. The other was remote end detection, which is the typical optrode geometry used for

remote sensing: the laser light was coupled from the unpatterned fiber end, propagated through the fiber, and triggered the SERS activity at the patterned remote facet; the SERS signal was then obtained from the distal fiber end and finally coupled back to the Raman spectrometer through the fiber. The SERS measurements were performed using a Renishaw InVia Raman Microscope system and the excitation wavelength was 514 nm with an Argon ion laser. In this study, all the spectra were baseline corrected to remove the broad fiber background unless otherwise mentioned.

For the optical characterization of the fiber SERS probe, reflectance spectra were measured in both the front end and the remote end configurations using Nanospec reflectometer with a white light source illumination. Figure 2.11 shows that there is a SPR at 558 nm for the front end configuration and a SPR at 537 nm for the remote end configuration. In the remote end configuration, the broader and deeper resonance dip is attributed to the excitation of the nanopillar array on the whole fiber core area (diameter: 50  $\mu\text{m}$ ) instead of only the ones at the focal spot (diameter: 20  $\mu\text{m}$ ), while the lower overall reflectivity is mainly caused by the coupling loss. In addition, there is a difference in numerical aperture that needs to be accounted for different angles of excitation involved; the numerical aperture changes from 0.40 to 0.22 in the front and remote end configuration, respectively. More crucially, we think that the difference in the wavelength position of SPR in the two configurations is mainly due to the asymmetry of this complex 3D dielectric-metal structure with respect to the excitation (especially in the out-of-plane z-direction). In order to optimize the enhancement for both the excitation laser and the Raman scattered signal, we have chosen 514 nm

laser light to excite the surface plasmon and activate the SERS signal in our experiment.

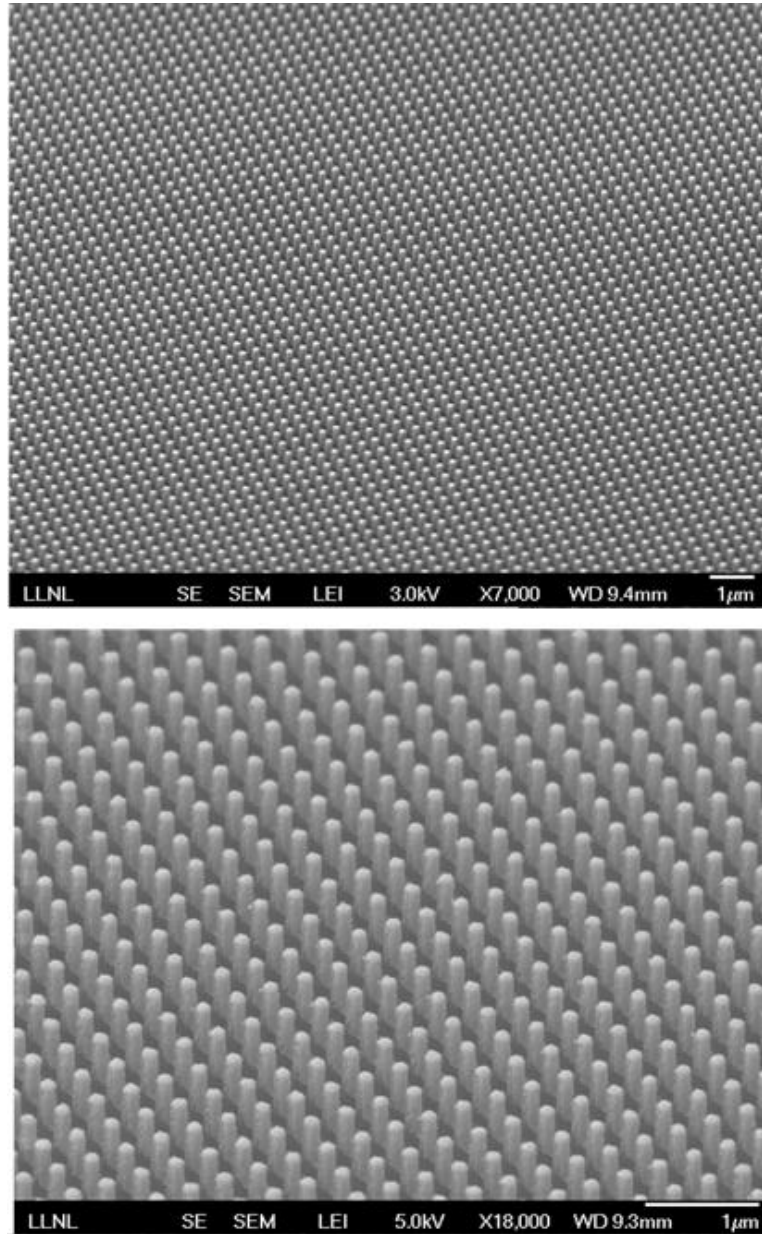


Figure 2.10: SEM images of the silver-coated nanopillar array patterned on the fiber core (tilted view: 45 °). Adapted with permission from ref. 60. Copyright 2012 Optical Society of America.

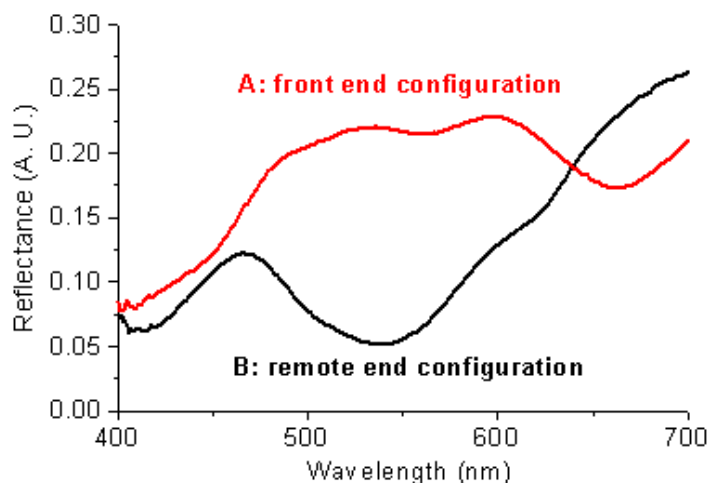


Figure 2.11: Reflectance spectra of the fiber SERS probe in both the front end configuration (A) and remote end configuration (B). Adapted with permission from ref. 60. Copyright 2012 Optical Society of America.

Figure 2.12(a) shows the SERS spectra of BPE monolayer measured in both the front end and the remote end configurations with a laser power of 0.2 mW and an integration time of 10 s. Both plots show the characteristic SERS peaks of BPE at  $1200\text{ cm}^{-1}$  (C=C stretching),  $1604\text{ cm}^{-1}$  (aromatic ring stretching), and  $1635\text{ cm}^{-1}$  (in-plane ring mode), which are consistent with that reported in the literature [66]. For the remote end configuration, the SERS signal intensity is around 1/5 of that obtained in the front end configuration. The bulk Raman spectrum of 0.1 M BPE solution in methanol is shown in Figure 2.12(b), which is obtained with a laser power of 2 mW and an integration time of 10 s. Besides the three main peaks from BPE, the broad peak at  $1456\text{ cm}^{-1}$  is from the methanol solvent. While the remote end configuration is more useful in practical sensing applications, characterization from the front end

configuration can provide a more direct measurement of the enhancement factor (EF) of the SERS substrate itself to give an indication of the quality and performance of our substrate as compared to other technologies. Therefore, in order to characterize the SERS performance of this fiber probe, we calculate the EF based on the front end configuration using the following expression:

$$EF = \frac{I_{SERS}}{I_{Raman}} \cdot \frac{P_{Raman} \cdot T_{Raman}}{P_{SERS} \cdot T_{SERS}} \cdot \frac{N_{Raman}}{N_{SERS}} \quad (2.1)$$

where  $I_{SERS}$  is the SERS intensity,  $I_{Raman}$  is the Raman intensity,  $P_{SERS}$  and  $P_{Raman}$  are the laser power for SERS measurement and Raman measurement respectively,  $T_{SERS}$  and  $T_{Raman}$  are the integration time for SERS measurement and Raman measurement respectively,  $N_{SERS}$  and  $N_{Raman}$  are the number of BPE molecules involved for SERS measurement and Raman measurement, respectively.

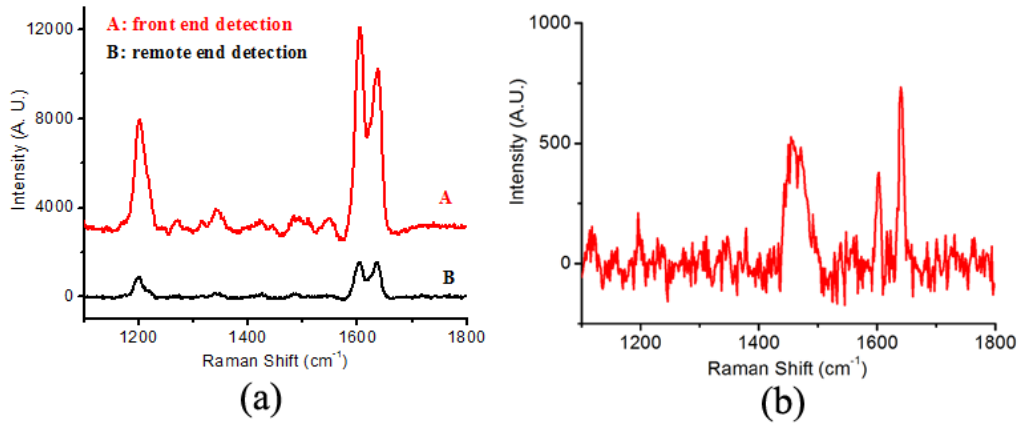


Figure 2.12: a) SERS spectra of BPE monolayer using the fiber SERS probe in both the front end configuration and remote end configuration (laser power: 0.2 mW, integration time: 10 s); (b) Raman spectrum of 0.1 M BPE obtained with the same spectroscopy system (laser power: 2 mW, integration time: 10 s). Adapted with permission from ref. 60. Copyright 2012 Optical Society of America.

Choosing the  $1200\text{ cm}^{-1}$  SERS band as a reference, the SERS intensity underneath this band is calculated to be 126157 (counts), while the Raman intensity underneath this band is calculated to be 1246 (counts). We estimate a monolayer coverage density for BPE on silver surface to be  $10^{14}$  molecules/cm<sup>2</sup> [65]. The depth of focus is around 200  $\mu\text{m}$  for our system. The number of molecules in SERS measurement is the molecular coverage density ( $10^{14}$  molecules/cm<sup>2</sup>) multiplied by the metal surface area within the laser beam spot area (diameter:  $\sim 5\ \mu\text{m}$ ). The number of molecules in Raman measurement is the molecular concentration used in the study multiplied by the total interaction volume, which is estimated to be the laser beam spot area multiplied by the depth of focus. Therefore, the EF value is calculated to be  $1.2 \times 10^7$  for the front end configuration. This value is a little bit lower than that (on the order of  $\sim 10^8$ ) achieved previously on our fused silica substrates [62, 64]. One possible reason is that in order for the remote sensing application, there is a potential tradeoff between minimizing the metal absorption loss and maximizing the SERS enhancement. Therefore, the metal deposition angle and coating thickness used in this study are different from that used previously [62, 64]. Moreover, the geometry of the nanopillar in this study has not been optimized yet. However, comparing to other existing technologies such as the EBL-transfer technique developed by Capasso et al. [35], which has an EF value of  $2.6 \times 10^5 \sim 5 \times 10^5$  for the front end configuration, our probe has a much higher sensitivity as a fiber SERS sensor.

### **2.2.3 Vapor SERS detection**

Recently, Chang et al. have demonstrated that the nanopillar array SERS substrate on fused silica wafer can be used for the toluene vapor detection [64]. Therefore, it is very straightforward to implement this technique on the optical fiber for the vapor remote sensing applications. In this study [60], toluene liquid (purity > 99.9%) was obtained commercially through Sigma-Aldrich. For the toluene vapor SERS detection, the fiber facet was placed above the toluene liquid surface. The concentration of the toluene vapor was estimated to be 2%-3% at room temperature.

Curve A in Figure 2.13 shows the fiber SERS probe used in the remote detection of the toluene vapor (2~3%). In this experiment, the excitation laser power was 2 mW and the integration time was 10 s. It can be clearly seen that both the  $1002\text{ cm}^{-1}$  and  $1597\text{ cm}^{-1}$  peaks (C=C stretching) are detectable. Curve B in Figure 2.13 shows a comparison experiment in which an unpatterned optical fiber without the silver coating in the toluene vapor using the same configuration cannot detect any signal. And we also tried a patterned fiber without the silver coating and an unpatterned fiber with the silver coating, both of which did not result in any detectable toluene signal.

Besides the organic solvent vapors such as toluene, another important type of target analytes in the gas sensing applications is the explosive, which is of paramount importance for both the environmental control and the national security. Therefore, in this study, we also chose 2,4-dinitrotoluene (DNT) vapor as the test molecule. DNT was purchased from Sigma-Aldrich. Similar to that in toluene vapor experiment, the fiber facet was placed above the pure DNT sample surface. The concentration of the

DNT vapor was estimated to be ~100 ppb at room temperature. The laser power was 2 mW and the integration time was 10 s.

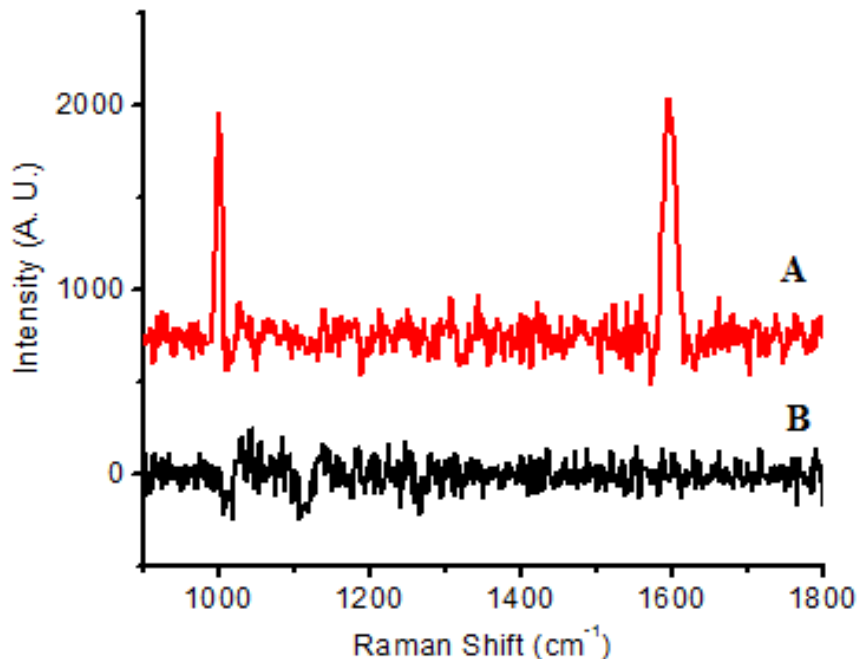


Figure 2.13: Curve A: the SERS spectrum of the fiber probe for the remote detection of toluene vapor (laser power: 2 mW, integration time: 10 s); Curve B: the spectrum obtained by the unpatterned optical fiber in the toluene vapor with the same system configuration. Adapted with permission from ref. 60. Copyright 2012 Optical Society of America.

Curve A in Figure 2.14 shows the SERS spectrum of the patterned fiber SERS probe in the remote detection of ~100 ppb DNT vapor. Comparing to the reference spectrum in which there is no DNT vapor exposure for the fiber probe, a broad peak at  $1353\text{ cm}^{-1}$  is observed. This peak is assigned as the DNT signature peak and corresponds to  $\text{NO}_2$  stretching modes in the DNT molecule. In this spectrum, the fiber

(fused silica) background hasn't been removed by the baseline correction and the other broad peaks at both  $1050\text{ cm}^{-1}$  and  $1200\text{ cm}^{-1}$  come from the fiber background.

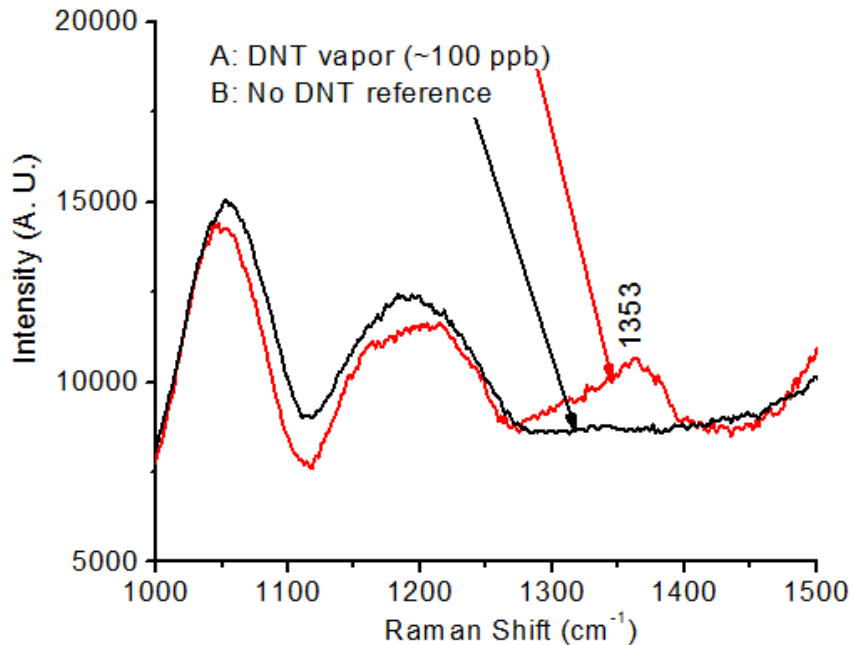


Figure 2.14: Curve A: the SERS spectrum of the fiber probe for the remote detection of DNT vapor (laser power: 2 mW, integration time: 10 s); Curve B: the spectrum obtained by the same optical fiber without any DNT vapor exposure with the same system configuration.

With the high sensitivity provided by the silver-coated nanopillar array SERS substrate on the fiber facet, this is the first time, to the best of our knowledge, that a single conventional multimode optical fiber SERS sensor can be used for the remote detection of the vapor/gas samples at room temperature. This key component could facilitate the development of a highly-sensitive integrated portable all-fiber based SERS sensing system for remote environmental control in the future work.

### 2.2.3 Simulation analysis

To have a better understanding of both the optical and SERS performance of the fiber probe, simulation analysis was performed using commercial EM modeling software COMSOL Multiphysics 4.2. Figure 2.15 shows the geometry of the unit cell in our simulation model. The unit cell has a pitch size of 313 nm. The purple region shown in Figure 2.15(a) corresponds to the fused silica on the fiber facet: the height of the fused silica region at the bottom is 250 nm; the fused silica nanopillar is a cylinder with a radius of 75 nm and a height of 600 nm plus a “cap” whose height (the difference between the top of whole nanopillar and the top of the cylinder) is 50 nm. The blue region shown in Figure 2.15(b) corresponds to the silver coating on the fused silica nanopillar: due to the “shadowing” effect of the high angle deposition, the silver is coated on one side of the nanopillar and the coating thickness on the edges is much less than the total metal coating thickness. The maximum silver thickness which lies in the  $y=0$  plane in this case is 60 nm while the minimum silver thickness which lies in the  $x=0$  plane in this case is 20 nm. Also, there is a “semi-ellipsoid” silver “cap” on the top of the pillar, the thickness of the silver coating is 60 nm, 20 nm, 60 nm in  $x$ ,  $y$ ,  $z$  directions, respectively. The rest of the unit cell is the air region and the total height of the air region is 900 nm.

Since the reflectance measurements are taken with the white light source, all polarization states need to be considered. In this model, we chose a fixed polarization state which is along the  $x$  axis while changing the direction of silver coating on the nanopillar to simulate the different polarization states instead since it is much easier to change the geometry than the excitation for the parametric sweep.  $\beta$  is the angle

between the edge of metal coating and the y axis. Fig 2.15(b) actually shows the case when  $\beta = 0^\circ$ . In this study we consider a series of  $\beta$  values which are  $0^\circ$ ,  $-15^\circ$ ,  $-30^\circ$ ,  $-45^\circ$ ,  $-60^\circ$ ,  $-75^\circ$ ,  $-90^\circ$ . And Fig 2.16 (a) and (b) show  $\beta = -45^\circ$  and  $\beta = -90^\circ$  respectively.

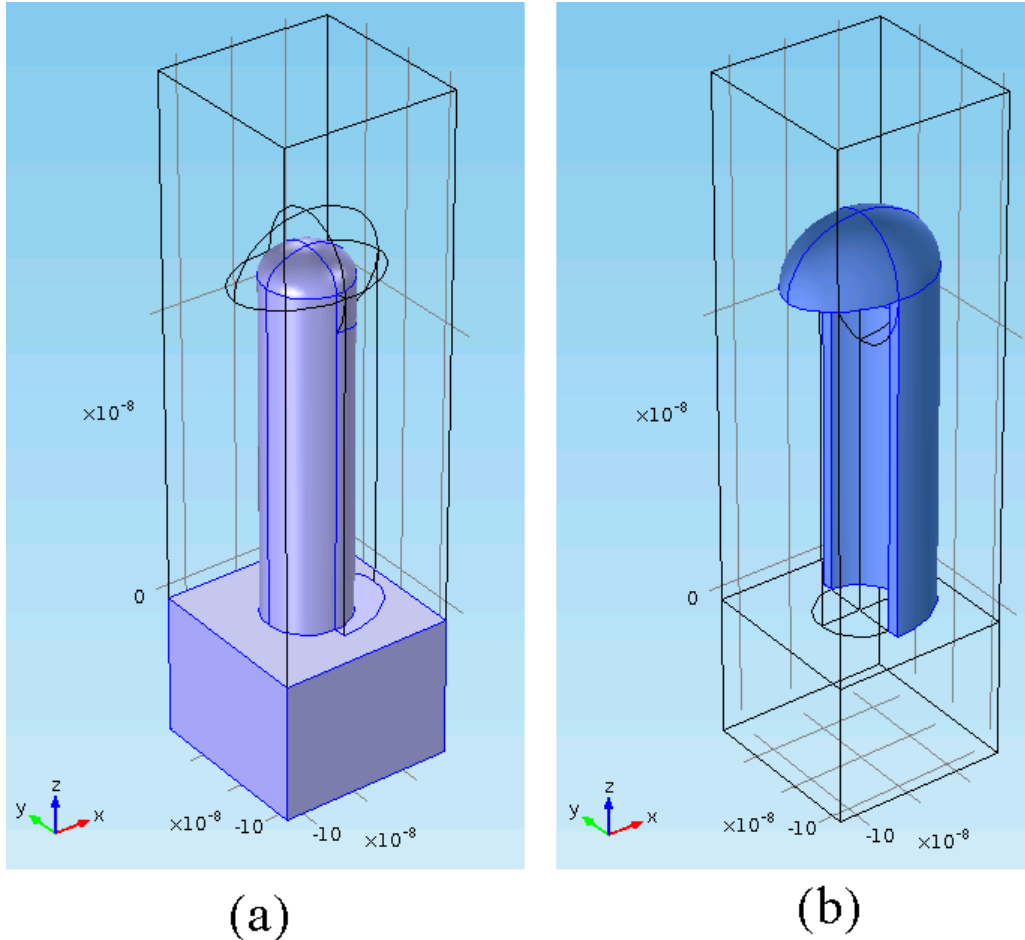


Figure 2.15: Geometry of the unit cell in the simulation model: (a) the purple region corresponds to the fused silica on the fiber facet; (b) the blue region corresponds to the silver coating on the fused silica pillar; the rest of the unit cell is the air region.

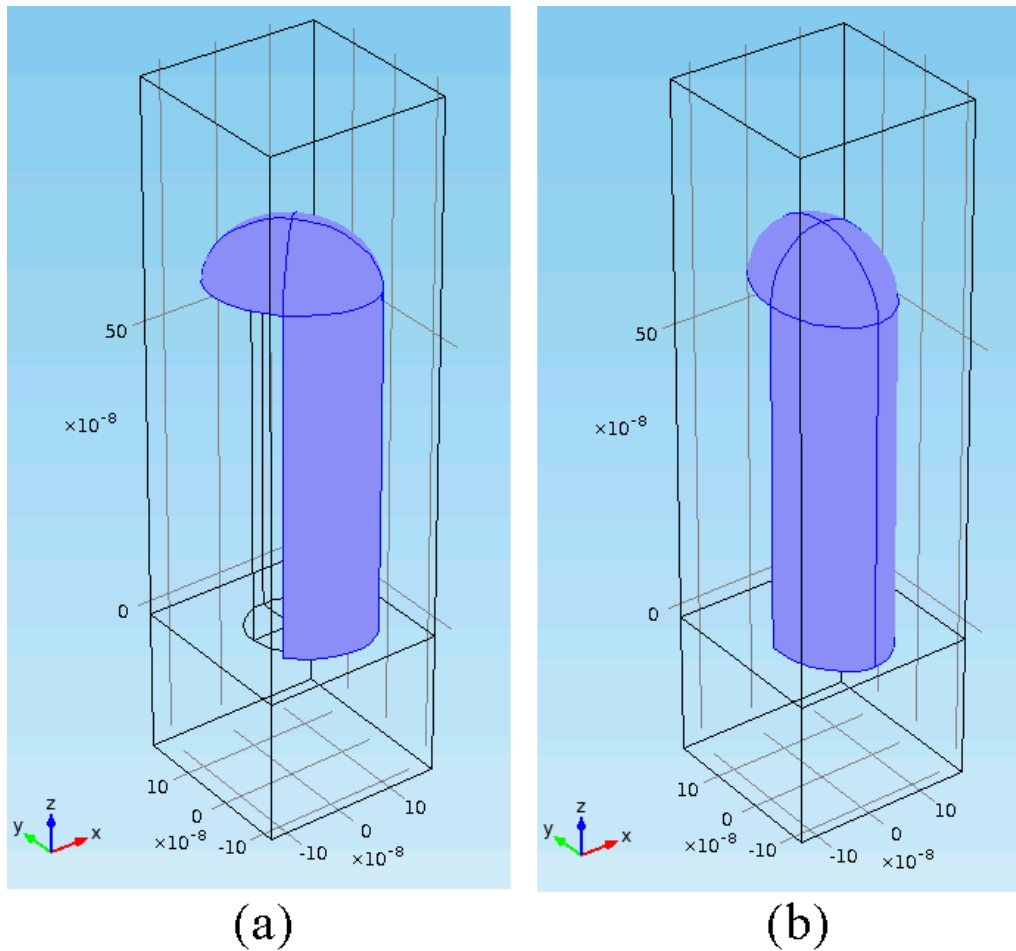


Figure 2.16: Geometry of the unit cell in the simulation model with different directions of the metal coating: (a)  $\beta = -45^\circ$ ; (b)  $\beta = -90^\circ$

The excitation light is at normal incidence coming from either the top or the bottom, which corresponds to the front end configuration and the remote end configuration, respectively. Figure 2.17 shows the simulated reflectance spectrum for the front end configuration averaged from all the cases with different  $\beta$  values ( $0^\circ$ ,  $-15^\circ$ ,  $-30^\circ$ ,  $-45^\circ$ ,  $-60^\circ$ ,  $-75^\circ$ ,  $-90^\circ$ ). Two resonances are observed at 540 nm and 640 nm, which are very close to that (558 nm and 661 nm) measured experimentally as shown

in Figure 2.11. It is also noticed that the depth ratio of two resonances in the simulation result matches pretty well with the experimental result.

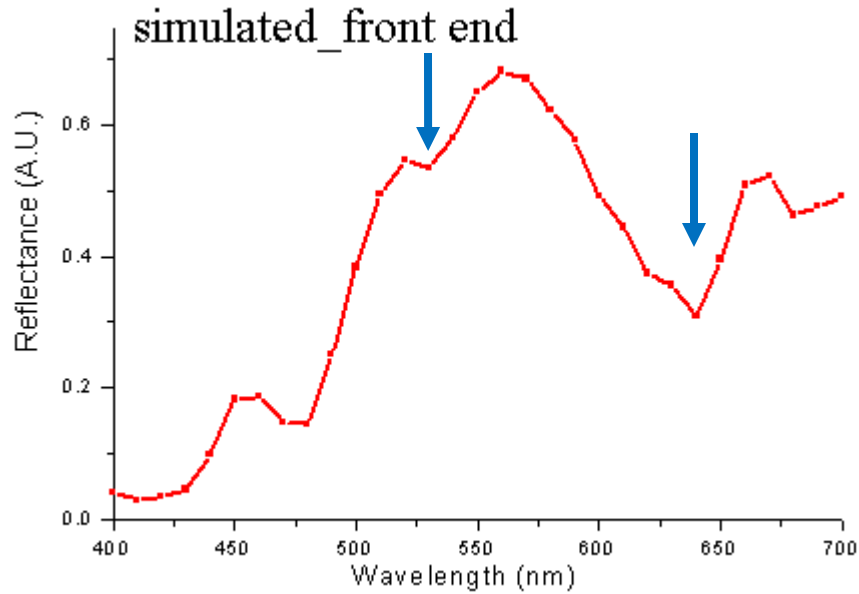


Figure 2.17: Simulated reflectance spectrum for the front end configuration.

Figure 2.18 shows the simulated reflectance spectrum for the remote end configuration averaged from all the cases with different  $\beta$  values ( $0^\circ$ ,  $-15^\circ$ ,  $-30^\circ$ ,  $-45^\circ$ ,  $-60^\circ$ ,  $-75^\circ$ ,  $-90^\circ$ ). Two resonances are observed at 530 nm and 620 nm, which are also similar that (537 nm and 611 nm) measured experimentally as shown in Figure 2.11.

Since the 3-D geometry involved in this study is quite complex, the modes for the corresponding resonances are hybrid ones, which are out of the scope of the current study. However, based on the reflectance spectra, we can have a better understanding of the silver-coated nanopillar geometry. For example, it's quite challenging to measure the height of the top “cap” and the minimum silver thickness on the edges

based on SEM images. By tuning these geometry parameters in the simulation model to match what measured experimentally, the values of these geometry parameters can be roughly estimated.

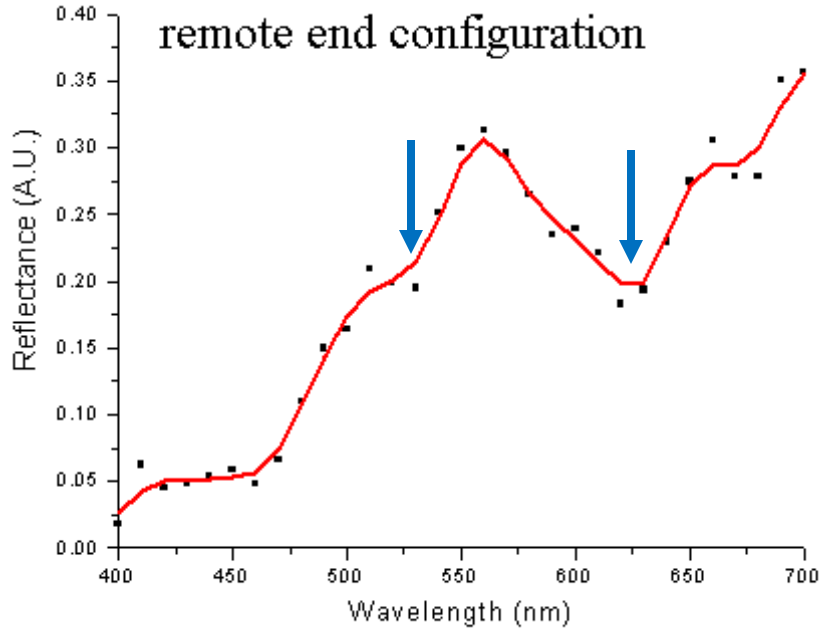


Figure 2.18: Simulated reflectance spectrum for the remote end configuration.

More importantly, using the finalized nanopillar geometry based on the reflectance spectra, we can decipher the EM distribution in this complex 3-D geometry. Figure 2.19 and Figure 2.20 show the EM distributions on  $z=0$ ,  $x=0$ , and  $y=0$  planes when  $\beta$  is  $0^\circ$  and the wavelength is 550 nm in the front end configuration and the remote end configuration, respectively. It can be seen that in both configurations the maximum electrical field is near the sharp edges on  $z = 0$  plane, which corresponds to the localized surface plasmon. The maximum field enhancement is 50.6 and 48.2 in the front end configuration and the remote end configuration, respectively. Also, there are

a large number of “hotspots” along the sharp edges as shown in Figure 2.19(b) and Figure 2.20(b). In addition, there is a propagating surface plasmon along the z direction as shown in Figure 2.19(c) and Figure 2.20(c).

Based on the results shown in Figure 2.19 and Figure 2.20, it can be seen that the nanopillar structure can be considered as a 3-D high-density SERS-active substrate and therefore can provide a much higher sensitivity than the conventional 2-D substrates. Actually this is the main reason for the high sensitivity of the fiber SERS probe which could push the in-situ remote detection of gas-phase molecules.

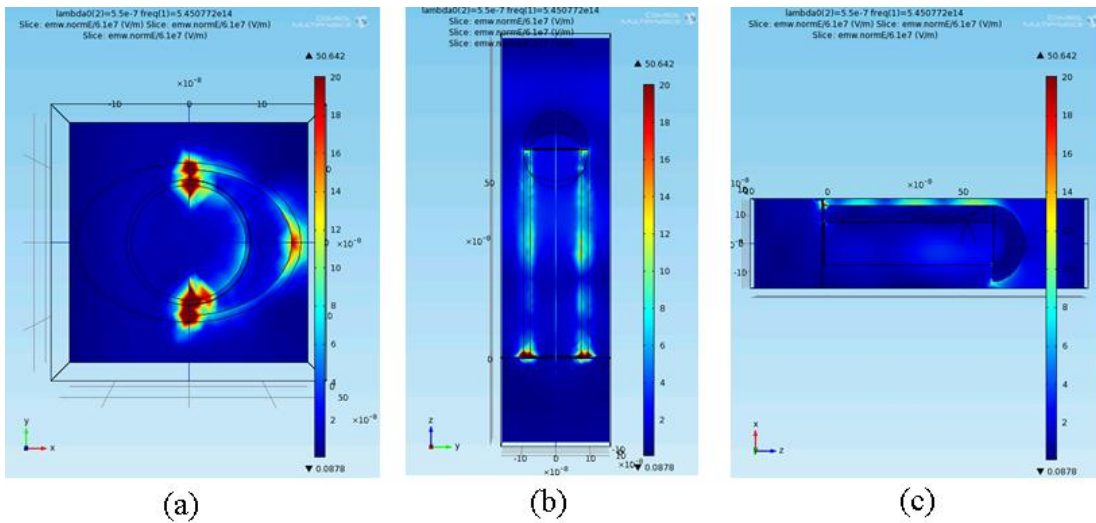


Figure 2.19: Simulated EM distribution in the front end configuration ( $\beta = 0^\circ$ ,  $\lambda = 550$  nm): (a)  $z = 0$  plane; (b)  $x = 0$  plane; (c)  $y = 0$  plane.

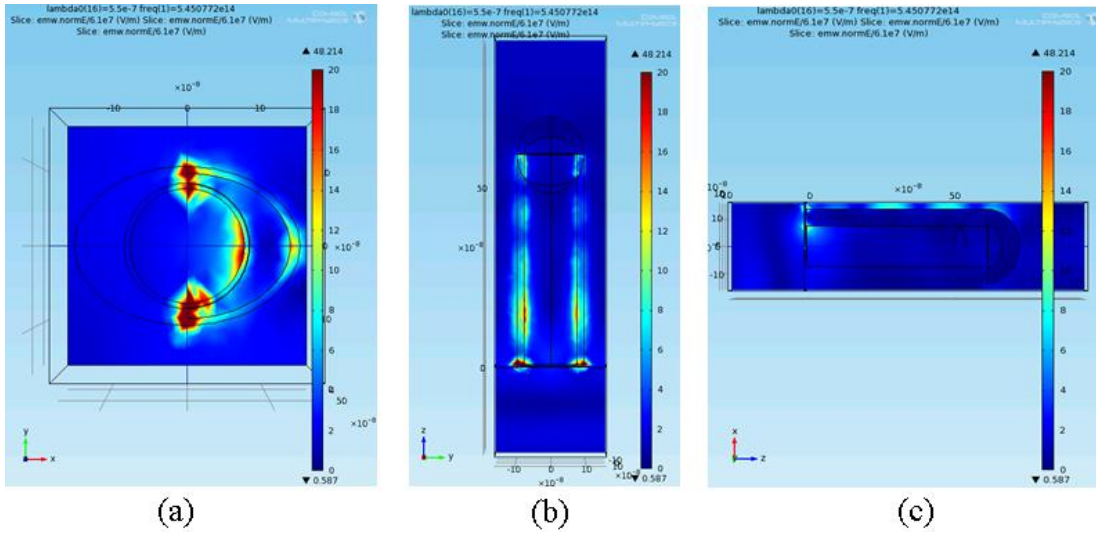


Figure 2.20: Simulated EM distribution in the remote end configuration ( $\beta = 0^\circ$ ,  $\lambda = 550 \text{ nm}$ ): (a)  $z = 0$  plane; (b)  $x = 0$  plane; (c)  $y = 0$  plane.

# Chapter 3. Photonic crystal fiber sensors

## 3.1 Gas Raman detection

Currently there is a growing interest in developing compact and reliable sensors for gas detection in applications for environmental control. While global air quality monitoring is usually involved with the detection of trace chemicals such as greenhouse gases (e.g., carbon dioxide), local air quality monitoring often requires the detection of toxic gases, explosives, hydrocarbon gases, and malodors. Most of the existing gas sensors tend to be bulky, expensive, relatively inaccurate, unable to provide real-time data, or non-molecular specific. Particularly, highly sensitive multiplexed gas sensing is challenging due to the lack of molecular specificity in most detection techniques.

With the advantage of molecular specificity, RS has been applied to analyze the composition of gaseous samples [2]. However, it is very challenging to analyze the low concentration gases due to the small Raman cross Sections and resultant low signal strengths. Since the HCPCF probe provides an ideal sensing platform both the excitation laser and the gaseous sample, we have used the HCPCF for gas Raman detection in our study [48].

### 3.1.1 Experimental set-up of HCPCF gas Raman detection

The HCPCF used in our experiment was purchased from Thorlabs Inc. (Model HC-800B) with its cross Section shown in the top right of Figure 3.1 [48]. The central

core diameter is 7.5  $\mu\text{m}$  and the cladding pitch is 2.3  $\mu\text{m}$ . The fiber has a low transmission loss in the wavelength range of 735 nm to 915 nm, as shown in Figure 3.2 [67].

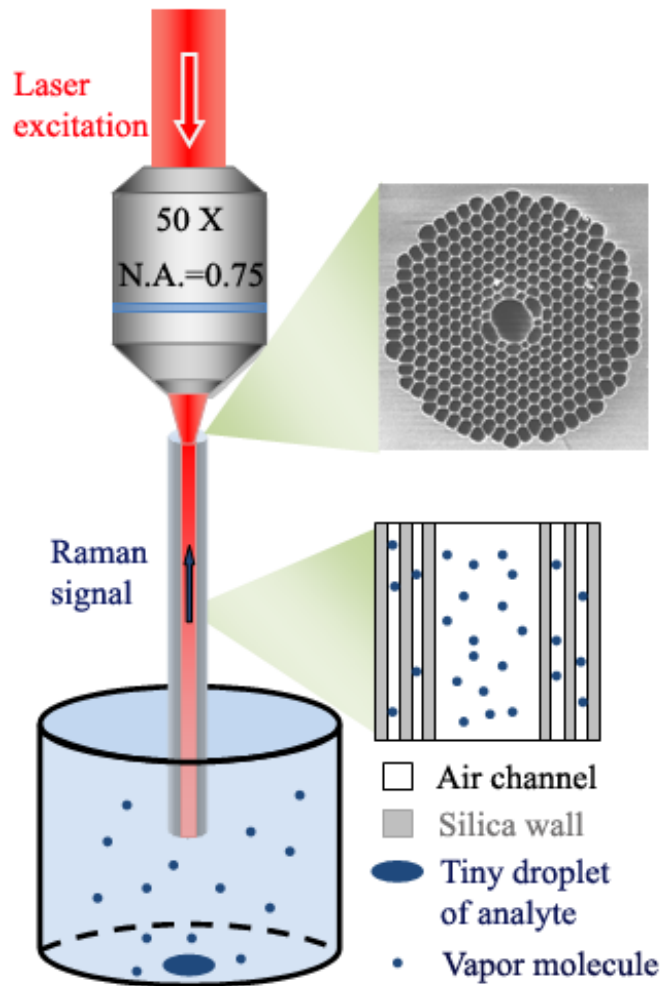


Figure 3.1: Schematic of a HCPCF probe for gas/vapor Raman detection. Top right: Cross Sectional view of the HCPCF probe; Bottom right: the air channels of the HCPCF filled with gas/vapor molecules. Adapted with permission from ref. 48.

Copyright 2012 Elsevier.

A segment of HCPCF probe was cut carefully at both ends with the fixed length. One end of the fiber was placed under the microscope for coupling while the distal end was placed in the ambient environment (nitrogen, oxygen, and carbon dioxide) or within a 1.2 liter sealed container (toluene, acetone, and 1,1,1-trichloroethane vapors) for remote detection, as shown in Figure 3.1 [48]. For the vapor Raman sensing, a controlled amount of the liquid sample was put inside the container to achieve the specific concentration. The Raman signal was obtained using a Renishaw Invia Raman system with a 785 nm excitation light (laser power: ~30 mW). As a reference, in the conventional bulk Raman detection, the laser light was directly focused in the air without using any fibers. All the spectra presented in this study were baseline corrected.

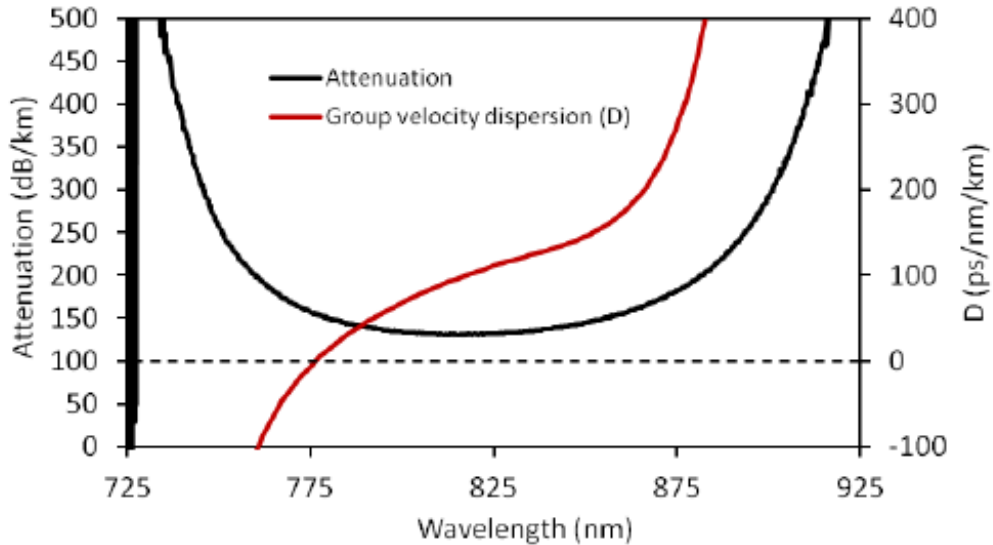


Figure 3.2: Typical attenuation and dispersion of the HCPCF (Model: HC-800B) used in gas Raman detection [67].

### 3.1.2 Ambient gas sensing

Figure 3.3(a) shows the Raman spectra of ambient nitrogen ( $2331\text{ cm}^{-1}$ ) and oxygen ( $1556\text{ cm}^{-1}$ ) obtained by both the conventional bulk detection and the 30 cm-long HCPCF probe. Choosing the nitrogen Raman line as a reference, the HCPCF probe can produce a signal intensity of 11000 (counts) with an integration time of 10 s, while the bulk detection only achieves an intensity of 95 (counts) with an integration time of 60 s. This comparison leads to a sensitivity enhancement of  $\sim 700$  times for the 30 cm-long HCPCF probe. We also quantitatively characterized the length dependence of the gas Raman signals using the HCPCF probe. Figure 3.3(b) shows the Raman spectra of ambient air detected with a series of fiber lengths and Figure 3.3(c) shows the length dependence of the nitrogen Raman signal. It can be concluded that the Raman signal increases almost linearly with respect to the fiber length in the range of 5-30 cm. Longer fiber length will lead to even stronger Raman signal. Figure 3.3(d) illustrates that the sensitivity enhancement can be up to  $\sim 4000$  times with the entire 10 meters of HCPCF available in our lab. With the limited amount of HCPCF, the length dependence of Raman sensitivity enhancement has not been studied beyond 30 cm. For our following experiments we chose 30 cm as the fiber length to achieve the enhancement of Raman signal and to limit both the detrimental fiber background and the filling time for the gas or vapor samples.

With the much enhanced Raman signal, we demonstrate that the ambient carbon dioxide ( $\sim 0.04\%$ ) Raman shifts can be detected by using the HCPCF probe with an integration time of 3 min, as shown in Figure 3.4. The peak at  $1388\text{ cm}^{-1}$  is one of the

Fermi doublet of the Q-band of carbon dioxide [68]. It is also noticed that the other much weaker rotation-vibration Raman bands of oxygen besides from the strongest  $1556\text{ cm}^{-1}$  peak can be detected with the HCPCF probe ( $1433\text{ cm}^{-1}$ ,  $1445\text{ cm}^{-1}$ ,  $1457\text{ cm}^{-1}$ ,  $1470\text{ cm}^{-1}$ ,  $1482\text{ cm}^{-1}$ ,  $1494\text{ cm}^{-1}$ ,  $1506\text{ cm}^{-1}$ ,  $1518\text{ cm}^{-1}$ ,  $1530\text{ cm}^{-1}$ ,  $1581\text{ cm}^{-1}$ ,  $1592\text{ cm}^{-1}$ ,  $1603\text{ cm}^{-1}$ ,  $1614\text{ cm}^{-1}$ ,  $1625\text{ cm}^{-1}$ ,  $1635\text{ cm}^{-1}$ ,  $1646\text{ cm}^{-1}$ ,  $1656\text{ cm}^{-1}$ ,  $1666\text{ cm}^{-1}$ ,  $1676\text{ cm}^{-1}$ ) [69], which further demonstrate the high sensitivity of this technique.

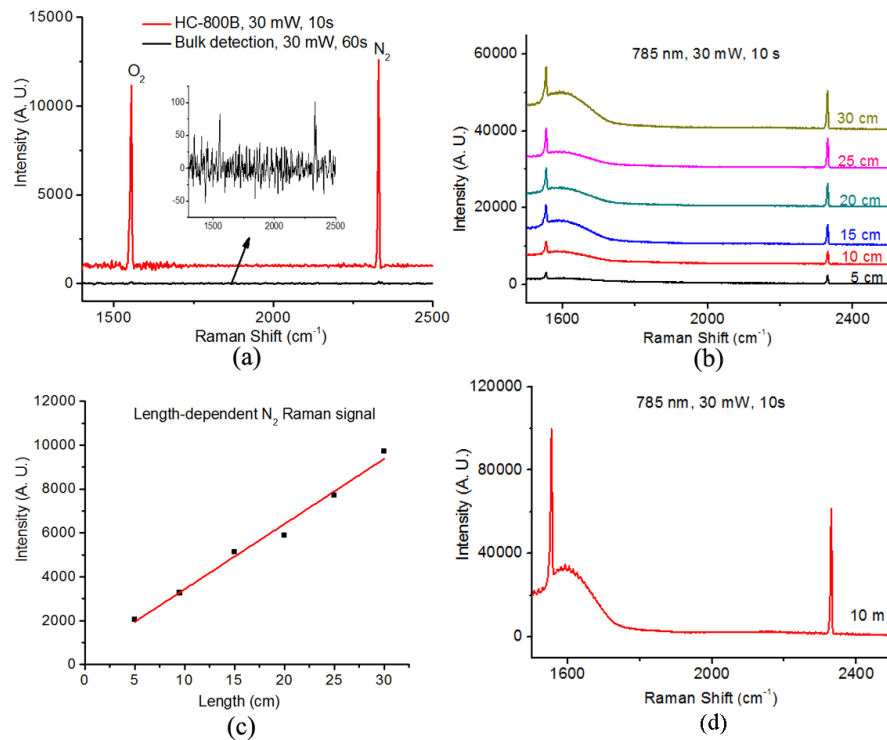


Figure 3.3: (a) Comparison of the ambient  $\text{N}_2/\text{O}_2$  Raman signals collected by the 30 cm-long HCPCF probe (10 s) and the conventional bulk detection (60 s); (b) Ambient  $\text{N}_2/\text{O}_2$  Raman signals obtained by the HCPCF probe at various fiber lengths in the range of 5-30 cm; (c) Length-dependence of the  $\text{N}_2$  Raman signal detected by the HCPCF probe; (d) Ambient  $\text{N}_2/\text{O}_2$  Raman signals obtained by the 10 meter-long HCPCF probe. Adapted with permission from ref. 48. Copyright 2012 Elsevier.

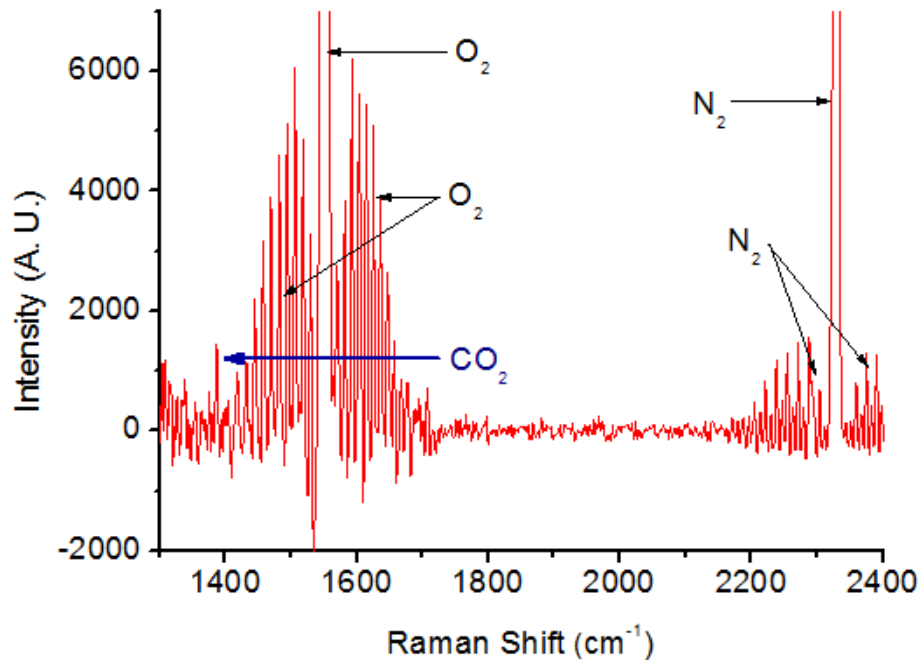


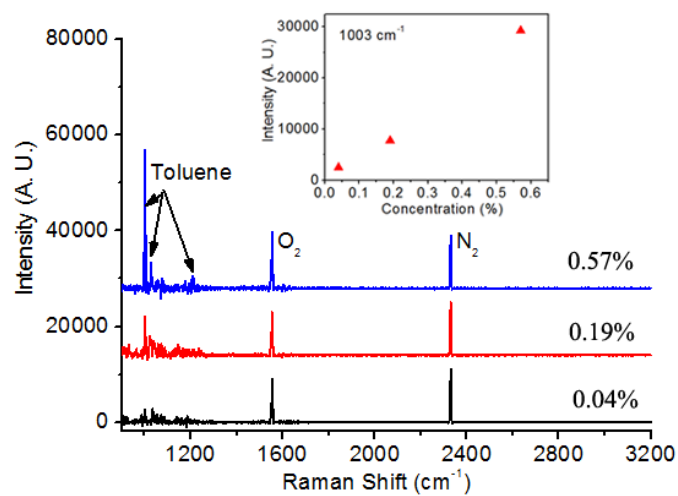
Figure 3.4: Ambient CO<sub>2</sub> Raman detection by the HCPCF probe. (Integration time: 3 min). Adapted with permission from ref. 48. Copyright 2012 Elsevier.

### 3.1.3 Organic vapor sensing

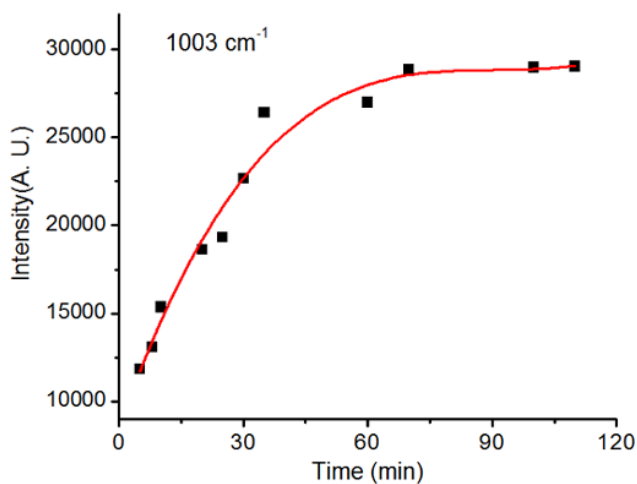
Besides the ambient gases, important organic solvent vapors were tested using the HCPCF probe under various concentrations. Figure 3.5(a) shows the toluene vapor Raman signals obtained by the HCPCF probe at the concentrations of 0.57%, 0.19%, and 0.04%. It can be seen that the two peaks at 1003 cm<sup>-1</sup> and 1031 cm<sup>-1</sup> are still observable at the lowest concentration of 0.04%. The inset of Figure 3.5(a) illustrates the plot of the intensity of 1003 cm<sup>-1</sup> peak vs. the toluene concentration and it demonstrates that the Raman signal has a linear relationship with respect to the concentration, which is crucial for the quantitative measurement. In addition, Figure

3.5(b) shows a time-dependent Raman intensity ( $1003\text{ cm}^{-1}$ ) of the toluene vapor at the concentration of 0.57% and it can be seen that typically around 1 hour is required for the filling of vapor/gas inside the small fiber channels to get the stable Raman signal.

Similarly, Figure 3.6 presents the acetone vapor Raman detection by the HCPCF probe at concentrations of 0.55%, 0.05%, and 0.01%. The detection limit for acetone ( $2935\text{ cm}^{-1}$ , vibrations of the methyl groups) is 0.01% and the Raman intensity also increases linearly with higher concentrations, as shown in the inset of Figure 3.6. Figure 3.7 shows the Raman spectrum of 1,1,1-trichloroethane vapor at the concentration of 1.2% and the characteristic peak at  $2950\text{ cm}^{-1}$  (symmetric CH stretching mode) is observed for 1,1,1-trichloroethane. Due to the sample restriction, we did not perform a concentration-dependent study for the 1,1,1-trichloroethane vapor; however, we would anticipate that there should also be a linear relationship between the Raman intensity and the concentration for the 1,1,1-trichloroethane vapor.



(a)



(b)

Figure 3.5: (a) Raman spectra of toluene vapor collected by the HCPCF probe at various concentrations (Integration time: 10 s): 0.57%, 0.19%, 0.04%; inset shows linear relationship between Raman signal for the strongest peak and concentration. (b) Intensity of the strongest peak of toluene vapor with respect to the filling time at the concentration of 0.57%. Adapted with permission from ref. 48. Copyright 2012

Elsevier.

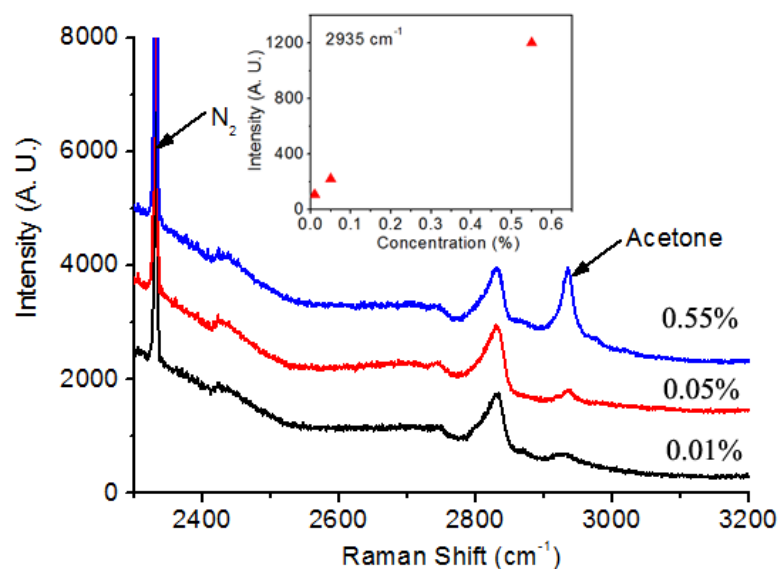


Figure 3.6: Raman spectra of acetone vapor collected by the HCPCF probe at various concentrations (Integration time: 10 s): 0.55%, 0.05%, 0.01%; inset shows linear relationship between Raman signal for the strongest peak and concentration. Adapted with permission from ref. 48. Copyright 2012 Elsevier.

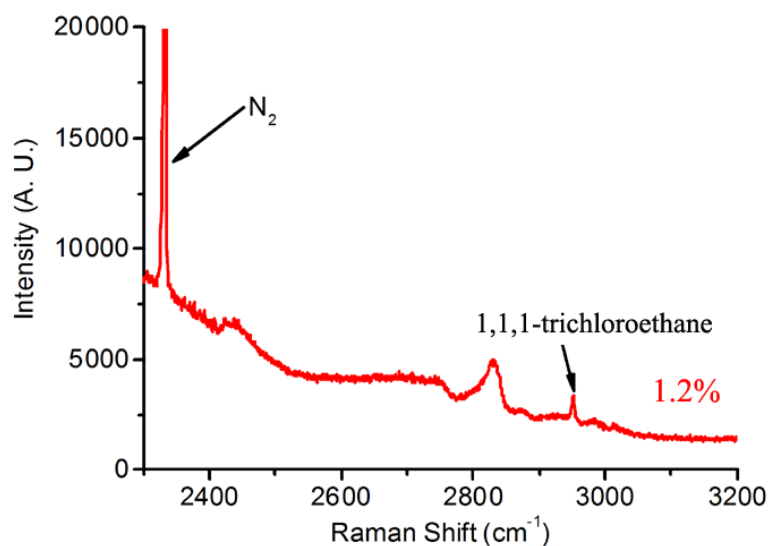


Figure 3.7: Raman spectrum of 1,1,1-trichloroethane vapor collected by the HCPCF probe at the concentration of 1.2%. (Integration time: 60 s). Adapted with permission from ref. 48. Copyright 2012 Elsevier.

While the HCPCF probe works well for individual vapors, it is critical to demonstrate this technique's multiplexing capability quantitatively, especially considering the unique advantage of molecular specificity of RS compared to other sensing techniques. Figure 3.8 shows the Raman spectrum of a vapor mixture of toluene, acetone, and 1,1,1-trichloroethane at the concentrations of 0.57%, 0.55%, 1.2%, respectively. Table 3.1 summarizes the relative Raman intensities of the three target analytes in both the individual vapors and the mixture vapor, using the intensity of nitrogen Raman peak ( $2331\text{ cm}^{-1}$ ) as a calibration to minimize the system variations during the measurements. It can be seen that the intensities of all the three vapors in the mixture are still roughly the same as or just a little bit lower than those measured individually, which quantitatively demonstrates the HCPCF Raman probe as a highly sensitive technique for multiplexed gas sensing applications.

In conclusion, we have demonstrated that HCPCF is a powerful platform for highly sensitive gas detection using RS. With a 30 cm-long HCPCF, a sensitivity enhancement of  $\sim 700$  times can be obtained compared to the conventional bulk detection. The carbon dioxide ( $\sim 0.04\%$ ) has been detected in the ambient environment and the minimum instrumentation-limited detectable concentrations for toluene, acetone, 1,1,1-trichloroethane vapors are 0.04%, 0.01%, 1.2%, respectively. Moreover, we have quantitatively demonstrated its multiplexed gas sensing capability with a three-analyte mixture. Both the high sensitivity and multiplexed sensing

capability provided by the HCPCF Raman probe prove it promising for standoff gas sensing in complex environment.

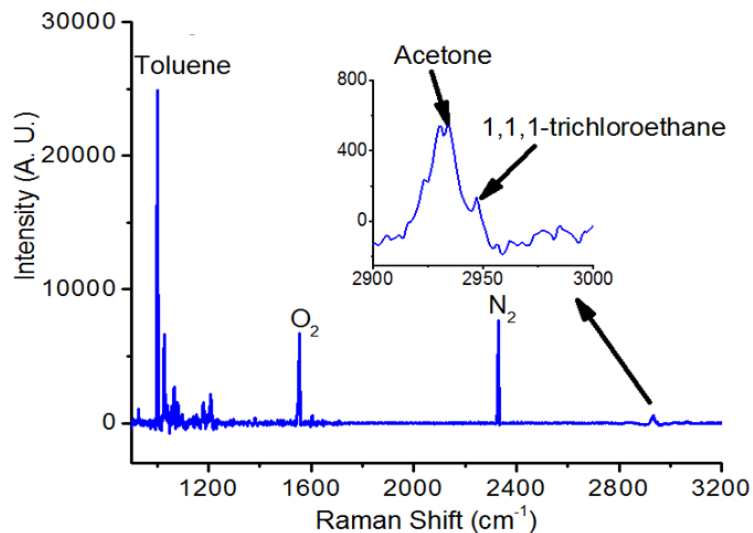


Figure 3.8: Raman spectrum of the toluene/acetone/1,1,1-trichloroethane vapor mixture (0.57%, 0.55%, 1.2%) collected by the HCPCF probe. (Integration time: 10 s); inset shows the close overlap but clear separation of the two fundamental peaks of acetone and 1,1,1-trichloroethane, respectively. Adapted with permission from ref. 48.

Copyright 2012 Elsevier.

Table 3.1. Using the nitrogen Raman line as the calibration, the relative Raman intensities of the vapors collected separately and in mixture by using the HCPCF probe. Adapted with permission from ref. 48. Copyright 2012 Elsevier.

	Toluene (1003 cm <sup>-1</sup> )	Acetone (2935 cm <sup>-1</sup> )	1,1,1-trichloroethane (2950 cm <sup>-1</sup> )
0.57% toluene	2.64	N.A.	N.A.
0.55% acetone	N.A.	0.10	N.A.
1.2% 1,1,1-trichloroethane	N.A.	N.A.	0.032
Mixture	2.29	0.068	0.025

## **3.2 Glucose Raman detection**

While it is straightforward to employ the HCPCF for the gas detection, it is also possible to apply this technique for the liquid samples for the purpose of the sensitivity improvement. One example is the glucose Raman detection.

### **3.2.1 Background knowledge of glucose detection**

Currently diabetes mellitus (type I and II) is an epidemic sweeping the world, affecting more than 171 million people worldwide (2.8% of the population) and costing the U.S. over \$132 billion each year [70]. It is estimated that the number of patients will increase rapidly to 366 million by 2030 [71]. Although there is no known cure for diabetes, diabetics manage their blood sugar levels in various ways to maintain their health, such as daily monitoring, diet, exercise, and use of medications (insulin in the case of type I, oral medications as well as potential insulin usage in type II). When the human body fails to produce insulin, the metabolic disorder will affect the blood glucose concentration to fall outside the normal range of 4.4–6.6 mM. Therefore, frequent measurements of blood glucose levels are needed for the diagnosis and management of diabetes mellitus. Actually, glucose biosensor occupies 85% of the entire biosensor market due to the huge population of diabetics. Conventional glucose monitoring technique involves “finger pricks” which monitors the hydrogen peroxide evolution from the oxidation of glucose with glucose oxidase; however, it is an indirect electrochemical detection and inconvenient for sampling

[71]. Thus, the development of a glucose detection system that is molecule-specific, sensitive, reliable, convenient and affordable has attracted extensive attention recently.

Among the biosensing techniques, optical biosensors are attractive since they are usually sensitive, often non-invasive, in some cases molecule specific, and relatively low cost. Previously, several optical methods have been applied to detect glucose [72]. One technique, using mid-infrared absorption, shows sensitivity to temperature, pH, and exhibits interference from water absorption [73]. Laser polarimetry is another protocol of glucose detection where polarized light is passed through the aqueous humor of the eye where the polarization is rotated by molecules such as glucose [74]. However, this protocol has drawbacks such as rotation of the polarization by molecules other than glucose. In addition, detection methods have been employed to monitor fluorescence changes of dye molecules containing arylboronic acids upon binding to glucose [75, 76]. However, molecules with similar structures or properties to glucose, e.g. other sugars such as fructose, can negatively affect the detection of glucose itself.

For the advantage of molecular specificity in complex blood samples, RS has been used for the glucose detection. However, Raman detection of glucose at physiological concentrations usually needs both high laser power (~250 mW) and long integration time (~5 min) [77]. This level of laser exposure is significantly high for the human body and therefore not practical for clinical tests. One promising method to overcome these problems is to use the SERS technique. Van Duyne et al. have done extensive

work on the SERS detection of glucose [78, 79]. In their study, SERS has been successfully implemented to detect glucose at physiological concentrations using thiols to anchor glucose to a silver film-over-nanospheres substrate [78, 79]. In another study, Dinish et al. used a nanogap SERS substrate with a deep-UV lithography technique for glucose sensing [80]. However, it is difficult to achieve high reproducibility, good uniformity, and long term stability for these SERS substrates. Moreover, glucose SERS sensing requires long incubation time (typically 10 min) for the molecules to get close to the metal surface, which inherently adds to the total measurement time.

In order to overcome the aforementioned issue, we implemented a liquid-filled PCF probe for the glucose detection based on normal RS [47].

### **3.2.2 Liquid-filled PCF preparation and Raman measurement**

D-Glucose and D-Fructose were purchased from Fisher Scientific and Sigma Aldrich respectively. Milli-Q water was used throughout this study [47].

In this work, we used an 8 cm-long HCPCF segment (Crystal Fiber A/S, model AIR-6-800) with its cross-section shown in Figure 3.9. The central core diameter of the PCF was 6  $\mu\text{m}$ , the side length of the hexagon-shaped cladding channels was 0.75  $\mu\text{m}$ , and the pitch distance between the cladding channels was 1.6  $\mu\text{m}$ . The fiber was dipped into the sample solution for the liquid to fill the air channels of the PCF probe by the capillary force. Then the dipped end was placed under the microscope for measurements. The Raman signals were collected using a Renishaw RM2000 Raman

System with a 50× objective lens in a backscattering geometry. Figure 3.9 shows a schematic of the liquid-filled PCF probe operating in the aqueous glucose detections, which is very similar to that in the gas Raman detection. The excitation laser wavelength was 632.8 nm. The laser power was around 2 mW and the integration time was 30 s. All the Raman spectra presented in this study were baseline-corrected.

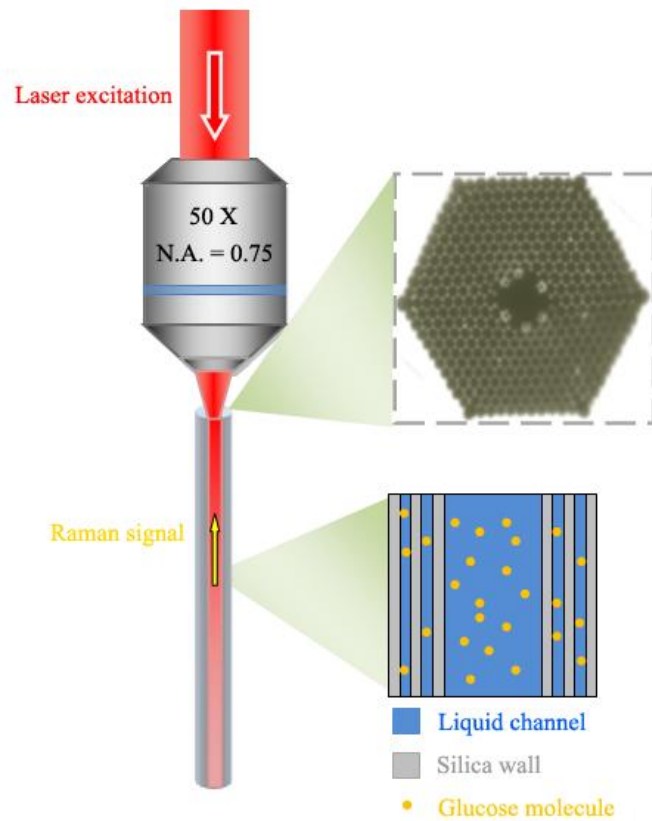


Figure 3.9: Schematic of a liquid-filled PCF probe for glucose detection. Top right: Cross Sectional view of the PCF probe (provided by Crystal Fiber A/S); Bottom right: the air channels of the PCF filled with glucose solution. Adapted with permission from ref. 47. Copyright 2011 Springer-Verlag.

### 3.2.3 Glucose Raman detection at physiological concentrations

By confining both the laser light and the sample solution along the length of the fiber, a much greater laser-analyte interaction volume can be achieved compared to the bulk detection, in which the effective interaction volume is limited by the spot size of the laser beam in the lateral direction and the depth of focus in the longitudinal direction. Similar to the excitation laser light, the Raman scattered signal will also be confined and (partially) propagated back in the liquid-filled PCF to the Raman spectrometer, which results in a higher collection efficiency than the bulk detection.

It should be noticed that in this study, sealing the cladding channels of the PCF to make a LCPCF, which is widely used in previous reports of PCF SERS detections, is not necessary [29, 51]. This is because there is no concern about the large background introduced by the interaction between the metal nanoparticles and fused silica walls, which exists in SERS experiments, which will be discussed later [52]. Therefore, the preparation of the HCPCF probe is much simplified, similar to that in the gas Raman measurements [48].

Figure 3.10 shows the Raman spectra of glucose solutions collected in bulk detection and using the liquid-filled PCF at different glucose concentrations. The spectra show characteristic Raman peaks of glucose, which is consistent with that in the literature [79]. Choosing the major Raman peak at  $1127\text{ cm}^{-1}$  as a reference, the liquid-filled PCF produces a signal intensity of 3647 (counts) at a concentration of 50 mM, while the bulk detection scheme only achieves an intensity of 525 (counts) at a concentration of 1 M. Thus the sensitivity enhancement for the liquid-filled PCF probe in the glucose detection is calculated to be 139.

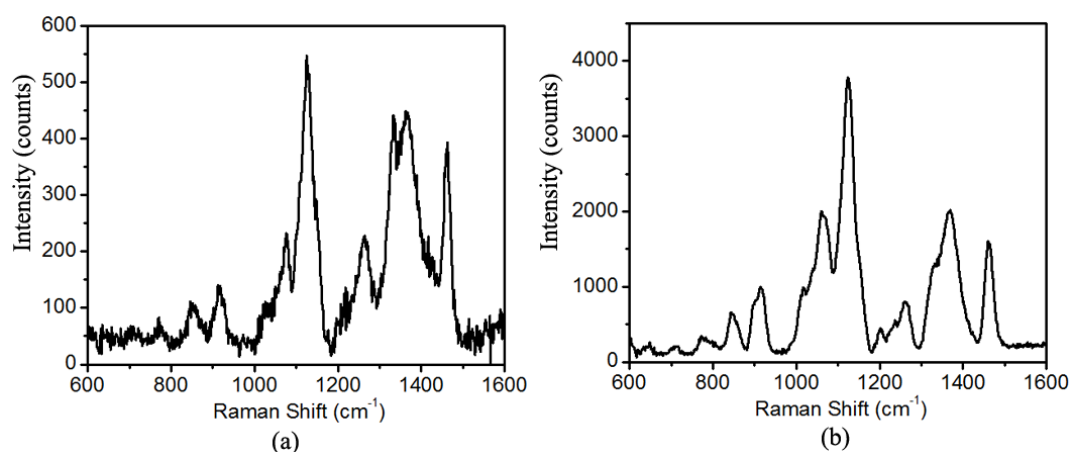


Figure 3.10: Raman spectra of glucose solutions collected by (a) conventional bulk Raman spectroscopy at the glucose concentration of 1 M; and (b) a liquid-filled PCF probe at the glucose concentration of 50 mM. Adapted with permission from ref. 47.

Copyright 2011 Springer-Verlag.

Considering the low signal strength in the bulk detection, which is similar to that in the previous study [77] and caused by the inherently small Raman scattering cross section of glucose, pushing the detection limit of glucose to the physiological concentration range (0–25 mM) is therefore very difficult and usually requires high laser power and long integration time, which is not desirable for practical measurements. Fortunately, the liquid-filled PCF probe shows two orders of magnitude enhanced sensitivity compared to the conventional Raman detection method, and the detection limit can be within the physiological concentration range of glucose.

Figure 3.11 shows a series of Raman measurements of glucose solution were performed at various physiological concentrations, including 1, 5, 10, 15, and 25 mM. It is evident that the major glucose Raman peaks including 1065, 1127, and 1459 cm<sup>-1</sup>

are detectable at concentrations as low as 1 mM [47]. Concentration-dependent Raman intensities of glucose molecules are shown in Figure 3.12 using the strong Raman peak at  $1127\text{ cm}^{-1}$ . A clear linear relationship between the Raman intensity and the concentration can be seen, which is critical for the quantitative measurement of the glucose levels. In addition, the variation of the Raman signal is only 6.0% at a concentration of 15 mM, which is mainly from the fluctuation of the laser power, the system noise, and the slight change in PCF position under the microscope.

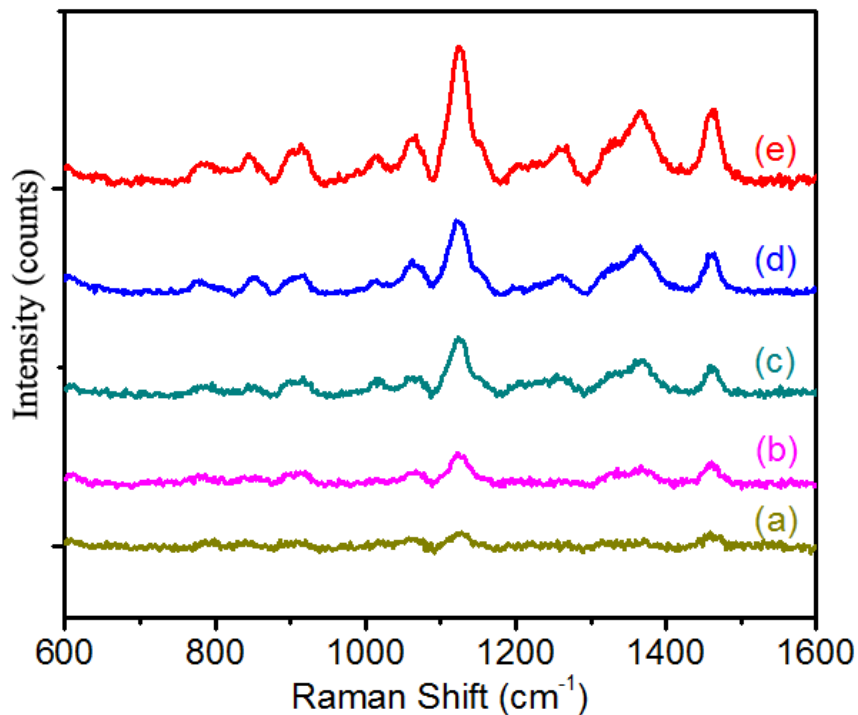


Figure 3.11: Raman spectra of glucose solutions collected by the liquid-filled PCF probe at various concentrations: (a) 1 mM; (b) 5 mM; (c) 10 mM; (d) 15 mM; (e) 25 mM. Adapted with permission from ref. 47. Copyright 2011 Springer-Verlag.

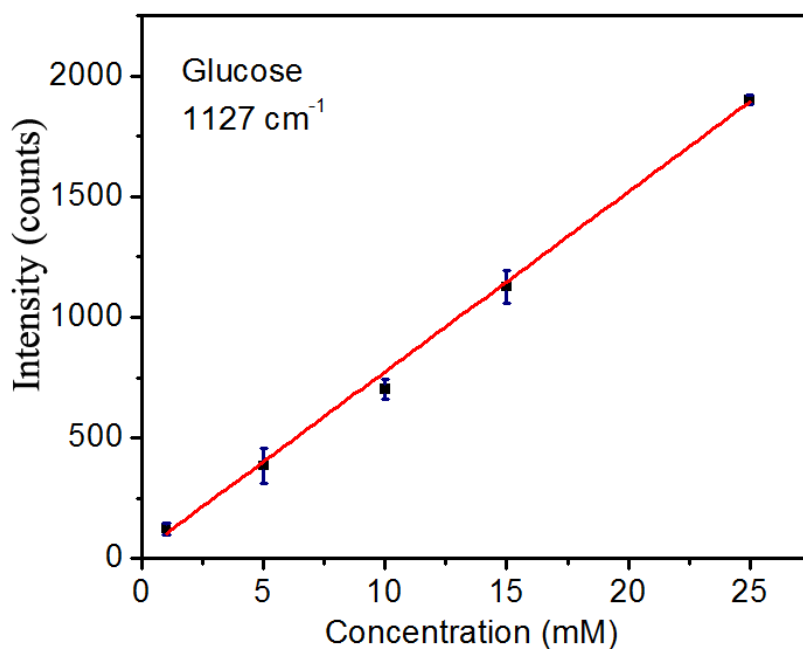


Figure 3.12: Concentration-dependent Raman intensities of glucose ( $1127\text{ cm}^{-1}$ ) measured by the liquid-filled PCF probe. Each datum indicates 5 measurements for each sample, and each error bar indicates the standard deviation. Adapted with permission from ref. 47. Copyright 2011 Springer-Verlag.

The above results demonstrate glucose detection at the physiological concentrations by RS, using the lowest laser power (2 mW) and the shortest integration time (30 s). This level of performance is comparable to and even lower than that reported in the SERS protocols [78-80]. Moreover, the PCF detection method has the following advantages: 1) The PCF detection is highly reproducible without uniformity and substrate instability issues (common problems in SERS techniques), making the quantitative measurement of glucose concentration feasible. 2) The PCF probe preparation and measurement is simpler than SERS detection, which consists of complicated and time-consuming steps such as SERS substrate

fabrication and analyte adsorption. 3) The maximum sampling volume is estimated to be less than 50 nL, considering the total volume of all air channels in the PCF. 4) Similar to other fiber sensors, the PCF probe possesses the unique advantages of flexibility and potential in-situ remote sensing capability.

To demonstrate the unique molecular specificity of RS using the liquid-filled PCF probe, we chose fructose as the competing sugar in the solution. Figure 3.13 shows the Raman spectra of glucose (10 mM), fructose (10 mM), and a mixture of glucose (5 mM) and fructose (5 mM), respectively. The Raman spectra of glucose and fructose can be easily distinguished and are consistent with that in the previous reports. The Raman signal of the mixture is nearly half of the sum of the individual Raman signals of these two molecules at 10 mM, as the concentrations have been reduced by a factor of 2. This study shows that the liquid-filled PCF probe can not only quantitatively detect glucose at physiological concentrations, but also fingerprint glucose and differentiate it from fructose.

As a summary for this part [47], we have demonstrated that HCPCF is a powerful tool for quantitative glucose detection at physiologically relevant concentration range using RS. Due to the high sensitivity and compactness of the liquid-filled PCF probe, measurements can be performed under low laser power (2 mW), short integration time (30 s), and small sampling volume (50 nL). The molecular specificity of this technique allows glucose detection in a mixture solution of glucose-fructose. Further improvement in the detection limit can be realized by optimizing the design of HCPCF probe to minimize the absorption and the propagation loss.

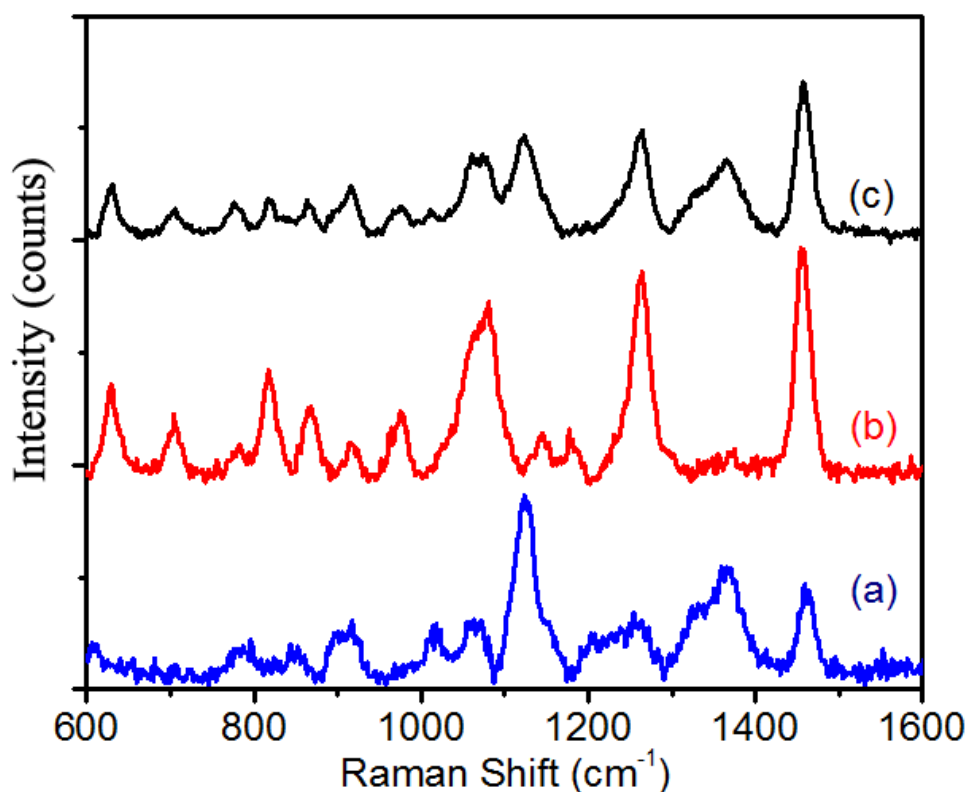


Figure 3.13: Raman spectra of (a) glucose (10 mM), (b) fructose (10 mM), and (c) a mixture of glucose (5 mM) and fructose (5 mM) measured by the liquid-filled PCF probe. Adapted with permission from ref. 47. Copyright 2011 Springer-Verlag.

### 3.3 HCPCF SERS detection and characterization

Besides from RS, the HCPCF probe can also work well with the SERS detections. As mentioned earlier in Section 1.3, previously Shi et al. achieved a sensitivity enhancement of  $100\times$  from the sealed end of the LCPCF in SERS detection and a sensitivity enhancement of  $10\times$  from the unsealed end of the probe, comparing to the bulk detection [29]. However, a systematic and quantitative analysis of the underlying

mechanism has not been given and efforts have not been put in pushing the detection limit of the analytes.

In this Section, we experimentally demonstrate and theoretically analyze two approaches of using the HCPCF as SERS probes [52]. The first approach fills the mixed nanoparticles/analyte solution in all the air channels of a HCPCF; and the second approach fills only the central hollow core channel. Both the liquid-filled PCF probe and the LCPCF probe are simulated using the MIT MEEP code. The simulation results explain the experimental results, and provide guidelines for the design of HCPCF SERS probes for future applications. We also demonstrate the SERS detection of R6G solution at the concentration of 0.1 nM using the LCPCF probe, which is, to the best of our knowledge, the lowest detection limit using similar techniques.

### **3.3.1 Experimental demonstrations of HCPCF SERS detections**

The HCPCF used in this experiment was purchased from Crystal fiber A/S (model AIR-6-800), same as that in the glucose Raman detection in Section 3.2. The citrate-reduced SNPs used in the sample solution were synthesized using the Lee and Meisel method, same as that in the TCMMF SERS detection in Section 2.1. The concentration of SNPs using the Lee and Meisel protocol is estimated to be  $\sim 3.77 \times 10^{-11}$  M.

The sample solution used in this study was prepared as previously reported for various concentrations of R6G molecules ( $10^{-5}$  M –  $10^{-10}$  M), and sodium chloride

(NaCl, 10 mM) was added to induce aggregation of SNPs [28]. Starting with aqueous R6G solution ( $10^{-4}$  M), SNPs were added to dilute the R6G solutions. 30  $\mu$ L of the R6G solution and 270  $\mu$ L of the SNP colloid were mixed to obtain 300  $\mu$ L solutions of  $10^{-5}$  M R6G molecules. Then, 30  $\mu$ L of the resulting solution was added to a 270  $\mu$ L of the SNP colloid again to generate a sample solution with R6G concentration of  $10^{-6}$  M. Solutions of various concentrations from  $10^{-7}$  M –  $10^{-10}$  M, respectively, were prepared using the same method accordingly. The solutions were incubated for about 10 min at room temperature and activated with 15  $\mu$ L NaCl solution for each sample solution. Raman measurements were taken about 20 min after the introduction of salt.

For the liquid-filled PCF SERS probes, one end of the HCPCF was cleaved carefully using a fiber cleaver to produce a flat surface and the other end was cut using a razor blade which does not affect the SERS performance of probe; for a fiber segment that is long enough to fit into the fiber cleaver, both ends can be cleaved. The cleaved end of the HCPCF piece was dipped into the mixed sample solution to allow the liquid to completely fill in both the core and cladding channels due to the capillary effect. Then the flat end was placed under the microscope of the Raman system for the measurements. The total length of the liquid-filled PCF segments used in this experiment varied from 2 mm to 5 cm. The SERS signal was collected using a Renishaw InVia Raman Microscope system and the excitation laser wavelength was 632.8 nm. A 50 $\times$  objective lens was used to couple the excitation laser light onto the liquid sample or into the core of HCPCF and collect the SERS signal as well.

Figure 3.14 shows the SERS spectrum collected using a 2 mm liquid-filled PCF, compared with that obtained by directly focusing the excitation light into the same mixed solution without using any fiber probes. The R6G concentration used in this experiment was  $10^{-6}$  M. The intensity of the SERS peak at  $1509\text{ cm}^{-1}$  was 15000 (A.U.) for the liquid-filled PCF probe and 1385 (A.U.) for the bulk detection. Noticing that the excitation power in the liquid-filled PCF detection is one  $10^{\text{th}}$  of that in the bulk detection, the result shows that the liquid-filled PCF has a 100 times sensitivity enhancement when it is as short as 2 mm.

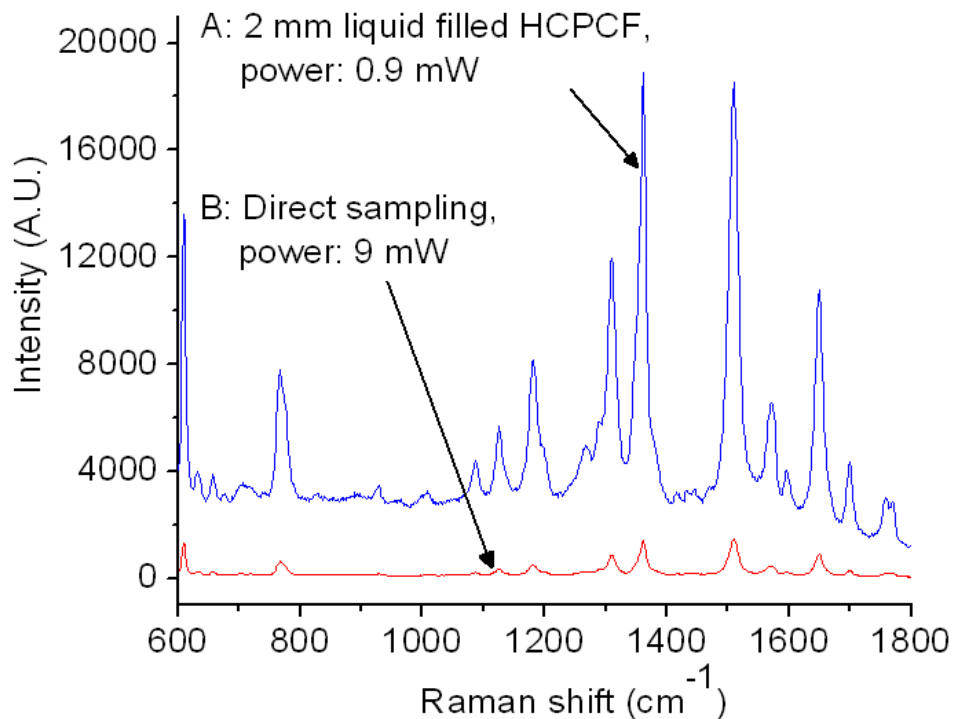


Figure 3.14: Comparison of SERS spectra of R6G at the concentration of  $10^{-6}$  M between the bulk detection and using a 2 mm liquid-filled PCF. Adapted with permission from ref. 52. Copyright 2010 Optical Society of America.

Another experiment was performed to find the sensitivity enhancement utilizing the liquid-filled PCF in both conventional Raman and SERS experiments. For the conventional Raman experiment, the concentration of the R6G solution ( $C_{\text{Raman}}$ ) was  $4.18 \times 10^{-2}$  M. For the SERS experiment, the concentration of the R6G solution ( $C_{\text{SERS}}$ ) was  $10^{-6}$  M. Table 3.2 lists the intensity of the Raman peak at  $1509 \text{ cm}^{-1}$  measured in both the conventional Raman ( $I_{\text{Raman}}$ ) and the SERS experiments ( $I_{\text{SERS}}$ ), with and without using the liquid-filled PCF, respectively.

Table 3.2. Using the  $1509 \text{ cm}^{-1}$  peak as a reference, the intensity of the conventional Raman signal and the SERS signal in both the bulk detection and the liquid-filled PCF. Adapted with permission from ref. 52. Copyright 2010 Optical Society of America.

	Raman Intensity (A. U.)	SERS Intensity (A.U.)
Bulk detection	3104	3213
Liquid-filled PCF	190105	312946

The results show that the sensitivity enhancement is 61 in the conventional Raman experiment (which is similar to that in the glucose Raman detection in Section 3.2), and 97 in the SERS experiment. This will be quantitatively explained in more details later in Section 3.3.2. Also, the EF:

$$EF = \frac{I_{\text{SERS}} / C_{\text{SERS}}}{I_{\text{Raman}} / C_{\text{Raman}}} \quad (3.1)$$

for the liquid-filled PCF is  $6.88 \times 10^4$ , while it is  $4.33 \times 10^4$  in the bulk detection. This experiment demonstrates that the microstructures inside the liquid-filled PCF does not introduce any significant extra SERS enhancement factor, indicating similar electromagnetic field distribution inside the liquid-filled PCF with and without SNPs, except the difference in absorption coefficients.

The sensitivity enhancement using the liquid-filled PCF probe offers an advantage for such SERS probes in low excitation power detection. In the next experiment, we demonstrate that by using the liquid-filled PCF probe the required excitation power can be reduced to one  $100^{\text{th}}$  of what is required in bulk detection, similar to that in the glucose Raman detection in Section 3.2. As shown in Figure 3.15, when the concentration of R6G was  $10^{-6}$  M, the lowest excitation power for a detectable SERS signal of R6G was around  $300 \mu\text{W}$  in bulk detection. When the excitation power was decreased to  $9 \mu\text{W}$  (the lowest controllable output power from the laser used in our experiment), the liquid-filled PCF probe could still detect the SERS signal and the intensity was even 3 times higher than that in bulk detection. This result demonstrates that the lowest excitation power required for a detectable SERS signal using the HCPCF probe can be one  $100^{\text{th}}$  of that in bulk detection, which is very useful especially when designing a SERS sensor with a relatively low power laser or reducing the laser exposure.

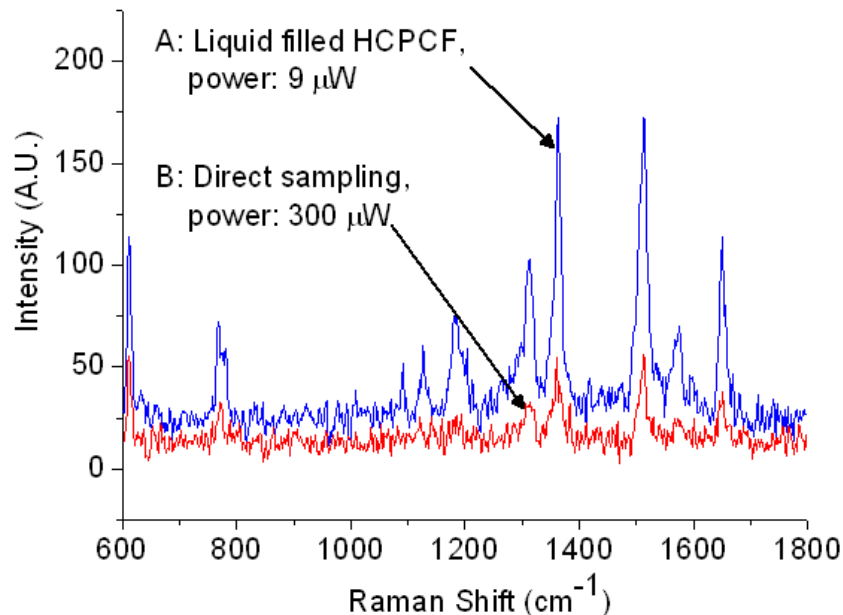


Figure 3.15: Comparison of the SERS signals at lowest excitation powers between bulk detection and using liquid-filled PCF when the concentration of R6G is  $10^{-6}$  M. Adapted with permission from ref. 52. Copyright 2010 Optical Society of America.

While the liquid-filled PCF probe offers a sensitivity enhancement of  $100\times$  at relatively high analyte concentration, at relatively low concentration, e.g.,  $10^{-8}$  M R6G and  $3.77\times 10^{-11}$  M SNPs, this approach fails to detect any SERS signal caused by an enhanced background. As shown in Figure 3.16, the lowest concentration we detected with bulk detection was  $10^{-8}$  M, however, the SERS signal was completely buried in the strong background enhanced by the liquid-filled PCF probe. A detection of the HCPCF segment filled with only the SNP colloid (without R6G) shows a similar background. The enhancement of the background is believed to be that the SNPs tend to attach to the fused silica surface inside the open channels of the HCPCF where the evanescent wave is fairly strong, as will be shown later in Section 3.3.2.

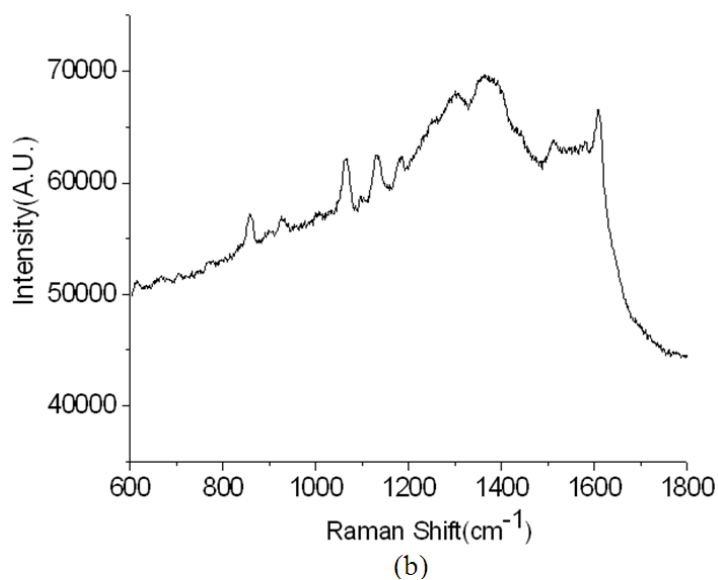
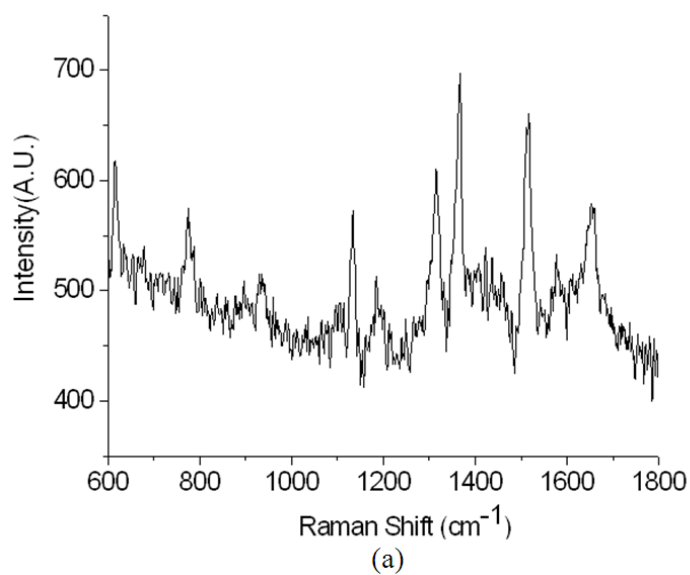


Figure 3.16: SERS signals detected from (a) bulk detection and (b) liquid-filled PCF when the concentration of R6G is  $10^{-8}$  M. While bulk detection can detect R6G signal, liquid-filled PCF failed due to an enhanced SNPs background. Adapted with permission from ref. 52. Copyright 2010 Optical Society of America.

When the ratio between the concentration of R6G and that of SNPs is low, the number of R6G molecules adsorbed on the nanoparticles near the wall regions is not

large enough to lead to a strong signal, therefore, the signal-to-noise (S/N) ratio decreases. To verify our hypothesis, we diluted the SNP solution and thus increased the ratio between the concentration of R6G and that of SNPs. Figure 3.17 illustrates the experimental result after decreasing the concentration of SNPs to  $3.77 \times 10^{-12}$  M, i.e., one  $10^{\text{th}}$  of the original concentration. When the concentration of R6G was  $10^{-7}$  M, bulk detection did not result in any signal due to the smaller concentration of SNPs; however, the liquid-filled PCF probe did detect certain signal although there was still a relatively high background.

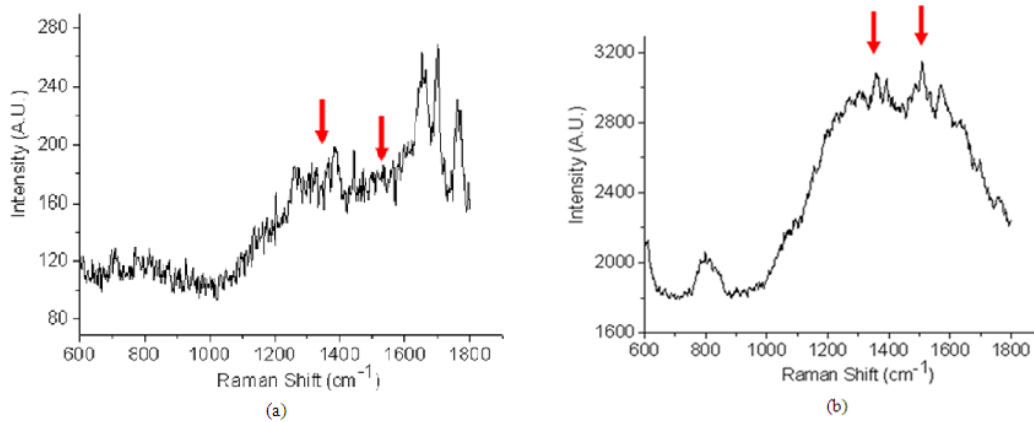


Figure 3.17: When the solution of SNPs is diluted by a factor of 10, the SERS signals are detected from (a) bulk detection and (b) liquid-filled PCF at the concentration of  $10^{-7}$  M. The positions of typical R6G peaks are marked by red arrows. In this case, liquid-filled PCF can detect a lower concentration ( $10^{-7}$  M) than bulk detection. Adapted with permission from ref. 52. Copyright 2010 Optical Society of America.

To reduce the background, we implemented the LCPCF SERS probes [52]. A 5 cm HCPCF segment was prepared by cutting carefully at both ends with a fiber cleaver, and a fusion splicer (model FITELE S175) was used to seal the cladding holes at one

end of the fiber. When the sealed end was dipped into the sample solution only the central core was filled with the liquid. Then the sealed end was placed under the microscope for the measurements.

Figure 3.18 demonstrates the reduction of the background using the LCPCF by showing the background spectra of both the liquid-filled PCF and the LCPCF, where the liquid contains only the silver colloid. The intensity of the background of the liquid-filled PCF is more than 4 times that of the LCPCF. It should be noticed that the arc current used in the fusion splicer needs to be large enough to seal all the cladding channels, especially the ones closest to the central core. The arc current used here (58 mA) was a little larger than what used previously (53 mA) by Shi et al. [29]. For the peaks shown in the background, they can be assigned to citrate used during the synthesis of SNPs [81].

By filling the LCPCF with the mixed solution of R6G and SNPs, the lowest detectable R6G concentration with the  $3.77 \times 10^{-11}$  M silver colloid was  $10^{-10}$  M (0.1 nM), as shown in Figure 3.19. It is also interesting to notice that some of the SERS peaks split into two separate peaks (peaks d and e, g and h) at this low concentration level. One possible reason is that at low concentrations, the R6G molecules are attached to the surface of the LCPCF in an ordered orientation/conformation, which gives narrower Raman peaks and the appearance of the two separate peaks; while at higher concentrations, besides those molecules adsorbed on the wall, there are some in the solution with a more random or inhomogeneous orientation/conformation, which result in inhomogeneously broadened Raman peaks and the appearance of one

broad peak. Besides the R6G SERS peaks marked, other peaks (a and c) in Figure 3.19 can be attributed to citrate introduced during synthesis [81]. The experimental results shown in Figure 3.16 and Figure 3.19 demonstrate that the detection limit using a LCPCF SERS probe is two orders of magnitude lower than that using the bulk detection, which makes the LCPCF SERS probe a practical technique in liquid-phase high-sensitivity chemical detection.

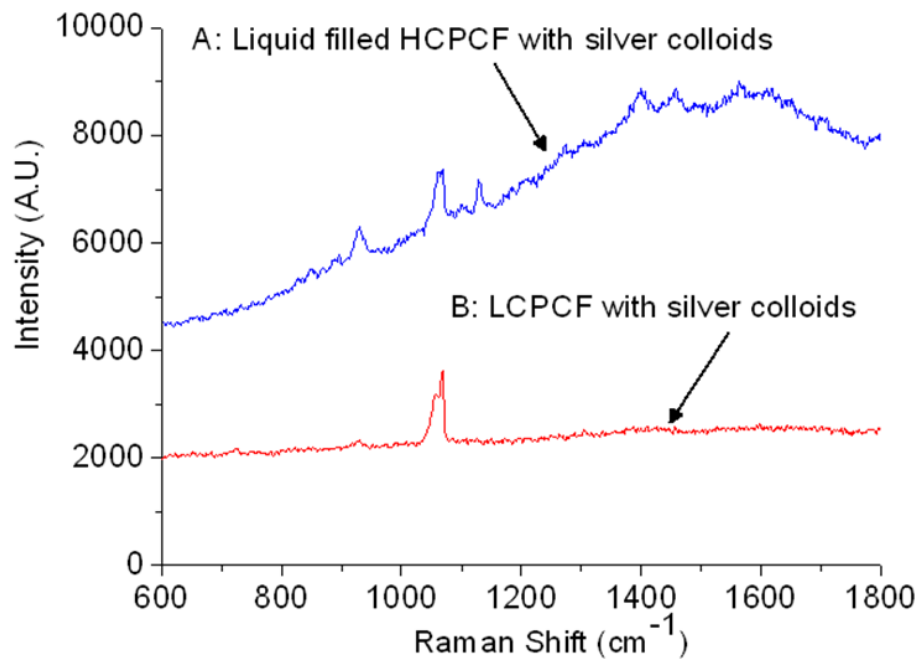


Figure 3.18: Background comparison between a liquid-filled PCF and a LCPCF with only the silver colloid. Adapted with permission from ref. 52. Copyright 2010 Optical Society of America.

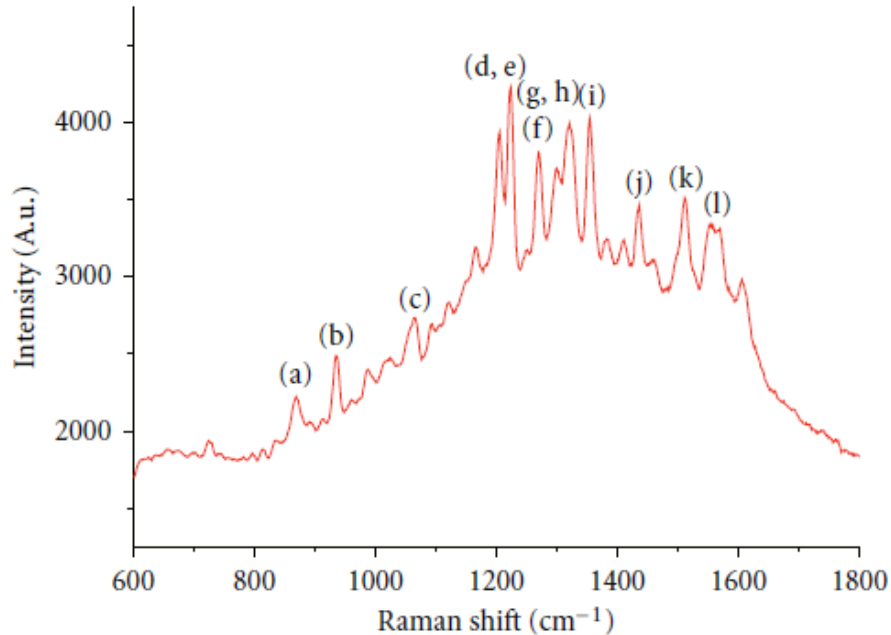


Figure 3.19: SERS signal from the detection of 0.1 nM R6G using a LCPCF. Peaks (a) and (c) are from the citrate introduced during the synthesis of SNPs. Peaks (b), (d), (e), (f), (g), (h), (i), (j), (k) and (l) are typical R6G peaks. Specifically, (d) and (e) are split from the  $1204\text{ cm}^{-1}$  peak while (g) and (h) are split from the  $1312\text{ cm}^{-1}$  peak compared to the high concentration SERS spectrum. Adapted with permission from ref. 52. Copyright 2010 Optical Society of America.

### 3.3.2 Theoretical analysis and discussion

To quantitatively explain the observed experimental results, especially the high sensitivity of HCPCF probes, we theoretically analyze the light distribution inside a HCPCF with the MIT MEEP code [82]. It is found that the liquid inside the air channels of the HCPCF significantly helps the light confinement inside the fiber even when the wavelength of the excitation light (e.g., 633 nm) does not match the designed transmission wavelength range of the HCPCF (745 – 853 nm) [52].

In the simulation, we excited a Gaussian beam with a wavelength of 633 nm and a width of 6  $\mu\text{m}$ , which was incident upon either a bulk liquid or a HCPCF. And the HCPCF had either open air holes, or all the holes filled with the liquid, or only the central core filled with the liquid, corresponding to the various experimental cases. The simulated HCPCF had the following parameters: the core diameter 4.5  $\mu\text{m}$ , the side length of cladding holes 0.75  $\mu\text{m}$ , pitch distance between cladding holes 1.6  $\mu\text{m}$  and three layers of cladding holes were considered.

Figure 3.20 illustrates the light propagation in various cases: focusing a Gaussian beam at (a) the surface of a bulk liquid (water), (b) the entrance of a HCPCF with open air channels, (c) the entrance of a HCPCF with all channels filled with liquid, (d) the entrance of a LCPCF with only the core channels filled with liquid, and (e) the entrance of a LCPCF with a 200 $\mu\text{m}$  air gap between the entrance and the liquid surface. To quantitatively characterize the power loss during the propagation, Figure 3.21 presents the total power within the fiber cross-section in (a) bulk detection, (b) HCPCF with air channels, (c) HCPCF filled with water, (d) LCPCF with a 200  $\mu\text{m}$  air gap between the entrance and the liquid surface. Figure 3.21(a) shows that the effective length ( $1/e$  power distance) for light propagating in bulk water is 166  $\mu\text{m}$ , which is roughly the same as the depth of focus for the Gaussian laser beam. Figure 3.21(b) shows that in an open air channel HCPCF, most power is quickly lost after the light is coupled into the fiber, since the excitation wavelength does not match the design wavelength of the HCPCF, and the propagation distance is around 200  $\mu\text{m}$ .

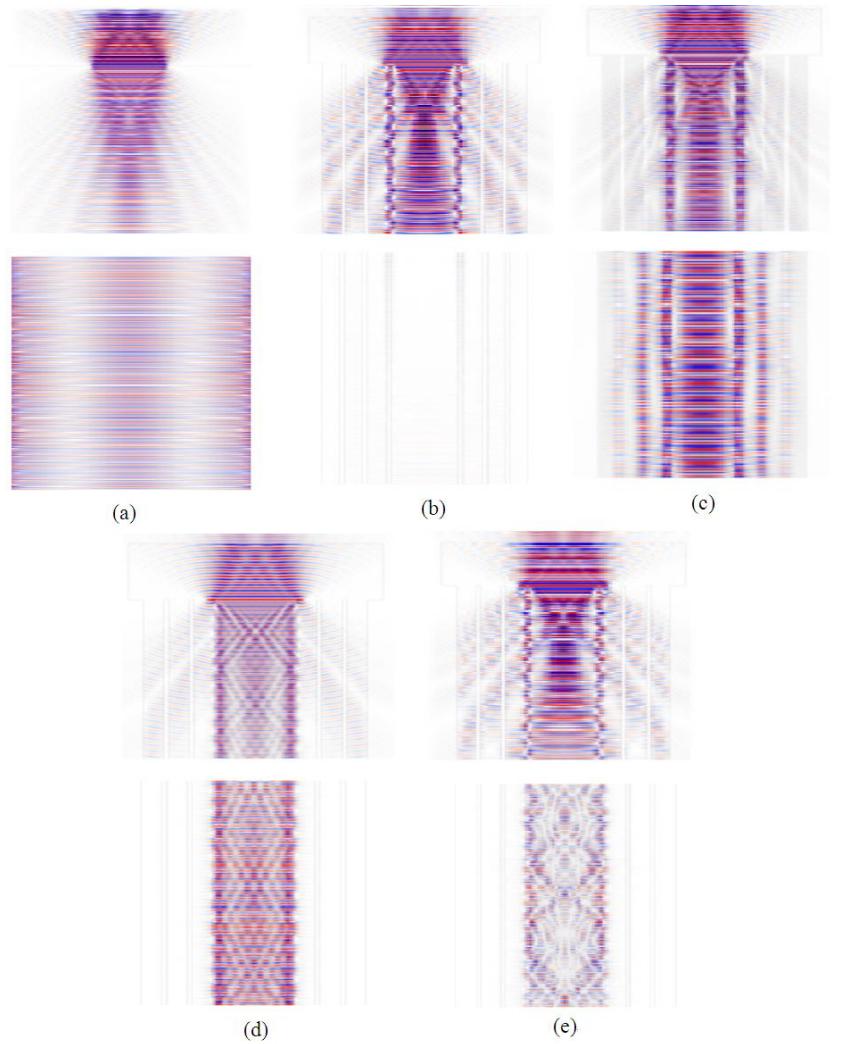


Figure 3.20: Light propagation when focusing a Gaussian beam at (a) the surface of a bulk liquid medium (water), (b) the entrance of a HCPCF with open air channels, (c) the entrance of a HCPCF with all channels filled with liquid, (d) the entrance of a LCPCF with only the core channels filled with liquid, (e) the entrance of a LCPCF with a 200  $\mu\text{m}$  air gap between the entrance and the liquid surface. In each set of images, the top one corresponds to the field distribution near the entrance of either bulk medium or HCPCF, while the bottom one corresponds to the field distribution after a propagation distance of 400  $\mu\text{m}$  from the entrance. Adapted with permission from ref. 52. Copyright 2010 Optical Society of America.

Figure 3.21 (c) represents the liquid-filled PCF and shows that the light will decay very slowly after coupled into the fiber. This demonstrates the liquid significantly broadens the transmission range and provides the desired light confinement inside the fiber. Figure 3.21(d) illustrates that when the light is coupled into a LCPCF with an air gap at the top, there will be significant power loss inside the air gap, and only when it reaches the water region the light can be confined again. Figure 3.21(d) also explains the previous SERS detection from the unsealed end of a LCPCF showing a lower sensitivity enhancement observed by Shi et al. [29], which is due to the existence of a possible air gap between the liquid surface and the fiber entrance.

Figure 3.22 shows the intensity distribution with respect to the radial position in both the liquid-filled PCF and the LCPCF where the cross section is 400  $\mu\text{m}$  below the fiber entrance. Consistent with the result shown in Figure 3.20 (c), Figure 3.22(a) indicates that although most of the light is inside the fiber core, a considerable light energy is propagating inside the glass regions of the cladding holes (shaded areas in Figure 3.22). The strong intensity of the evanescent wave near the walls results in an enhanced SNP background during the liquid-filled PCF experiments. Although the intensity near the wall of the fiber core in the LCPCF probe is still strong, the total effective interaction wall areas is much smaller than that in liquid-filled PCF, which results in a much weaker background.

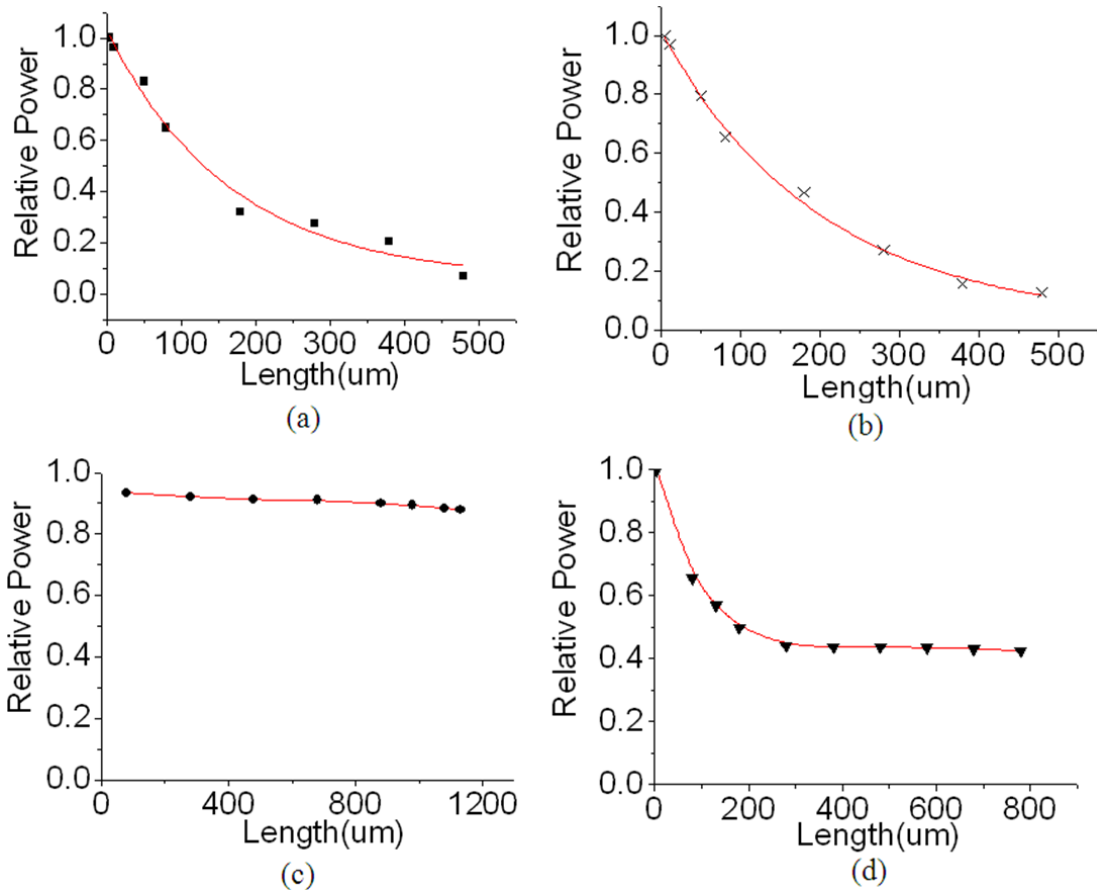


Figure 3.21: Light power inside the fiber cross-section with respect to the propagation distance in various cases: (a) bulk water; (b) HCPCF with open air channels; (c) water-filled PCF; (d) LCPCF with a 200  $\mu\text{m}$  air gap between the fiber entrance and the surface of water. Adapted with permission from ref. 52. Copyright 2010 Optical Society of America.

Based on the simulation shown above, we compare the number of SERS nanoparticles in a liquid-filled PCF probe with that in the bulk detection to explain the mechanism behind the sensitivity enhancement and our experimental results. For a liquid-filled PCF probe, we consider the central core plus the nearest three cladding layers as the SERS-active regions. For the bulk detection, we consider the SERS-

active region inside a cylinder with a Gaussian waist as the cross-section and the depth of focus as the effective length. Using the parameters of HCPCF in Section 3.2.2 and considering the shortest experimental length with a 100 times sensitivity enhancement that is 2 mm, the total number of nanoparticles/molecules in the interaction volume of a liquid-filled PCF is calculated to be 46 times that in the bulk detection, close to the sensitivity enhancement of 61 measured in Section 3.3.1 for the conventional Raman scattering. In addition, since the nanoparticles tend to adhere to the cladding walls where the evanescent wave is stronger, a redistribution of the light energy and nanoparticles results in an extra sensitivity enhancement in SERS experiments. These factors combined together contribute to an overall SERS sensitivity enhancement of 97 as shown in Section 3.3.1.

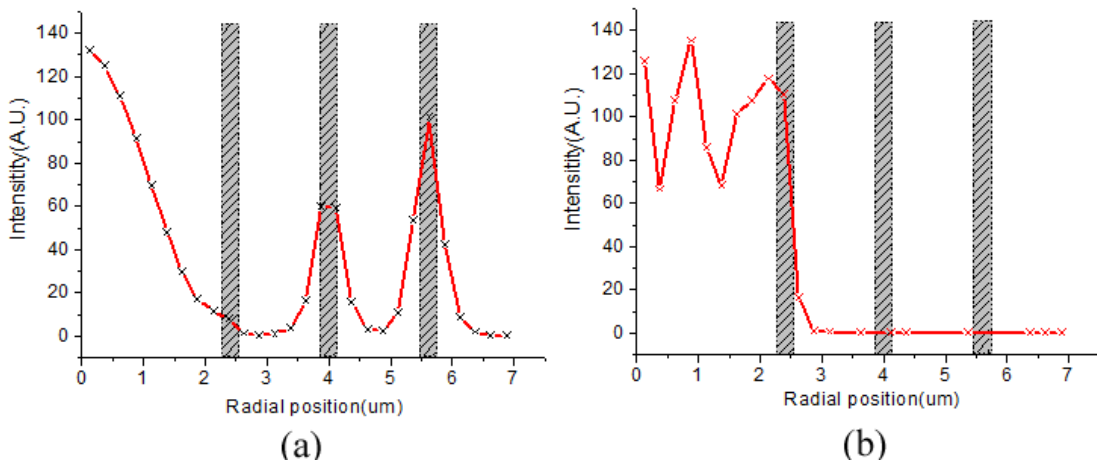


Figure 3.22: Plot of intensity distribution with respect to the radial position of (a) liquid-filled PCF; (b) LCPCF. Gray regions indicate silica walls in the HCPCF. Adapted with permission from ref. 52. Copyright 2010 Optical Society of America.

In addition to the above analysis, we also performed FDTD simulations for the electromagnetic field near nanoparticles inside a HCPCF and no significant field enhancement was observed. The FDTD result further confirms that the sensitivity enhancement is mainly due to the increased number of nanoparticles involved in the SERS activity.

### **3.4 Bacteria SERS detection using LCPCF**

While the LCPCF probe works well with the small dye molecules, it is important to demonstrate its application in the detection of interesting biological macromolecules or systems. In this part, we present the work of employing the LCPCF probe for the SERS detection of the live bacterial cells of *Shewanella oneidensis* MR-1 [31]. The bacteria *Shewanella* is a Gram-negative facultative anaerobe with extracellular electron transfer capability that has various applications such as bioremediation of contaminated and radioactive soils, heavy metal detoxification, and microbial fuel cells [83, 84]. The SERS detection and characterization of this biological system can help us have a better understanding of its properties.

#### **3.4.1 Bacterial strain and culture conditions**

*Shewanella oneidensis* MR-1 strain (ATCC 700550) was obtained from the American Type Culture Collection (ATCC, Manassas, VA). The MR-1 cells were cultured in the lactate-defined minimum medium, which consists of (per liter of deionized water) 20 mM sodium lactate, 28 mM NH<sub>4</sub>Cl, 1.34 mM KCl, 5 mM

NaH<sub>2</sub>PO<sub>4</sub>, 0.7 mM Na<sub>2</sub>SO<sub>4</sub>, 1 mM MgSO<sub>4</sub>•7H<sub>2</sub>O, 20 mM PIPES, 52 mM NaCl, 0.2 mM CaCl<sub>2</sub>, 1 mL vitamin and 1 mL trace metal elements. The cells were grown aerobically at 30 °C in a water bath incubator with vigorous shaking at 150 rpm.

### **3.4.2 Bacteria SERS detection**

For aqueous bacteria of *Shewanella* SERS detection, the bacteria sample solutions were simply mixed with the citrate-reduced SNPs (1:9, v/v). The LCPCF SERS probe was prepared as the same as that in Section 3.3.1. In this experiment, the SERS signals were obtained using a Renishaw Raman RM 2000 System with a 632.8 nm excitation light. The laser power was around 2 mW and the exposure time for each SERS measurement was 10 s. The SERS spectra presented in this study were baseline corrected.

Figure 3.23 shows the SERS spectra of MR-1 cells obtained by the bulk detection and using the LCPCF probe at various concentrations. It can be seen that while the detection limit is 10<sup>9</sup> cells/mL in bulk detection, the detection limit can be as low as 10<sup>6</sup> cells/mL using the LCPCF probe. At the same high concentration of 10<sup>10</sup> cells/mL, the sensitivity enhancement is around 30 times choosing one of the main peaks at 1449 cm<sup>-1</sup> as a reference, which is generally consistent with the result of R6G SERS detection using the LCPCF SERS probe.

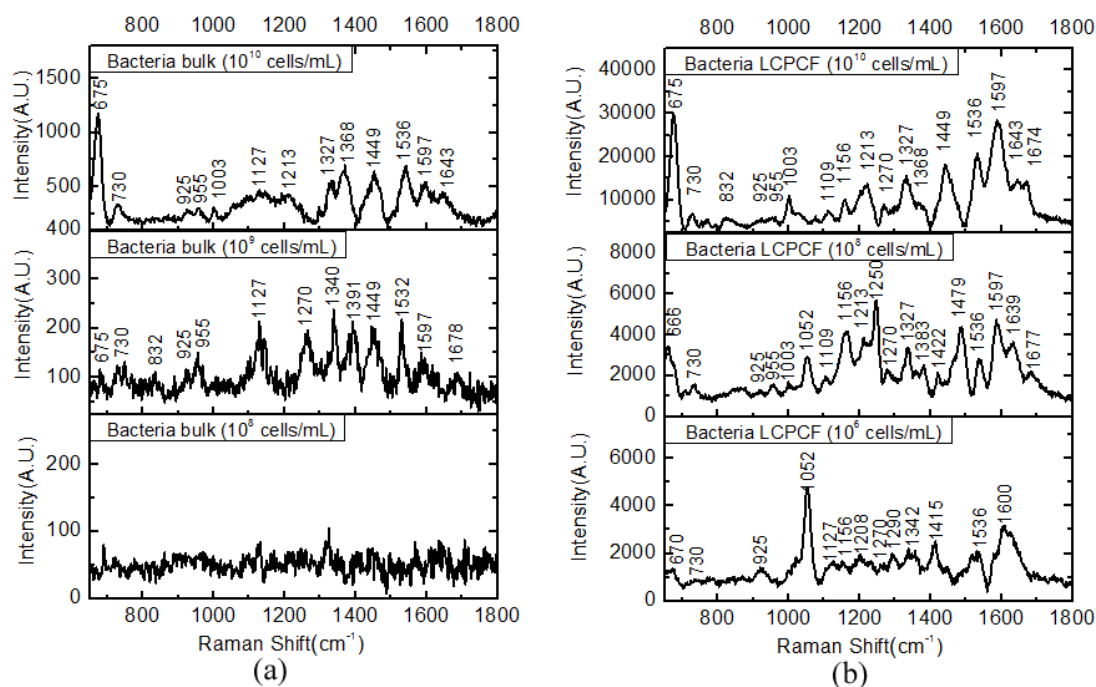


Figure 3.23: SERS spectra of MR-1 cells detected by (a) bulk detection ( $10^{10}$ ,  $10^9$ , and  $10^8$  cells/mL), and (b) using the LCPCF probe ( $10^{10}$ ,  $10^8$ , and  $10^6$  cells/mL). Adapted with permission from ref. 31. Copyright 2011 American Chemical Society.

Table 3.3 lists the tentative band assignments for the SERS spectra of MR-1 cells [58, 85, 86]. Some of the major Raman peaks are from  $\text{CH}_2$  wagging mode ( $1327 \text{ cm}^{-1}$ ) and scissoring mode ( $1368 \text{ cm}^{-1}$ ,  $1449 \text{ cm}^{-1}$ , and  $1479 \text{ cm}^{-1}$ ). Other major Raman peaks can be attributed to the  $\text{COO}^-$  asymmetric stretching mode ( $1536 \text{ cm}^{-1}$ ), bacterial amide ( $1597 \text{ cm}^{-1}$ ), and Amide I ( $1643 \text{ cm}^{-1}$  and  $1674 \text{ cm}^{-1}$ ).

Control SERS measurements of the lactate medium without the bacteria were performed in both the bulk detection and using the LCPCF probe and are shown in Figure 3.24. And it should be noticed that at low concentrations, peaks from the lactate medium or lactate medium/LCPCF can be observed:  $1340 \text{ cm}^{-1}$  and  $1391 \text{ cm}^{-1}$

were seen in bulk detection and peaks at  $1052\text{ cm}^{-1}$ ,  $1342\text{ cm}^{-1}$  and  $1383\text{ cm}^{-1}$  were seen in LCPCF detection respectively.

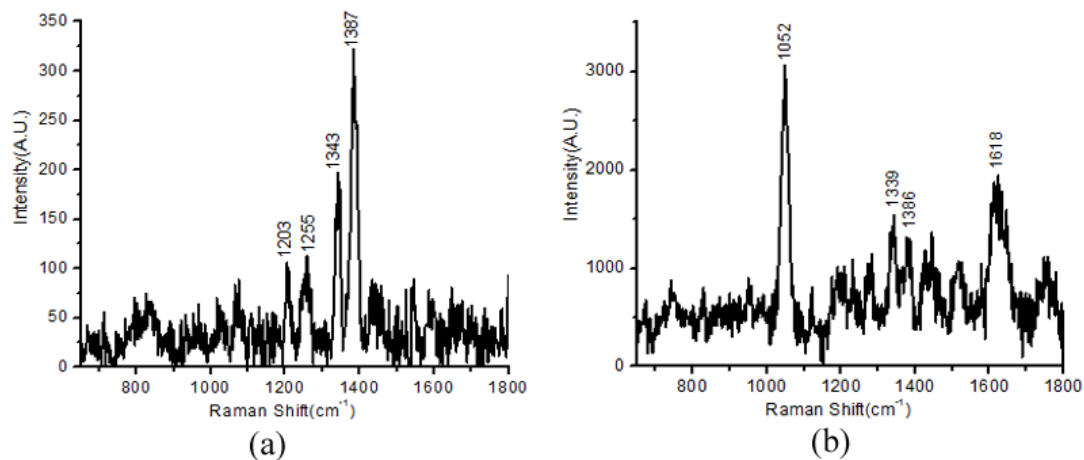


Figure 3.24: Control experiment with lactate medium and SNPs but without MR-1 cells in both (a) bulk detection and (b) using the LCPCF SERS probe. Adapted with permission from ref. 31. Copyright 2011 American Chemical Society.

Table 3.3. Band assignments for bacteria of *Shewanella oneidensis* MR-1. Adapted with permission from ref. 31. Copyright 2011 American Chemical Society.

Bulk( $10^{10}$ cells/mL)	Bulk( $10^9$ cells/mL)	LCPCF( $10^{10}$ cells/mL)	LCPCF( $10^8$ cells/mL)	LCPCF( $10^6$ cells/mL)	Assignments
675	675	675	666	670	Same as reported
730	730	730	730	730	Adenine
----	832	832	----	----	CCH (Aliphatic)
925	925	925	925	925	C-COO <sup>-</sup> stretching
955	955	955	955	----	C-C stretching
1003	----	1003	1003	----	Phe
-----	-----	-----	1052	1052	lactate medium in LCPCF
----	----	1109	1109	----	
1127	1127	-----	-----	1127	NH <sub>3</sub> <sup>+</sup> deformation
----	----	1156	1156	1156	NH <sub>3</sub> <sup>+</sup> deformation
1213	----	1213	1213	1208	Ring Breath
----	1270	1270	1250, 1270	1270, 1290	Amide III
1327	----	1327	1327	-----	CH <sub>2</sub> wagging
----	1340	-----	-----	1342	lactate medium
1368	----	1368	-----	-----	CH <sub>2</sub> scissoring
----	1391	-----	1383	-----	lactate medium
----	----	-----	1422	1415	COO <sup>-</sup> symmetric stretching
1449	1449	1449	1479	-----	CH <sub>2</sub> scissoring
1536	1532	1536	1536	1536	COO <sup>-</sup> asymmetric stretching
1597	1597	1597	1597	1600	Bacterial amide
1643	-----	1643	1639	-----	Amide I
----	1678	1674	1677	-----	Amide I

# Chapter 4. Portable fiber SERS sensing systems

Molecular sensors based on Raman/SERS and optical fiber probes have been widely applied in chemical and biological detection and sensing due to their unique advantages, such as molecular specificity, high sensitivity, flexibility, reliability and also remote sensing capabilities. However, the bulky spectrometer in the sensing system seriously limits their practical applications outside the laboratory. Recently, portable Raman spectrometers have been developed and are commercially available although their sensitivity still needs to be improved. Fiber SERS probes integrated with a portable Raman spectrometer offer an ideal solution to a compact and flexible sensing system with high sensitivity and molecular specificity.

In Section 2 and Section 3, we have demonstrated that TCMMF and LCPCF SERS probes can achieve higher sensitivity than the bulk detection. And previously, LCPCF SERS probe integrated with a portable Raman spectrometer was proposed in the preliminary study by Shi et al. [87]. However, the unique high sensitivity was not well preserved and the achieved sensitivity was only roughly the same as that of bulk detection.

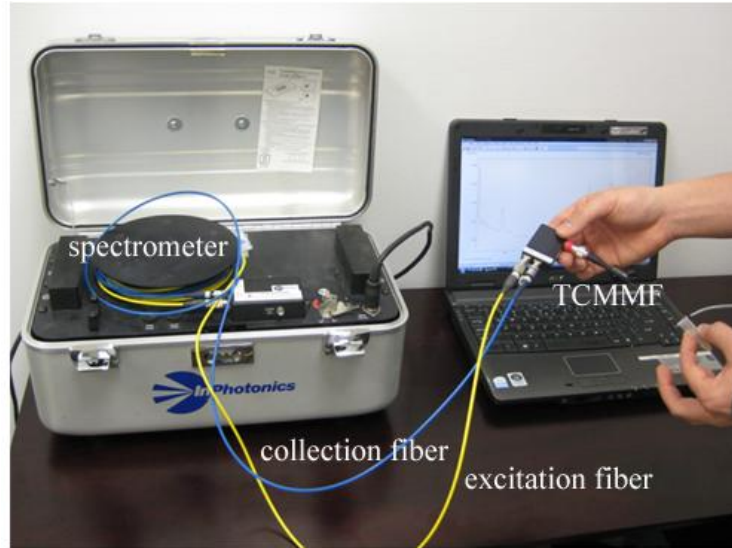
In this part, we experimentally demonstrate two improved approaches of integrating fiber SERS probes with a portable Raman spectrometer for higher sensitivity [30]. The first approach is the TCMMF-portable SERS system, which uses

the original design of the TCMMF as the test probe and can achieve 2-3 times better sensitivity than bulk detection, the same level of improvement as that achieved in the bulky Renishaw Raman system. The TCMMF-portable SERS system, using the standard FC/PC connectors, is lens-free and does not need any optical alignment. In addition, the TCMMF probe can be reusable after ultrasonic washing with Milli-Q water. The second approach is the highly-sensitive LCPCF-portable SERS system, whose sensitivity can reach up to 59 times as that of bulk detection, comparable to the value of 100 times using the Renishaw Raman system. The demonstration of the highly-sensitive portable SERS systems offers a very promising and powerful technique for various chemical, biological, medical, and environmental detections outside the laboratory.

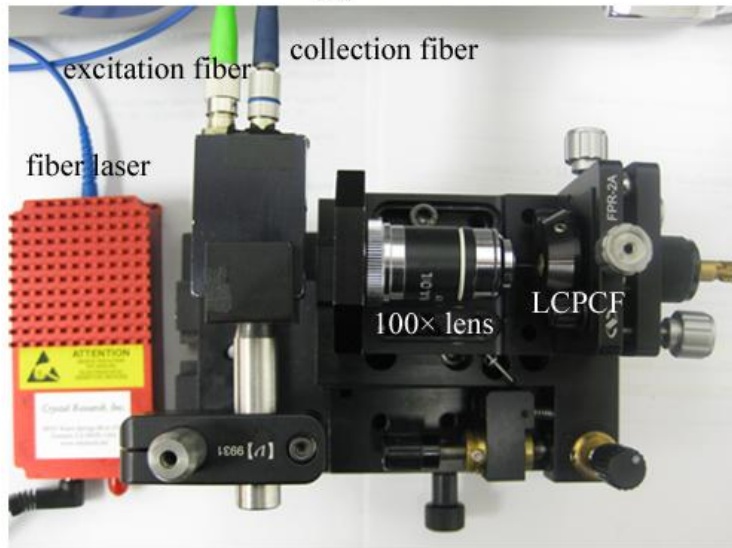
#### **4.1 Experimental demonstrations of portable fiber SERS systems**

The optical setups for the integration of the TCMMF and LCPCF SERS probes with a portable Raman spectrometer are shown in Figure 4.1 (a) and (b), respectively [30]. And Figure 4.2 show their corresponding schematics. For the TCMMF-portable SERS system shown in Figure 4.2 (a), a custom-designed probe box (also shown in Figure 4.1(a) as the black box held in the right hand) offers the standard FC/PC connectors for the excitation fiber, the collection fiber, and the TCMMF SERS probe. The excitation laser source inside the portable Raman spectrometer (785 nm, 70 mW) was delivered to the probe box by a multimode optical fiber. A band-pass filter inside the box was implemented to remove the fused silica Raman background from the

fiber and only transmit the laser light. Also a long-pass filter was used to transmit only the Raman scattered signal, which was reflected by a dichroic beam splitter.

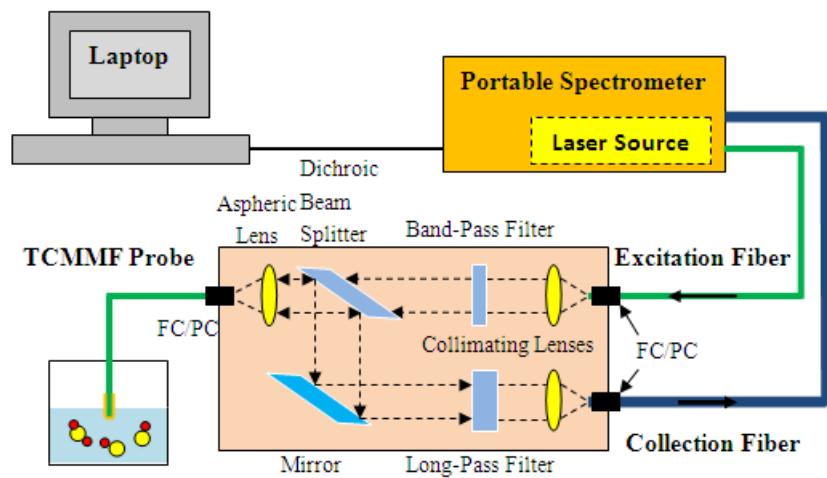


(a)

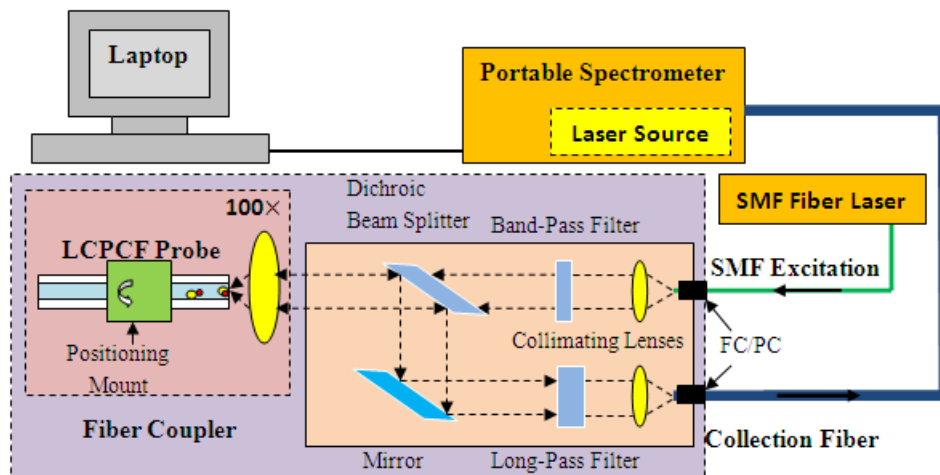


(b)

Figure 4.1: Experimental set-up: (a) TCMMF-portable SERS system; (b) LCPCF-portable SERS system (spectrometer and laptop computer not included). Adapted with permission from ref. 30. Copyright 2010 American Institute of Physics.



(a)



Portable Coupling Stage

(b)

Figure 4.2: Schematics of (a) TCMMF-portable SERS system and (b) LCPCF-portable SERS system (not to scale). Adapted with permission from ref. 30.

Copyright 2010 American Institute of Physics.

And for the LCPCF-portable SERS system shown in Figure 4.1 (b), a compact position stage was designed and used for the integration and alignment. A singlemode fiber laser (785 nm, 20 mW) was chosen as the excitation source, for the purpose of better mode matching, and coupled to the filter box by FC/PC connectors. A 100× objective lens was used for the coupling between the filter box and the LCPCF SERS probe that was mounted on an adjustable stage. For the bulk detection, a small lens with 7.5 mm focal length was placed at the output port of the filter box, replacing the aspheric lens and the output FC/PC connector in Figure 4.2 (a), for focusing the laser beam onto the sample solution and collecting the SERS signal as well. The portable Raman spectrometer was purchased from InPhotonics.

In this experiment, SNPs were used as the SERS substrates and R6G was used as a test molecule. SNPs used in the sample solution were the same as before, which were synthesized using the Lee and Meisel method [54]. The sample solution was prepared as that in Section 3.3.1, in which sodium chloride (10 mM) was added to induce aggregation of SNPs for optimum SERS performance. For the TCMMF-portable SERS system, the spectrum of  $10^{-5}$  M SERS sample solution was measured with an integration time of 10 s. For the LCPCF-portable SERS system, the spectrum of  $10^{-6}$  M sample solution was measured with an integration time of 10 s.

In this study, we chose the original design of the TCMMF probe by using the hexanethiolate-protected SNPs on the optical fiber tip [28]. The multimode fiber used to build the TCMMF SERS probe was the same as that used in Section 2.1 (Newport, model F-MLD-500). One end of the optical fiber was self-packaged with a FC/PC

connector while the other end was tip coated with another type of SNPs synthesized by a modified Brust protocol, which corresponded to the original design of the TCMMF probe proposed by Shi et al. [28]. Basically, 170 mg of AgNO<sub>3</sub> was dissolved in 5 mL of ethanol and kept under magnetic stirring. And 3 molar equivalents of hexanethiol were added dropwise followed by an addition of 80 mL of toluene. The solution was then reduced with a tenfold molar excess of NaBH<sub>4</sub> in 10 mL of nanopure water. The reduction was allowed to proceed overnight. Subsequently, the solution was washed several times with nanopure water to remove any inorganic impurities and the toluene phase was collected and placed under rotary evaporation. The nanoparticles were further purified with methanol. The average core size of the resulting hexanethiolate-protected SNPs (AgC<sub>6</sub>) was 5 ± 2 nm. The coating procedure was simpler than the one used previously; the tip of the fiber was dipped into the SNPs solution overnight without any complicated procedures [28, 30].

As for the LCPCF preparation, it is the same as that in Section 3.3. The LCPCF probe was placed in the fiber holder on the coupler with the sealed end facing toward the objective lens. The alignment for coupling the laser beam onto the surface of the core of LCPCF was performed with adjusting screws on the fiber coupler with 5 degrees of freedom, 3 translational and 2 rotational; and a power meter was placed after the LCPCF to monitor the transmitted power. The best SERS signal was achieved near the point with the maximum transmitted power, but not exactly at the transmission peak where a significant amount of power could be coupled into the cladding.

## 4.2 Results and discussion

Figure 4.3 shows the SERS signals collected from the TCMMF-portable SERS system and the bulk detection when the concentration of R6G is  $10^{-5}$  M. Comparing the typical peak at  $1358\text{ cm}^{-1}$ , the signal obtained with the TCMMF system is around 2.5 times that obtained from the bulk detection. Since the core size of the TCMMF is  $100\text{ }\mu\text{m}$ , the same as that of the excitation fiber, the coupling is relatively easy by using a collimating lens and an aspheric focusing lens between the excitation fiber and the TCMMF probe. In addition, a  $200\text{ }\mu\text{m}$  (core size) collection fiber is chosen for better collection efficiency. Therefore, the sensitivity enhancement, defined as the ratio between the SERS signals obtained with the TCMMF and from the bulk detection, achieved by using the TCMMF-portable SERS system can be the same as that achieved by using the bulky Renishaw system [28, 30]. Besides the higher sensitivity, the other advantage of the TCMMF-portable SERS system is the freedom from any optical alignment. The TCMMF SERS probe can be interfaced with the rest of the system by FC/PC connectors, and the measurement is easily taken by just inserting the fiber probe into the sample solution by hand, as shown in Figure 4.1 (a).

Moreover, we have demonstrated that the TCMMF SERS probe can be reusable. Since the SNPs coated on the fiber are not dissolvable in water, the probe can be ultrasonically washed by Milli-Q water. Figure 4.4 shows that after two washing cycles, the SERS signal is still roughly the same as before. No SERS signal was observed with the tip only after the washing procedure, which demonstrated the dye

molecules have been washed away. All these characteristics of the TCMMF-portable SERS system including higher sensitivity, portability, and reusability make it well-suited for various practical applications.

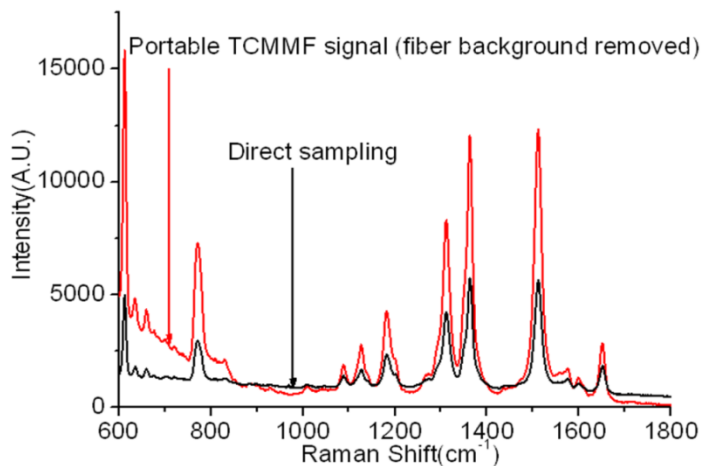


Figure 4.3: SERS signals obtained using the portable-TCMMF system and that obtained using direct sampling, when the R6G concentration is  $10^{-5}$  M. Adapted with permission from ref. 30. Copyright 2010 American Institute of Physics.

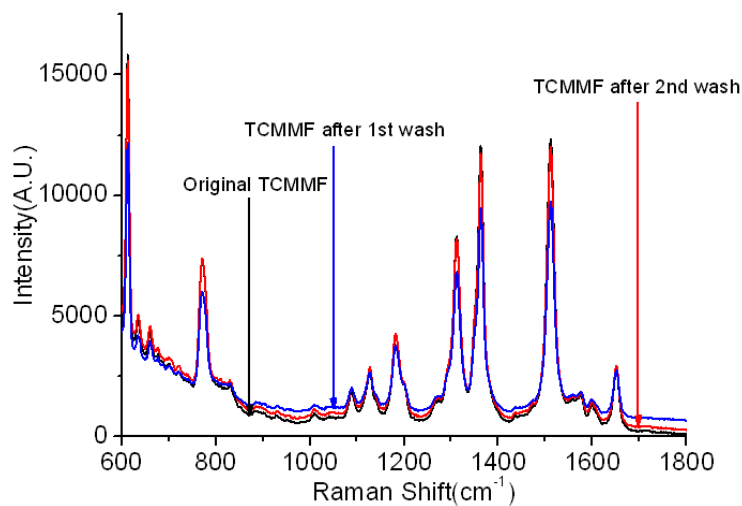


Figure 4.4: SERS signals obtained using the portable-TCMMF system after washing procedures. Adapted with permission from ref. 30. Copyright 2010 American

Institute of Physics.

For the LCPCF-portable SERS system, since LCPCF has a much smaller core size (6  $\mu\text{m}$  in diameter), coupling between the laser source and the LCPCF is much more challenging than the TCMMF system. Misalignment or large beam size would affect the coupling efficiency and therefore degrade the performance of the highly sensitive SERS probe. In our system, a single-mode fiber laser was implemented to replace the excitation laser built in the portable Raman spectrometer, and a  $100\times$  objective lens was applied to achieve a small enough beam size for coupling. The beam size at the focal plane can be as small as 5  $\mu\text{m}$  measured by a CCD imaging system, which is very suitable for the coupling considering the core size of the LCPCF (6  $\mu\text{m}$  in diameter). To integrate the LCPCF SERS probe with the fiber laser and the portable spectrometer, a compact portable coupling stage with adjustment screws was built, as shown in Figure 4.1 (b). All optical components, except the fiber holder, are fixed on the base. The fiber holder can be adjusted with 5 degrees of freedom, including 3 translational and 2 rotational, by using the screws on the mount.

Figure 4.5 shows the SERS signals collected from the bulk detection and that from the portable LCPCF SERS system. Compared to the result shown in Figure 4.5 (a), Figure 4.5 (b) demonstrates that the portable LCPCF SERS system's sensitivity is 59 times that of bulk detection, choosing the intensity of the  $1358\text{ cm}^{-1}$  peak as a reference. This enhancement is comparable to the 100 times achieved when using the LCPCF SERS probe under the Renishaw system. The difference in sensitivity enhancement between the portable system and bulky Renishaw system can be due to

the coupling between the objective lens and the LCPCF. In the portable system the alignment was performed with the help of a power meter; while in the Renishaw system the CCD camera was utilized to facilitate the alignment. Other possible factors that limit the achievement of the 100 times sensitivity enhancement include the performance of other optical parts in the portable fiber SERS system. At present, the 59 times sensitivity enhancement has already been quite significant for a portable Raman system.

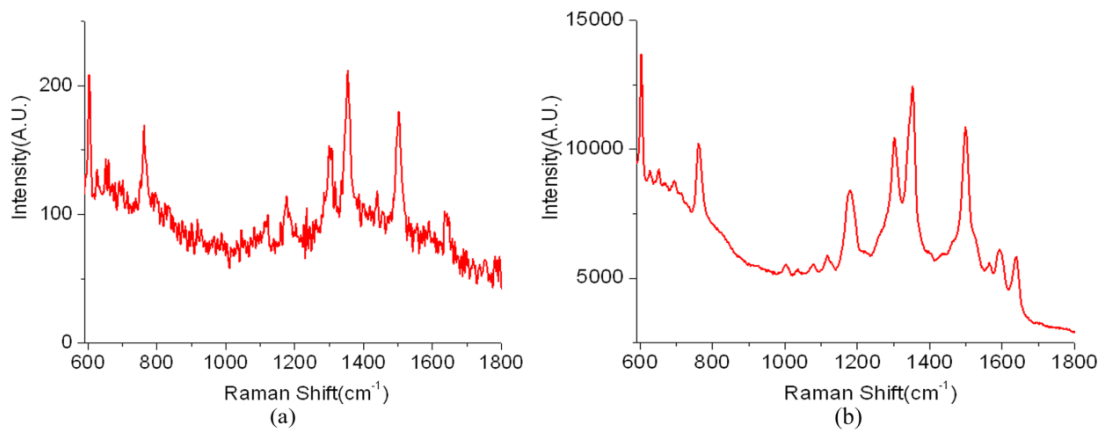


Figure 4.5: SERS signals obtained using (a) direct sampling, and (b) the portable-LCPCF system, when the R6G concentration is  $10^{-6}$  M. Adapted with permission from ref. 30. Copyright 2010 American Institute of Physics.

## Chapter 5. Summary

The above results show that optical fibers provide an excellent platform for molecular sensors, which are molecular specific, highly sensitive, flexible, and compact. In this work, we emphasize two categories of optical fiber sensors based on RS or SERS and demonstrate these fiber probes can be applied in various interesting chemical and biological detections.

The first category is based on the conventional multimode optical fibers, which are implemented with two types of novel SERS techniques. The first SERS technique is based on a double substrate “sandwich” structure using colloidal metal nanoparticles. We demonstrate that it provides  $\sim 10\times$  times sensitivity enhancement compared to the bulk detection by enhancing the local EM field and can push the detection limit of lysozyme and cytochrome c to 0.2  $\mu\text{g/mL}$  in aqueous solutions. The second SERS technique is to use the advanced interference lithography technique which has the advantages of high uniformity, high reproducibility, and potential mass-production capability; in this case, the fiber facet is patterned with silver-coated nanopillar array as the SERS-active substrate. We demonstrate a high EF of  $1.2\times 10^7$  can be achieved by focusing the laser directly onto the nanopillar array substrate. More importantly, we successfully employ this probe for the in-situ remote sensing of toluene vapor (2-3%) and 2,4-dinitrotoluene vapor (100 ppb).

The second category is the HCPCF sensors. For HCPCF, it employs a guiding mechanism fundamentally different from that in conventional index guiding fibers. In

an HCPCF, periodic air channels in a glass matrix acts as reflectors to confine light in an empty core. By filling the air channel(s) with the target analyte, HCPCF can provide an ideal platform for the strong interaction between the light and the analyte while minimizing the interference from the glass background, and therefore it is very promising to improve the sensitivity performance of existing Raman/SERS techniques. In particular, we demonstrate it can be used for the Raman sensing of the ambient greenhouse gas ( $\text{CO}_2$ ) and also for the quantitative multiplexed Raman sensing of organic vapor mixture (toluene, acetone, and 1,1,1-trichloroethane). By using a liquid-filled PCF probe, it can also be applied for the glucose Raman sensing in the physiological concentration range, which is very useful in the diagnosis and management of diabetes mellitus. In addition, we theoretically and experimentally demonstrate this technique can work very well with the SERS detection using metal nanoparticles as the SERS-active substrates. With a highly sensitive LCPCF probe, we demonstrate a detection limit of 0.1 nM for R6G dye molecules. We also show that it can be successfully applied in the detections and characterizations of biological macromolecules or systems such as bacteria cells and a detection limit of  $10^6$  cells/mL has been achieved for *Shewanella oneidensis*.

Moreover, we demonstrate these fiber sensors can be integrated with the portable Raman spectrometer to build compact sensor systems for molecular detections. The performance of the sensitivity enhancement of these probes in the portable Raman system can be comparable to that in the bulky Raman system by using the appropriate coupling designs. These fiber SERS probes integrated with a portable Raman

spectrometer provide a promising scheme for the development of a compact and flexible molecular sensing system with high sensitivity and portability.

The aim of future study is to further push the sensitivity of these fiber sensors by optimizing the fabrication techniques of the SERS substrates and the optical fibers. There is also a strong need to understand the fundamental mechanisms and guidelines in the design optimization processes, such as the activation of surface plasmon resonance, surface chemistry for molecular adsorption, structure optimization for photonic bandgap guidance, and etc. In addition, a better packaging design is needed for the HCPCF probes in the portable Raman system. The final goal of this project is to develop an all-fiber integrated remote sensing system, which is highly sensitive, molecular specific, flexible, compact, portable, easy to use, and low cost.

## Bibliography

1. K. Kneipp, H. Kneipp, I. Itzkan, R. R. Dasari, and M. S. Feld, Ultrasensitive chemical analysis by Raman spectroscopy, *Chem. Rev.* 99, 2957-2975, 1999.
2. D. A. Long, *Raman Spectroscopy*, McGraw-Hill, New York, 1977.
3. S. Weiss, Fluorescence spectroscopy of single biomolecules, *Science* 283, 1676-1683, 1999.
4. W. H. Nelson and J. F. Sperry, UV Resonance Raman Spectroscopic Detection and Identification of Bacteria and other Microorganisms, in *Modern Techniques for Rapid Microbiological Analysis*, VCH, New York, 1991.
5. M. Moskovits, Surface-enhanced spectroscopy, *Rev. Mod. Phys.* 57, 783, 1985.
6. A. Campion and P. Kambhampati, Surface-enhanced Raman scattering, *Chem. Soc. Rev.* 27, 241-250, 1998.
7. K. Kneipp, H. Kneipp, I. Itzkan, R. R. Dasari, and M. S. Feld, Surface-enhanced Raman scattering and biophysics, *J. Phys.: Condens. Matter* 14, R597-R624, 2002.
8. M. Fleischmann, P. J. Hendra, and A. J. McQuillan, Raman spectra of pyridine adsorbed at a silver electrode, *Chem. Phys. Lett.* 26, 163-166, 1974.
9. K. A. Willets and R. P. Van Duyne, Localized surface plasmon resonance spectroscopy and sensing, *Ann. Rev. Phys. Chem.* 58, 267-297, 2007.
10. G. C. Schatz and R. P. Van Duyne, Electromagnetic Mechanism of Surface-Enhanced Raman Spectroscopy, *Handbook of Vibrational Spectroscopy*, 2006.

11. K. L. Kelly, E. Coronado, L. L. Zhao, and G. C. Schatz, The optical properties of metal nanoparticles: the influence of size, shape, and dielectric environment, *J. Phys. Chem. B* 107, 668-677, 2003.
12. A. Otto, I. Mrozek, and H. Grabhorn, Surface enhanced Raman scattering, *J. Phys. Cond. Mat.* 4, 1143, 1992.
13. B. J. Wiley, S. H. Im, Z. Y. Li, J. McLellan, A. Siekkinen, and Y. Xia, Maneuvering the surface plasmon resonance of silver nanostructures through shape-controlled synthesis. *J. Phys. Chem. B* 110, 15666, 2006.
14. K. Faulds, R. E. Littleford, D. Graham, G. Dent, and W. E. Smith, Comparison of surface-enhanced resonance Raman scattering from unaggregated and aggregated nanoparticles. *Anal. Chem.* 76, 592, 2004.
15. I. W. Sztainbuch, The effects of Au aggregate morphology on surface-enhanced Raman scattering enhancement, *J. Chem. Phys.* 125, 124707, 2005.
16. P. Hildebrandt and M. Stockburger, Surface-enhanced resonance Raman spectroscopy of Rhodamine 6G adsorbed on colloidal silver. *J. Phys. Chem.* 88, 5935, 1984.
17. H. Xu, J. Aizpurua, M. Kall, and P. Apell, Electromagnetic contributions to single-molecule sensitivity in surface-enhanced Raman scattering, *Phys. Rev. E* 62, 4318, 2000.
18. G. P. Agrawal, *Fiber-Optic Communication Systems*, Wiley, 2002.
19. K. I. Mullen and K. T. Carron, Surface-enhanced Raman spectroscopy with abrasively modified fiber optic probes, *Anal. Chem.* 63, 2196-2199, 1991.

20. D. L. Stokes and T. Vo-Dinh, Development of an integrated single-fiber SERS sensor, *Sens. Actuators B* 69, 28, 2000.
21. D. L. Stokes, Z. H. Chi, and T. Vo-Dinh, Surface-enhanced-Raman-scattering-inducing nanoprobe for spectrochemical analysis, *Appl. Spectrosc.* 58, 292, 2004.
22. C. Viets and W. Hill, Single-fibre surface-enhanced Raman sensors with angled tips, *J. Raman Spectrosc.* 31, 625, 2000.
23. C. Viets and W. Hill, Laser power effects in SERS spectroscopy at thin metal films, *J. Phys. Chem. B* 105, 6330, 2001.
24. C. Viets and W. Hill, Comparison of fibre-optic SERS sensors with differently prepared tips, *Sens. Actuators B* 51, 92, 1998.
25. A. Lucotti and G. Zerbi, Fiber-optic SERS sensor with optimized geometry, *Sens. Actuators B: Chem.* 121, 356-364, 2007.
26. V. Guieu, P. Garrigue, F. Lagugne-Labarthe, L. Servant, N. Sojic, and D. Talaga, Remote surface enhanced Raman spectroscopy imaging via a nanostructured optical fiber bundle, *Opt. Express* 17, 24030-24035, 2009.
27. Y. Zhang, C. Gu, A. Am. Schwartzberg, and J. Z. Zhang, Surface-enhanced Raman scattering sensor based on D-shaped fiber, *Appl. Phys. Lett.* 87, 123105, 2005.
28. C. Shi, H. Yan, C. Gu, D. Ghosh, L. Seballos, S. Chen, and J. Z. Zhang, A double substrate sandwich structure for fiber surface enhanced Raman scattering detection, *Appl. Phys. Lett.* 92, 103107, 2008.

29. C. Shi, C. Lu, C. Gu, L. Tian, R. Newhouse, S. Chen and J. Z. Zhang, Inner wall coated hollow core waveguide sensor based on double substrate surface enhanced Raman scattering, *Appl. Phys. Lett.* 93, 153101, 2008.
30. X. Yang, Z. Tanaka, R. Newhouse, Q. Xu, B. Chen, S. Chen, J. Z. Zhang and C. Gu, Portable fiber sensors based on surface-enhanced Raman scattering, *Rev. Sci. Instrum.* 81, 123103, 2010.
31. X. Yang, C. Gu, F. Qian, Y. Li, and J. Z. Zhang, Highly sensitive detection of proteins and bacteria in aqueous solution using surface-enhanced Raman scattering and optical fibers, *Anal. Chem.* 83, 5888-5894, 2011.
32. G. F. S. Andrade, M. Fan, and A. G. Brolo, Multilayer silver nanoparticles-modified optical fiber tip for high performance SERS remote sensing, *Biosens. Bioelectron.* 25, 2270-2275, 2010.
33. A. Dhawan, M. Gerhold, A. Madison, J. Fowlkes, P. E. Russell, T. Vo-Dinh, and D. N. Leonard, Fabrication of nanodot plasmonic waveguide structures using FIB milling and electron beam-induced deposition, *Scanning* 31, 139-146, 2009.
34. E. J. Smythe, M. D. Dickey, G. M. Whitesides, and F. Capasso, A technique to transfer metallic nanoscale patterns to small and non-planar surfaces, *ACS Nano* 3, 59-65, 2009.
35. E. J. Smythe, M. D. Dickey, J. Bao, G. M. Whitesides, and F. Capasso, Optical antenna arrays on a fiber facet for in situ surface-enhanced Raman scattering detection, *Nano Lett.* 9, 1132-1138, 2009.

36. G. Kostovski, D. J. White, A. Mitchell, M. W. Austin, and P. R. Stoddart, Nanoimprinted optical fibers: biotemplated nanostructures for SERS sensing, *Biosens. Bioelectron.* 24, 1531-1535, 2009.
37. G. Kostovski, U. Chinnasamy, S. Jayawardhana, P. R. Stoddart, and A. Mitchell, Sub-15 nm optical fiber nanoimprint lithography: a parallel, self-aligned and portable approach, *Adv. Mater.* 23, 531-535, 2011.
38. T. A. Birks, P. J. Roberts, P. St. J. Russell, D. M. Atkin, and T. J. Shepherd, Full 2-D photonic bandgaps in silica/air structures, *Electron. Lett.* 31, 1941-1943, 1995.
39. R. F. Cregan, B. J. Mangan, J. C. Knight, T. A. Birks, P. St. J. Russell, P. J. Roberts, and D. C. Allan, Single-mode photonic band gap guidance of light in air, *Science* 285, 1537-1539, 1999.
40. F. Benabid, J. C. Knight, G. Antonopoulos, and P. St. J. Russell, Stimulated Raman scattering in hydrogen-filled hollow-core photonic crystal fiber, *Science* 298, 399-402, 2002.
41. F. Benabid, J. C. Knight, and P. St. J. Russell, Particle levitation and guidance in hollow-core photonic crystal fiber, *Opt. Express* 10, 1195-1203, 2002.
42. T. Ritari, J. Tuominen, H. Ludvigsen, J. C. Petersen, T. Sorensen, T. P. Hansen, and H. R. Simonsen, Gas sensing using air-guiding photonic bandgap fibers, *Opt. Express* 12, 4080-4087, 2004.
43. S. Smolka, M. Barth, and O. Benson, Highly efficient fluorescence sensing with hollow core photonic crystal fibers, *Opt. Express* 15, 12783-12791, 2007.

44. S. O. Konorov, C. J. Addison, H. G. Schulze, R. F. B. Turner, and M. W. Blades, Hollow-core photonic crystal fiber-optic probes for Raman spectroscopy, *Opt. Lett.* 31, 1911-1913, 2006.
45. M. P. Buric, K. P. Chen, J. Falk, and S. D. Woodruff, Enhanced spontaneous Raman scattering and gas composition analysis using a photonic crystal fiber, *Appl. Opt.* 47, 4255-4261, 2008.
46. M. P. Buric, K. P. Chen, J. Falk, and S. D. Woodruff, Improved sensitivity gas detection by spontaneous Raman scattering, *Appl. Opt.* 48, 4424-4429, 2009.
47. X. Yang, A. Y. Zhang, D. A. Wheeler, T. C. Bond, C. Gu, and Y. Li, Direct molecule-specific glucose detection by Raman spectroscopy based on photonic crystal fiber, *Anal. Bioanal. Chem.* 402, 687-691, 2012.
48. X. Yang, A. S. P. Chang, B. Chen, C. Gu, and T. C. Bond, High sensitivity gas sensing by Raman spectroscopy in photonic crystal fiber, *Sens. Actuators B*, in press, DOI: 10.1016/j.snb.2012.09.04, 2012.
49. Y. Han, S. Tan, M. K. K. Oo, D. Pristinski, S. Sukhishvili, and H. Du, Towards full-length accumulative surface-enhanced Raman scattering-active photonic crystal fibers, *Adv. Mater.* 22, 2647-2651, 2010.
50. H. Yan, C. Gu, C. Yang, J. Liu, G. Jin, J. Zhang, L. Hou, and Y. Yao, Hollow core photonic crystal fiber surface-enhanced Raman probe, *Appl. Phys. Lett.* 89, 204101, 2006.

51. Y. Zhang, C. Shi, C. Gu, L. Seballos, and J. Z. Zhang. Liquid core photonic crystal fiber sensor based on surface enhanced Raman scattering. *Appl. Phys. Lett.* 90, 193504, 2007.
52. X. Yang, C. Shi, D. Wheeler, R. Newhouse, B. Chen, J. Z. Zhang, and C. Gu, High-sensitivity molecular sensing using hollow-core photonic crystal fiber and surface-enhanced Raman scattering, *J. Opt. Soc. Am. A* 27, 977-984, 2010.
53. X. Yang, C. Shi, R. Newhouse, J. Z. Zhang, and C. Gu, Hollow core photonic crystal fibers for surface-enhanced Raman scattering probes, *Int. J. Opt.* 2011, 754610, 2011.
54. P. C. Lee and D. Meisel, Adsorption and Surface-Enhanced Raman of Dyes on Silver and Gold Sols, *J. Phys. Chem.* 86, 3391-3395, 1982.
55. V. Patil, R. B. Malvankar, and M. Sastry, Role of particle size in individual and competitive diffusion of carboxylic acid derivatized colloidal gold particles in thermally evaporated fatty amine films, *Langmuir* 15, 8197-8206, 1999.
56. X. X. Han, G. G. Huang, B. Zhao, and Y. Ozaki, Label-free highly sensitive detection of proteins in aqueous solutions using surface-enhanced Raman scattering, *Anal. Chem.* 81, 3329-3333, 2009.
57. M. Kahraman, I. Sur, and M. Culha, Label-free detection of proteins from self-assembled protein-silver nanoparticle structures using surface-enhanced raman scattering, *Anal. Chem.* 82, 7596-7602, 2010.

58. S. Stewart and P. M. Fredericks, Surface-enhanced Raman spectroscopy of peptides and proteins adsorbed on an electrochemically prepared silver surface, *Spectrochim. Acta, Part A* 55, 1615-1640, 1999.
59. S. Feng, X. Zhang, H. Wang, M. Xin, and Z. Lu, Fiber coupled waveguide grating structures, *Appl. Phys. Lett.* 96, 133101, 2010.
60. X. Yang, N. Ileri, C. C. Larson, T. C. Carlson, J. A. Britten, A. S. P. Chang, C. Gu, and T. C. Bond, Nanopillar array on a fiber facet for highly sensitive surface-enhanced Raman scattering, *Opt. Express*, 20, 24819-24826, 2012.
61. A. Fernandez, H. T. Nguyen, J. A. Britten, R. D. Boyd, M. D. Perry, D. R. Kania, and A. M. Hawryluk, Use of interference lithography to pattern arrays of submicron resist structures for field emission flat panel displays, *J. Vac. Sci. Technol. B* 15, 729-735, 1997.
62. M. R. Gartia, Z. Xu, E. Behymer, H. Nguyen, J. A. Britten, C. Larson, R. Miles, M. Bora, A. S. P. Chang, T. C. Bond, and G. L. Liu, Rigorous surface enhanced Raman spectral characterization of large-area high-uniformity silver-coated tapered silica nanopillar arrays, *Nanotechnology* 21, 395701, 2010.
63. M. Bora, B. J. Fasenfest, E. M. Behymer, A. S. P. Chang, H. T. Nguyen, J. A. Britten, C. C. Larson, J. W. Chan, R. R. Miles, and T. C. Bond, Plasmon resonant cavities in vertical nanowire arrays, *Nano Lett.* 10, 2832-2837, 2010.
64. A. S. P. Chang, M. Bora, H. T. Nguyen, E. M. Behymer, C. C. Larson, J. A. Britten, J. C. Carter, and T. C. Bond, Nanopillars array for surface enhanced Raman scattering, *Proc. SPIE*, 8024, 80240I, 2011.

65. A. Gutes, I. Laboriante, C. Carraro, and R. Maboudian, Silver nanostructures on silicon based on galvanic displacement process, *J. Phys. Chem. C* 113, 16939-16944, 2009.
66. A. Kim, F. S. Ou, D. A. A. Ohlberg, M. Hu, R. S. Williams, and Z. Li, Study of molecular trapping inside gold nanofinger arrays on surface-enhanced Raman substrates, *J. Am. Chem. Soc.* 133, 8234-8239, 2011.
67. <http://www.thorlabs.com/Thorcat/22700/HC-800B-SpecSheet.pdf>.
68. W. R. Fenner, H. A. Hyatt, J. M. Kellam, S. P. S. Porto, Raman cross section of some simple gases, *J. Opt. Soc. Am.* 63, 73-77, 1973.
69. A. Weber, E. A. McGinnis, The Raman spectrum of gaseous oxygen, *J. Mol. Spectrosc.* 4, 195-200, 1960.
70. S. Wild, G. Roglic, A. Green, R. Sicree, and H. King, Global prevalence of diabetes, estimates for the year 2000 and projections for 2030, *Diabetes Care*, 27, 1047-1053, 2004.
71. J. Wang, Electrochemical glucose biosensors, *Chem. Rev.* 108, 814-825, 2008.
72. P. G. Steffes, Laser-Based Measurement of Glucose in the Ocular Aqueous Humor: An Efficacious Portal for Determination of Serum Glucose Levels, *Diabetes Technol. Ther.* 1, 129-133, 1999.
73. D. C. Klonoff, J. Braig, B. Sterling, C. Kramer, D. Goldberger, R. Trebino, Mid-infrared spectroscopy for noninvasive blood glucose monitoring, *IEEE LEOS Newsletter* 12, 13-14, 1998.

74. B. D. Cameron, H. W. Gorde, B. Satheesan, G. L. Cote, The use of polarized laser light through the eye for noninvasive glucose monitoring, *Diabetes Technol. Ther.* 1, 125-143, 1999.
75. R. J. Russell, M. V. Pishko, C. C. Gefrides, M. J. McShane, G. L. Cote, A Fluorescence-Based Glucose Biosensor Using Concanavalin A and Dextran Encapsulated in a Poly(ethylene glycol) Hydrogel, *Anal. Chem.* 71, 3126-3132, 1999.
76. A. Tong, A. Yamauchi, T. Hayashita, Z. Zhang, B. Smith, N. Teramae, Boronic Acid Fluorophore/ $\beta$ -Cyclodextrin Complex Sensors for Selective Sugar Recognition in Water, *Anal. Chem.* 73, 1530-1536, 2001.
77. A. J. Berger, T. W. Koo, I. Itzkan, G. Horowitz, and M. S. Feld, Multicomponent blood analysis by near-infrared Raman spectroscopy, *Appl. Opt.* 38, 2916–2926, 1999.
78. K. E. Shafer-Peltier, C. L. Haynes, M. R. Glucksberg, and R. P. Van Duyne, Toward a glucose biosensor based on surface-enhanced Raman scattering, *J. Am. Chem. Soc.* 125, 588-593, 2003.
79. J. M. Yuen, N. C. Shah, J. T. Wahlsh, M. R. Glucksberg, and R. P. Van Duyne, Transcutaneous Glucose Sensing by Surface-Enhanced Spatially Offset Raman Spectroscopy in a Rat Model, *Anal. Chem.* 82, 8382-8385, 2010.
80. U. S. Dinish, F. C. Yaw, A. Agarwal, M. Olivo, Development of highly reproducible nanogap SERS substrates: Comparative performance analysis and its application for glucose sensing, *Biosens. Bioelectron.* 26, 1987-1992, 2011.

81. M. Kerker, O. Siiman, L. A. Bumm, and D. S. Wang, Surface enhanced Raman scattering (SERS) of citrate ion adsorbed on colloidal silver, *Appl. Opt.* 19, 3253–3255, 1980.
82. A. Farjadpour, D. Roundy, A. Rodriguez, M. Ibanescu, P. Bermel, J. D. Joannopoulos, S. G. Johnson, and G. Burr, Improving accuracy by subpixel smoothing in the finite-difference time domain, *Opt. Lett.* 31, 2972–2974, 2006.
83. R. M. Charles and K. H. Nealson, Bacterial manganese reduction and growth with manganese oxide as the sole electron acceptor, *Science* 240, 1319-1321, 1988.
84. J. C. Biffinger, J. Pietron, O. Bretschger, L. J. Nadeau, G. R. Johnson, C. C. Williams, K. H. Nealson, and B. R. Ringeisen, The influence of acidity on microbial fuel cells containing *Shewanella oneidensis*, *Biosens. Bioelectron.* 24, 900-905, 2008.
85. S. Preciado-Flores, D. A. Wheeler, T. M. Tran, Z. Tanaka, C. Jiang, M. Barboza-Flores, F. Qian, Y. Li, B. Chen, and J. Z. Zhang, SERS spectroscopy and SERS imaging of *Shewanella oneidensis* using silver nanoparticles and nanowires, *Chem. Commun.* 47, 4129-4131, 2011.
86. A. Sengupta, M. Mujacic, and E. J. Davis, Detection of bacteria by surface-enhanced Raman spectroscopy, *Anal. Bioanal. Chem.* 386, 1379–1386, 2006.
87. C. Shi, C. Gu, R. Newhouse, J. Z. Zhang, K. Tanaka, and B. Chen, Portable photonic crystal fiber sensor based on surface enhanced Raman scattering (SERS), in *Frontiers in Optics, OSA Technical Digest (CD) (Optical Society of America, 2009)*, paper FTuE4.